Università Politecnica delle Marche
Scuola di Dottorato di Ricerca in Scienze dell'Ingegneria
Corso di Dottorato in Ingegneria Civile, Ambientale, Edile e Architettura

---

Wave induced hydro and morpho-dynamics around a single slender pile: experimental and numerical analysis

Ph.D. Dissertation of:
Francesco Marini

Supervisor:
Prof. Alessandro Mancinelli

Assistant Supervisors:
Dr. Sara Corvaro
Prof. Javier L. Lara

Ph.D. Course coordinator:
Prof. Francesco Fatone

XVIII edition - New series

Abstract

During the last years, the presence of piled structures, such as offshore wind farms or oil platforms, in the marine environment is becoming more important. For this reason, it gains relevance the correct analysis of possible criticisms and uncertainties in the design process. The aim of this thesis is the study of both the hydrodynamics and the morphodynamics induced by regular and random waves over a single slender pile by means of laboratory and numerical modelling. Therefore, the objective of the present thesis is to contribute to a better understanding of such physical processes. In particular, it aims to provide some tools that can be useful in the design process, in order to avoid a wrong estimation of the most important parameters and, thus, to ensure a proper design of the piled marine structure and its facilities. Particular attention is paid on the evaluation of the total force due to wave action, on the scour at the base of the pile and on the run-up over its surface. A rigid bed model has been realised to evaluate the best approach for the estimation of the total force over the pile due to nonlinear waves. An alternative method to the classical Morison et al. (1950)'s approach has been proposed for the computation of the total force from the velocity and acceleration of the water particles from a measured water surface elevation time series. Such method consists in a *Fourier* spectral decomposition of the input free water surface signal; the contribution of each component, computed according to the *Airy* theory, is summed to obtain the total horizontal and vertical velocity along the vertical profile. The results showed that this approach allowed to give a very good estimate of the total force both in terms of maximum value and of the phase in which it occurs. On the contrary, the application of the linear theory for the calculation of the velocity to be applied in the force calculation (classical *Morison* approach used in the design process) leads to an underestimation of the peak value and to a wrong representation of the shape of the force. Another primary parameter in the stability of a structure in the marine environment is the scour at the base of the monopile. An additional experimental campaign is performed by means of a mobile bed model in which a vertical cylinder is placed over a sandy seabed and it is attacked by both regular and random nonlinear waves. The results for regular waves are quite in agreement with the earlier work of Sumer et al. (1992). However, the results of this study reveal that the scour process due to nonlinear regular waves starts for hydrodynamic conditions characterized by a lower intensity (*Keulegan-Carpenter* parameter $KC = 4$) in comparison with those reported in the literature for linear waves ($KC = 6$). Different formulas are proposed for its estimation depending on dimensionless parameter KC, and, in order to take into account of the nonlinearity of the wave, also the *Ursell* parameter (Ur). For random waves, the approach proposed by Ong et al. (2013) for scour evaluation has been modified. This method depends on the cumulative distribution function of the dimensionless crest heights but, because of its complexity, it has been simplified in order to became suitable for design pur-

poses without affecting the quality of the results. To better understand the process of formation, growth and detachment of vortices, measurements made by using the *Particle Tracking Velocimetry* (PTV) technique are carried out and the results are integrated with those from pressure sensors and from the mobile bed model for the characterization of the whole process of vortex formation and scour generation. The results showed that the wave phases and positions in which the maximum values of the pressure gradients occur, correspond to those in which the detachment of vortices is observed. From the interpretation of the contour maps of the vorticity and of the *Okubo-Weiss* (OW) parameter it is possible to explain the scour patterns obtained in the mobile bed campaign. Furthermore, a numerical model has been realised with the tool OpenFOAM® that permitted to contribute to the comprehension of the complex 3D physical phenomenon induced by the wave-structure interaction. A new wave generation boundary condition for the generation of a measured water surface elevation time series has been added to the numerical code. The corresponding velocity field in this boundary condition has been computed with the *Fourier* decomposition method mentioned above. The nonlinear waves of the rigid bed experimental campaign are here simulated for the better comprehension of the vortex formation process and for the estimation of wave run-up which is very important for the design of the access facility of the marine structures. Excellent results are obtained in comparison with experimental data of force, pressure, velocity and water elevation. The analysis of the maximum values of run-up is performed and the results are compared with some formula available in the literature. An adaptation of the equation of Hallermeier (1976), that compute the run-up depending on the crest height, is proposed and the results, obtained with a significant number of samples, are very good. Finally, the visualization of the three-dimensional vortical structures by means of the *Q-criterion* has been performed. The numerical results showed that, in some instances, a vortex generated during the first half of the wave period can remain in the area of influence of the pile. After the reversal of the flow, it changes the direction according to the stream until it is finally removed on the opposite side of the pile with respect to where it was generated. The results are in agreement with those of the PTV experimental campaign: both the phase, size and position of vortices are well represented. The achievements obtained with the numerical model are able to improve the understanding of the complex physical processes by linking the different results, such as the pressure gradients, vortical structures and the associated scour patterns.

Contents

List of Symbols

a_n	amplitude of the wave component n_i after the *fft*
A	wave motion horizontal amplitude
A_{rms}	rms value of the wave motion horizontal amplitude
b_c	distance between the load cell and the hinge in the rigid bed model
b_c	position of line of application of the wave force
C	wave velocity
C_g	wave group velocity
C_D	drag coefficient
C_M	inertia coefficient
d_{50}	mean grain diameter
d	maximum scour distance from the axis of the pile
d_*	dimensionless grain size
D	pile diameter
f_n	frequency of the wave component n_i after the *fft*
F_c	force measured in correspondence of the load cell
F_D	drag force
F_I	inertia force
F_w	force applied in position b_w
F	total force
g	gravitational accelaration
h	water depth
H	water heigth
H_s	significant wave heigth
$H(w_c - w_{c1/n})$	Heaviside-function
k	wave number
k_n	wave number of the wave component n_i after the *fft*
k_p	wave number corresponding to the peak frequency
k_1	wave number corresponding to the spectral mean wave period
k_s	roughness parameter
KC	Keulegan-Carpenter number
KC_{rms}	rms Keulegan-Carpenter number
KC_η	modified Keulegan-Carpenter number for random waves
L	wave length
m	kinetic coefficient in run-up formulas

n	the portion of the highest random wave crests, among those exceeding the limiting value w_{c1}, that contribute to the scour process
n_i	index of the wave component derived from the *fft* process
N_{tot}	the total numbers of samples of a water elevation time series
n_w	group factor number
p^*	pseudo-dynamic pressure
P	total pressure
P_d	dynamic pressure
$P(w_c)$	probability density function of the dimensionless crest height
P_η	probability of exceedence of the dimentionless crest heigth
$P(w_c)$	Weibull cumulative distribution function of the dimentionless crest heigth
PE	percent error
Re	Reynolds number
Re_D	pile Reynolds number
R_u	run-up over the pile
s	specific gravity of sediment grains
S	scour depth along the pile
S_n	computed scour depth for random waves obtained with a specific value of n
S_{max}	maximum scour depth around the pile
$S_u(f)$	power spectrum of the horizontal velocity
t	time
t_{max}	maximum duration of a test
T	wave period
T_1	spectral mean wave period
T_p	wave peak period
T_S	scour equilibrium time scale
T^*	dimentionless equilibrium time scale
$S_\eta(f)$	wave spectrum of the instantaneous free surface elevation
S_1	wave steepness for random waves
U	horizontal particle velocity along the x direction
U_c	critical horizontal velocity for initiation of motion
$\mathbf{U}$	velocity vector
U_f	undisturbed bed shear velocity
U_m	undisturbed orbital velocity at the bottom
U_{rms}	rms value of the undisturbed orbital velocity at the bottom
Ur	Ursell number
Ur_1	Ursell number for random waves
V	horizontal particle velocity along the y direction
W	vertical particle velocity
w_c	dimensionless crest elevation

w_{c1}	lower dimensionless crest elevation limiting value of the truncated Weibull distribution
$w_{c1/n}$	limiting value that, among the waves higher than w_{c1}, identifies the waves that give a contribution to the scour process
$\mathbf{X}$	position vector
X_n	complex amplitude for each wave component n_i
x	horizontal coordinate: zero in correspondence of the centre of the pile
x'	curvilinear coordinate: distance along the cylinder surface from the stagnation point
y	horizontal transversal coordinate: zero in correspondence of the centre of the pile
$Y(w_c)$	dimensionless scour depth associated to w_c
z	vertical coordinate: zero at s.w.l. and positive upwards
α, β	2D Weibull parameters
α_i	VOF fraction of the i-th phase
α_1	VOF indicator function
$\frac{\partial u}{\partial t}$	horizontal particle acceleration
δ_n	average value of the relative scour error
ϵ	spectral width parameter
ε	wave nonlinearity
$\eta(t)$	water surface elevation
$\eta_0(t)$	experimental water elevation time series at the location of the wave generation
η_c	wave crest elevation
$\eta_{c,d}$	design wave crest elevation
θ	Shields parameter
θ_{cr}	critical Shields parameter
κ	curvature of the interface
μ_{eff}	efficient dynamic viscosity
ν	kinematic viscosity of the fluid
ρ	water density
ρ_s	sand density
σ	surface tension coefficient
σ_D	sediment uniformity diameter
σ_η	integer of the wave spectrum of the instantaneous free surface elevation
$\bar{\tau}_0$	bed shear stress
$\bar{\tau}_{m0}$	maximum undisturbed bed shear stress for waves
φ	angular coordinate: angle measured from the x axis and centred in the middle of the pile
ϕ	phase angle
ϕ_n	phase angle of the wave component n_i after the *fft*
ω	angular frequency
ω_p	peak angular frequency

List of Figures

List of Tables

Chapter 1

Introduction

During the last years, the development of renewable energies led to the growth of wind farms and offshore platforms over the main seas. Only in 2018, Europe connected 409 new offshore wind turbines reaching a total installed offshore wind capacity of 18499MW (WindEurope, 2019). In 2019 it will be operational the first wind farm in the Mediterranean sea, it will consist in 10 turbines with a total capacity of 30MW and it will be placed in Taranto (Italy). In Italy, the importance of offshore wind energy is increasing such that in the latest proposed national plan on energy and climate (Energia Clima 2030, 2019) the power growth objective for 2025 is set to 300MW and for 2030 to 900MW. In the italian seas, the available water depths for the installation of wind farms are mainly in shallow/intermediate waters ($h/L < 0.5$) and thus, in the present thesis, such water depth condition is considered.
The knowledge of the hydro and morpho-dynamics induced by such structures is very important for their design. In particular, the aim of this thesis is to improve the knowledge of the main physical processes due to the wave-structure interaction that can highly impact on their correct design. Among the aspects analysed in this thesis, particular attention is paid on the force and run-up on the pile. Moreover, the generation and growth of coherent structures around the cylinder and the induced net scour are studied. The present topics have been experimentally and numerically studied in the literature (e.g., Sumer et al., 1997; Olsen and Kjellesvig, 1998; Roulund et al., 2005; Baykal et al., 2017). In open oceans, waves and currents can coexist, and, depending on the specific site, the effects of currents may dominate over those of waves and vice versa. In a number of instances (e.g., middle Adriatic Sea, South African coast, south-eastern Australian coast), the tidal range is significantly smaller than the wave height at breaking and hence a micro-tidal regime is observed in which waves mostly influence the morphological processes (Masselink and Short, 1993). In the middle Adriatic sea, for example, the tidal current is also smaller than the current due to the gradient of salinity given by the fresh water intake of the river Po and, therefore, both effects can be considered negligible with respect to waves. For this reasons, in this thesis the influence of the current is not considered and the focus is on the analysis of the hydrodynamics around a vertical slender cylinder subjected to wave forcing only. A vertical pile may represent a part or the whole marine structure (e.g. piers, offshore oil platform and foundation for offshore wind turbine) as in the case of monopile foundations, the most used fixed foundation in offshore wind. The better comprehension of such physical processes helps the design and permits to guarantee the integrity and the stability of the structure over time.

A key point for the design of such structure is the evaluation of the total force acting on a slender pile under wave action. Several formulations are present in the literature based on the approach of Morison et al. (1950). However, some assumptions are made to perform the analytic solution of the problem: the linear wave theory has been used for the evaluation of the velocity profile according to the potential flow theory; the involved hydrodynamic coefficients are taken constant in time and along the vertical direction; the water displacement above or below the mean water level little contributes to the total (η was small compared to the water depth h) and, thus, the integration is performed up to the mean still water level. All these restrictions are, usually, not suitable for real wave conditions in shallow/intermediate waters and could lead to high underestimations of the total loads over the structure. Several studies have been performed for the evaluation of the hydrodynamic coefficients to use in the total force formula. Sarpkaya (1976) obtained results for a wide range of *Re* and *KC* with U-tube tests while Chakrabarti (1980) performed a series of wave tank tests within a limited range of the *Reynolds* number. Moreover, several authors (Isaacson, 1979; Journée and Massie, 2001) stated that the choice of the computational method highly influences the estimation of those parameters and it could lead to a high scatter of the results. In this thesis, a series of tests on a rigid bed model has been done for the evaluation of the total force on the cylinder induced by nonlinear waves that are more representative for real field conditions. The velocity profile has been both measured and computed by means of a *Fourier* decomposition approach which gives very good results with respect to the typically used application of the linear theory.

In addition, the correct design of the foundations of these structures depends on the proper evaluation of all the parameters that play a primary role for the stability. In particular, the uncertainties on the magnitude of the maximum scour depth estimation could lead to an unsafe design. The maximum scour and its pattern need to be adequately kept in consideration while dimensioning the structure because its influence is relevant for the whole structure stability. While the scour process under steady currents has been intensively studied from the 70's (Breusers et al., 1977; Ettema, 1980; Melville, 1984), the first works in the wave induced scour over piles have been made by Sumer et al. (1992). Mobile bed tests permitted to find the first experimental relation between the dimensionless scour depth and the *Keulegan-Carpenter* parameter under regular or random waves. Carreiras et al. (2000) found results in disagreement with this equation in the case of nonlinear waves and, hence, they proposed an adaptation of the formula in this condition. More recently, Ong et al. (2013) proposed a method for the estimation of the scour depth due to random waves based on the cumulative distribution of the crest heights. For the present thesis, a mobile bed campaign has been realised in order to study the scour induced by nonlinear regular and random waves. The beginning of the scour process has been investigated and the tests are performed until an equilibrium value is reached. For regular waves, the effectiveness of the above mentioned relations is analysed and an extension of data-set for nonlinear waves has been provided and, for random waves, a new simplified method for the computation of scour depth is proposed.

In the last years, several researches have been carried out on the topic of the wave interaction with monopiles using *Computational Fluid Dynamics* (*CFD*) based *Navier-Stokes* equations. In most of these applications (e.g., Lara et al., 2013; Sun et al., 2016; Cao and Wan, 2017; Lin et al., 2017; Mohseni et al., 2018), the open source tool OpenFOAM® has been used, proving its robustness and validity, among the others, for this kind of application. In addition, OpenFOAM® is an open source

toolbox, so one of its main advantages is that it is free and the user can directly modify the source code and control each step of the solving procedure. In particular, here a new boundary condition for the correct laboratory wave generation is introduced in the solver and the results are compared with those from the laboratory. The *Reynolds Averaged Navier-Stokes* (*RANS*) model with this new boundary condition correctly generates nonlinear waves. It was possible to study the wave run-up that is another important parameter that could interfere with the access of those structures. Indeed, a wrong evaluation of this parameter could lead to safety problems if the access facilities are placed in a too low level. On the contrary, if they are placed in a too much high elevation, the access to the platform would not be comfortable in calm sea level conditions. From the physical point of view, the kinetic energy of the water is converted into potential energy because of the interaction with the cylinder (Hallermeier, 1976). The analysis of several numerical wave conditions permitted to study the reliability of the formulations available in the literature analysing and reviewing possible criticisms.
Moreover, the application of this model also permits to obtain useful information on vortex generation and growth that have been related with the scour patterns from the previous mobile bed experiments.

Objective and outline of the thesis

The aim of the present thesis is to contribute to a better understanding of the hydrodynamics and morphodynamics induced by nonlinear waves (regular ad random) in intermediate water conditions. The objective of the improvement of the knowledge of such physical processes is fundamental for a proper design of marine structures. Estimates of the force and run-up on the pile, as well as the analysis of the coherent structures around it and the scour, are all activities undertaken to reach the goals. The combined use of experimental and numerical analysis of nonlinear waves interaction with a vertical slender cylinder adds information to that already available in the literature because of the broad analysis on the dynamics and on morphological processes both by inspecting/linking a variety of results and by providing original insight into various specific mechanisms. In particular, specific attention is focused on the determination of a valid methodology for the estimation of the total force for hydrodynamic conditions in which the assumption of Morison et al. (1950)'s are not valid, often found in real cases. An accurate evaluation of the total force under nonlinear waves is not available in the literature, thus both experimental and numerical approaches were adopted aiming at collecting useful data and information on this phenomenon. The laboratory experiments have been designed mainly focusing on the reconstruction of the phase-averaged force under several wave conditions in order to find the best methods for its evaluation. The broad overview of the results may be a starting point for the evaluation of such fundamental parameter in a different way from what usually done in the design process in which nonlinear waves, typical of real sea states, are assumed to be linear waves following the assumptions of Morison et al. (1950).
Another important objective of this thesis is the evaluation of the scour depth at the base of the cylinder due to regular and random waves and to extend the dataset available in the literature. The nonlinear behaviour of waves influences the mechanics of scouring which is one of the most important causes of failure of structures in the

marine environment. Under these conditions, the available formulas and methods for the estimation of the maximum scour depth are reviewed with the extended dataset and new approaches are proposed and analysed. A mobile bed model campaign has been needed for the characterization and evaluation of morphological patterns that such waves induce on the sandy seabed.
The formation and growth of the scour is due to the intensity of the vortices that are able to catch the sediments, put them in suspension and to release them in different positions with respect to their original ones, thus leading to different seabed patterns. The present research has been undertaken in an effort to improve the understanding of the generation of vortices in relation with the equilibrium morphology of the same wave conditions. In this light, a series of *Particle Tracking Velocimetry* (PTV) tests are carried out, in rigid bed conditions, over both vertical and horizontal planes close to the bottom. Such analysis shed light on the influence of a vertical cylinder on the hydrodynamics and morphodynamics induced by waves. The available experimental data allow for a complete evaluation of a numerical model generated with a *CFD* tool (such as OpenFOAM®). Numerical modelling is usually considered a valid support to the design process and allows for information that is not easily obtainable in an experimental way without introducing a disturbance due to the presence of some sensors (e.g. free surface and velocity gauges). In particular, the evaluation of the force, the run-up and the coherent structures around the cylinder have been performed and such results contribute to the better understanding of the physical processes and, hence, can be an help during the design process.
The present thesis is structured as follows:

- Chapter 2 gives a brief description of the state of the art of the main topics regarding the present work. The hydrodynamical processes of the wave-structure interaction are described in terms of vortex generation and total force over the pile and, in addition, the scour process is also described;

- Chapter 3 describes the laboratory facilities and the employed instrumentations. Moreover, the detailed description of the two experimental configurations is reported: first the rigid bed model for force and pressure measurements and for the analysis of the velocity and vorticity field by means of PTV technique is reported, finally, the mobile bed model for the experimental evaluation of the scour is described;

- Chapter 4 shows first the main results about the hydrodynamics (velocity, force and pressure distribution) and, after that, about the morphology of the seabed concerning the scour depth under regular and random waves. Finally, the results of the PTV tests are shown and a correlation between the vortex formation, development and evolution and the seabed patterns obtained experimentally is provided;

- Chapter 5 describes the numerical model generated with OpenFOAM®, the new implemented boundary condition and the comparison of the numerical results with those obtained from the laboratory campaigns. Different analysis are carried out to confirm the vortex generation process and wave run-up;

- Chapter 6 summarizes the main findings of the present work within a critical discussion on the available and proposed design methods.

Chapter 2

Review and Theory

In this chapter an overview on the main theories and the state of the art about the topics of this thesis is reported. In Section 2.1 the flow around a vertical cylinder and the formation and evolutions of vortices is described. Section 2.2 describes the process of formation of the scour and the main formulae for its evaluation. Finally, in Section 2.3 the main studies and formulations for the evaluation of the force on slender cylinders due to waves are reported.

2.1 Flow around a single slender pile

In the marine environment, under wave action, two kind of flow regimes are possible. If the size of the pile is so small that the flow, and thus the vortices, is separated the regime is called "slender-pile". On the other hand, if the size of the body (namely the ratio between the pile diameter D and the length of the wave L) is so large that the flow is unseparated the regime is termed "large-pile" regime. Several authors (Isaacson, 1979; Sumer et al., 1997) highlighted how the diffraction effect becomes important when the ratio D/L increases over $O(0.1)$. Considering average values of diameters of offshore structures in comparison with the associated wave length, the thesis focuses on the slender pile regime.
As displayed in Figure 2.1, the three main effects due to the presence of a vertical cylinder in the hydrodynamics of the marine environment are the formation of a horseshoe vortex in front of the pile, secondly a vertical axis vortex is generated on the lee-side of the pile and, finally, the contraction of the streamlines occurs at the side edges of the pile.

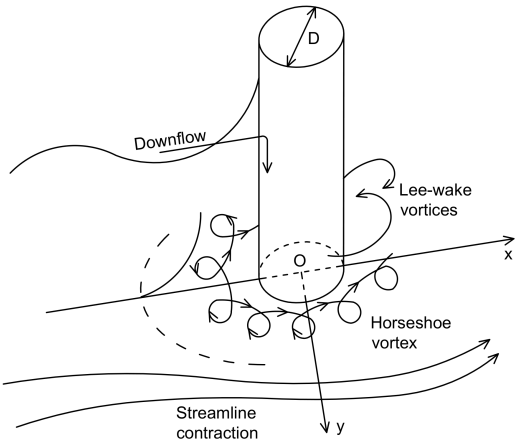

Figure 2.1: Definition sketch of the main hydrodynamic processes induced by the presence of a vertical cylinder under waves. Adapted from Sumer and Fredsøe (2002).

The bottom boundary layer due to undisturbed waves, under the influence of the adverse pressure gradient produced by the descending flow in front of the pile, does not separate up to the point in which the *Keulegan-Carpenter* parameter (KC) reaches the limiting value of $KC = 6$ and the horseshoe vortex is originated. The separated boundary layer rolls up to form a spiral vortex around the structure, which then trails off downstream. The experience of Sumer et al. (1992) confirmed how the KC is directly related to the vortex formation and, thus with the scour intensity. It is defined as:

$$KC = \frac{U_m T}{D}. \tag{2.1}$$

Hence, for a given pile diameter (D), KC depends on the maximum value of the undisturbed orbital velocity at the bed U_m and on the wave period T. Considering a linear wave, the maximum horizontal velocity can be calculated as $U_m = A\omega = \frac{2\pi A}{T}$ where A is the amplitude of the wave motion. Hence the value of KC can be calculated as:

$$KC = \frac{2\pi A}{D}. \tag{2.2}$$

The physical meaning of the KC number can probably be better explained with this equation in which the numerator represents the total amplitude of the motion ($2A$) with respect to the size of the pile D on the denominator. As this parameter increases, the water particles cover a larger distance with respect to the diameter and, thus, the probability of separation and vortex shedding increases, especially on the wake side. The lee-wake vortices are caused by the rotation in the boundary layer over the surface of the pile. The vortex flow-regimes behind a free cylinder, subjected to an oscillatory flow, have been studied by several authors. Williamson (1985) and Sumer et al. (1997) observed that the vortex flow-regimes for a free cylinder subject to an oscillatory flow and the lee-wake vortex flow are governed primarily by KC, with some influence also of the pile geometry, the pile Reynolds number and the surface roughness. The bed shear stress under the horseshoe vortex and the bed shear stress in the lee-wake are also influenced by KC. In particular, different flow regimes can be identified as shown in Figure 2.2 taken from Sumer et al. (1997):

1. when $2.8 \leq KC < 4$ a pair of symmetric vortices separate behind the pile (Figure 2.2a)
2. when $4 \leq KC < 6$ the symmetry breaks up but the vortices are still attached, no shedding occurs (Figure 2.2b)
3. when $KC \geq 6$ the vortex shedding occurs (Figure 2.2c)) and the shed frequency increases with KC (Figure 2.2d)

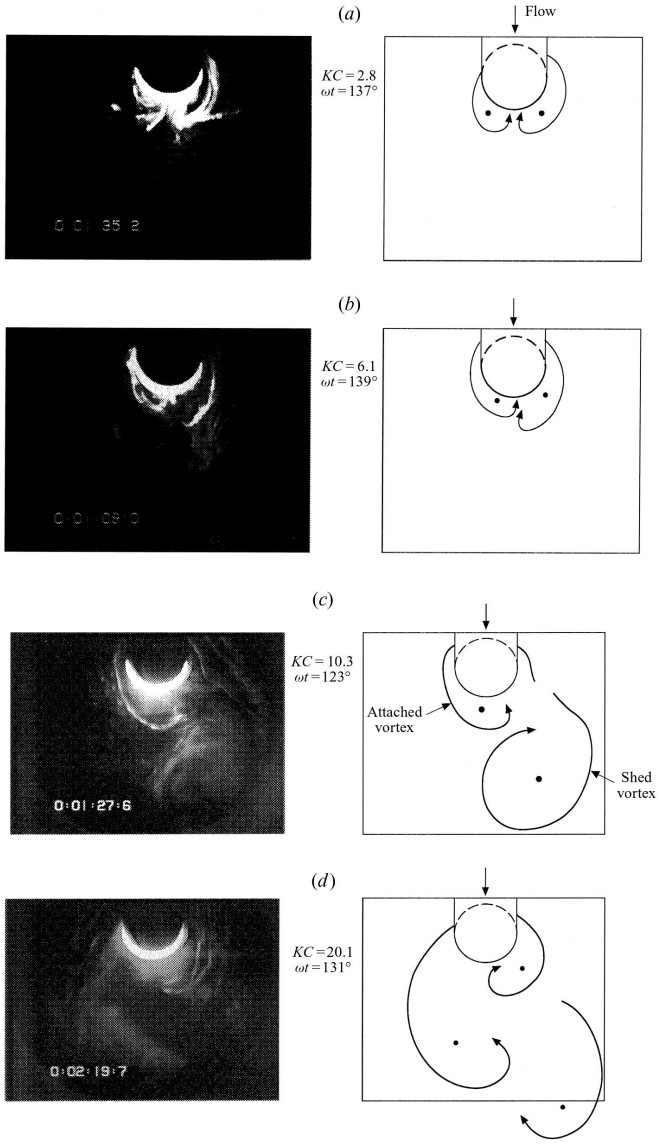

Figure 2.2: Near-bed wake vortices. Sumer et al. (1997).

In the case of steady currents (river flows, tidal currents), several studies have been done for the measurement of pressure and velocities beneath the horseshoe vortex flow

(Baker, 1979; Dargahi, 1989; Roulund et al., 2005). Baker (1979) demonstrated that the bed shear stress can be amplified by a factor of 7-11 with respect to its undisturbed value due to the very strong presence of the horseshoe vortex. For waves, instead, Sumer et al. (1997) evaluated that the amplification of the bed shear stress, defined as $\bar{\tau}_0/\bar{\tau}_{m0}$, in which $\bar{\tau}_0$ is the bed shear stress and $\bar{\tau}_{m0}$ is the maximum undisturbed bed shear stress for waves has a maximum of about $O(4)$ at (or near) the side edges of the pile for a pile subjected to waves, becoming larger than 10 in the case of steady currents (Roulund et al., 2005), when $KC \to \infty$. More recently, Baykal et al. (2017) performed numerical simulations to confirm the results of Roulund et al. (2005) for steady current and of Sumer et al. (1997) under wave conditions.

2.2 Scour process under waves

Scour around a circular cylinder is mainly forced by the horseshoe vortex combined with a downflow in front of the pile, vortex shedding behind of the pile and contraction of streamlines at the side edges (Sumer and Fredsøe, 2002). Many works have been devoted to scour around the piles. A detailed account of the topic has been given by Whitehouse (1998), Melville and Coleman (2000) and Sumer and Fredsøe (2002). Experimental investigation and dimensional analysis are the most commonly used approaches. The interaction between the flow field and the sediment motion around the pile is generally discussed in terms of dimensionless parameters. The spatial profile of the undisturbed seabed around the cylinder is largely modified by the passage of the waves. After a transient period, a periodically-steady equilibrium state is reached. When waves become the dominant forcing, the intensity of the lee-wake vortex flow, active during each half period of the oscillating motion, prevails on the horseshoe vortex and, as a consequence, the scour is produced mostly laterally or behind the pile. During a complete wave period, different flow regimes take place at the seabed around the toe of the cylinder (Sumer et al., 1992). As a consequence, different sand detachment occurs as a function of the local flow shear stress and bed slope, and modifies the slope itself, both in terms of steepness and height. Sand particles move as either bedload, i.e. rolling and translating close to the seabed, or as suspended solid, i.e. displaced away from the seabed and transported by the freestream flow. Both conditions are able to induce a net solid transport from and to different bed regions. It follows that the flow regime is strongly influenced by the seabed mobility and efforts to reproduce all the dynamics evolving at an erodible bed through use of a rigid mould may not be adequate (Manes and Brocchini, 2015).
The equilibrium scour depth S (usually normalized with the diameter of the pile) mainly depends on the characteristics of the flow, the sediment and on the roughness (k_s) of the pile. As proposed by Sumer et al. (1992) its dimensionless equation can be stated as:

$$\frac{S}{D} = f(\theta, Re_D, k_s/D, KC)$$

where $\theta = U_f^2/(g(s-1)d_{50})$ is the Shields parameter, U_f is the undisturbed bed shear velocity, s the specific gravity of sediment grains, d_{50} the grain size; $Re_D = U_m D/\nu$ is the pile Reynolds number and ν is the kinematic viscosity of the fluid ($\nu = 10^{-6} m^2/s$ for the water).
As KC increases, the length of the lee-wake vortices increases and, in addiction, the life span and size of horseshoe vortices increase. The results of Sumer et al. (1992) are shown in Figure 2.3. This figure shows that the scour tends to a constant value as $KC \to \infty$ because of the finite lifetime of the vortices. Since this value is the

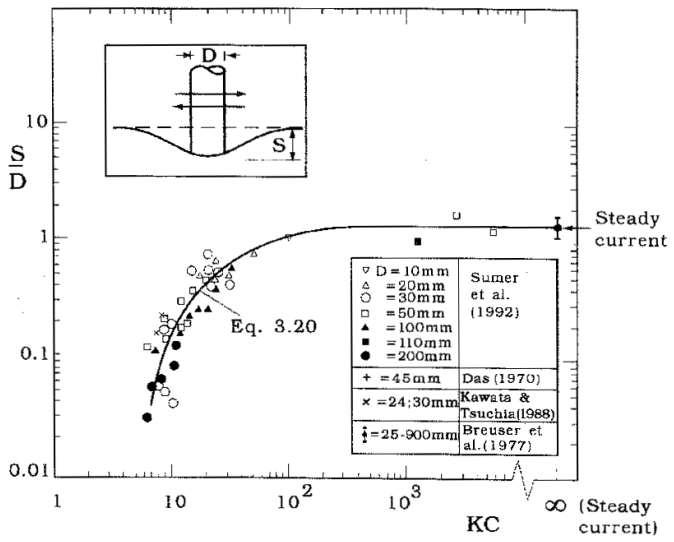

Figure 2.3: Equilibrium scour depth. Sumer et al. (1992)

same that can be obtained for steady currents ($S/D = 1.3$) it can be concluded that the contribution to the scour for large KC numbers is mainly due to the horseshoe vortices. On the other hand, if $KC < O(10)$ the net scour is directly related to the lee-vortex shedding because the life span of the horseshoe vortex is rather small. Sumer et al. (1992) gives the following expression for the evaluation of the dimensionless equilibrium scour depth depending only on the KC value.

$$\frac{S}{D} = 1.3\{1 - exp[-0.03(KC - 6)]\}; KC \geq 6 \tag{2.3}$$

Note that in the present formulation the limiting value $KC \geq 6$ is determined as a consequence of the experience of the experiments carried out by Sumer et al. (1997) that found that the limit of existence of horseshoe vortex, and thus its associated net scour, is for $KC = 6$.

An other formula have been obtained for estimation of maximum scour depth under the action of current and waves taking into account also the effect of the sediment characteristics on scouring by means of the critical velocity for the initiation of motion (U_c) of the sediment particles (Zanke et al., 2011). However, the influence of the ratio U_c/U is of primary importance for high values of KC, namely in wave-current conditions and, therefore, it is not analysed throughout this thesis. Matutano et al. (2013) analysed these methods in the context of the design of medium and large diameter monopile foundations. They reported a need for revised design formulae in terms of environmental parameters in order to determine the extent of scour protection. In the last decade, researchers have tried to improve the accuracy of scour depth estimation. More recent experimental works have been made on the scour around piers under waves and currents, most of them focused on the scour in sand-clay mixtures (Dey et al., 2011; Myrhaug and Ong, 2013), or for different cross sections (Farooq and Ghumman, 2019), or its reduction with innovative techniques (Dey et al., 2006; Corvaro et al., 2018a). In addition, *Artificial Neural Networks* have been used in hydraulic engineering problems because of their flexibility, ability to generalize and

power to approximate nonlinear and complex phenomena. As an example, Ayoubloo et al. (2010) developed a model to predict the scour depth more accurately than the conventional approach. Also *CFD* numerical models (Baykal et al., 2017) has proven successful in predicting the scour and backfilling process under waves obtaining results in full agreement with observations.

2.3 Wave force over a single pile

The correct design process of an offshore structure depends mainly on the right computation of the water wave forces. The complexity of the wave-structure interaction, the nonlinearity of the waves and the random nature of ocean waves lead to a difficulty in describing and quantifying adequately this process. An extensive review on the wave forces over structures can be found in Chakrabarti (1987) and the same information is reported also in the more recent recommended practice (Det Norske Veritas, 2010). Depending on the relative size of the structure towards the wavelength, the forces are mainly calculated in three different ways:

- *Morison* equation
- *Froude-Krylov* theory
- Diffraction theory

The *Morison* equation (Morison et al., 1950) can be used for piles that have diameters small in comparison with the wave length (namely $L > 5D$) and computes the total force as a sum of a drag and an inertial component and it uses coefficients that have to be determined experimentally. If the structure is still relatively small and the drag force is still dominant over the inertia the *Froude-Krylov* theory can be applied. According to this method the force is computed with the incident wave pressure and with the pressure-area method on the surface of the structure. If the size of the structure increases up to a point that it is comparable to the wave length ($D/L > 0.2$) the presence of the structure changes the whole wave field in its surroundings, so, in this case, the wave diffraction must be taken into account. As an example, the pile diameter of an offshore wind turbine can reach values up to 4-6m and, according with the data of Fraunhofer IEE, in 2018 more than 90% of the European offshore wind farms are placed at a water depth greater than 5. Hence, even in shallow water conditions and for short wave periods, the associated wave length takes values higher than 40m and, thus, the ratio D/L is typically smaller than the limit for the application (0.2) of the *Morison* equation.
The drag component in the *Morison* equation is given by the presence of a wake region, where the pressure is lower with respect to that one on the "upstream" side of the pile. This difference in terms of pressure leads to the generation of a force in the direction of movement of the water particles and it depends on the square of their velocity according to Equation 2.4.

$$F_D = \int_{-h}^{\eta} \frac{1}{2} \rho C_D D U |U| dz \tag{2.4}$$

in which h is the mean water depth, η is the water surface elevation from the mean level, ρ is the water density, U is the local velocity of the particles, C_D is the drag coefficient and z is the vertical coordinate which is zero at the mean water level and positive upwards.

Furthermore, the water particle that passes around the cylinder accelerates and decelerates carrying momentum with it. The resulting force over the pile is the inertial force and it is defined as:

$$F_I = \int_{-h}^{\eta} \frac{\pi}{4} D^2 \rho C_M \frac{\partial U}{\partial t} dz \tag{2.5}$$

in which C_M is the inertia coefficient.
Therefore, the total force over the cylinder due to wave action can be calculated as the linear superposition of these two contributions and the *Morison* equation is obtained by:

$$F = F_I + F_D = \int_{-h}^{\eta} \frac{\pi}{4} D^2 \rho C_M \frac{\partial U}{\partial t} dz + \int_{-h}^{\eta} \frac{1}{2} \rho C_D D U|U| dz \tag{2.6}$$

The integration of this formula can be done by means of different hypothesis. In particular, considering that the wave height is small in comparison with the water depth, it can be integrated between $-h$ and 0 and the water particle velocity and acceleration can be computed according to the linear *Airy* wave theory as:

$$\begin{aligned} U &= \frac{\pi H}{T} \frac{\cosh[k(h+z)]}{\sinh(kh)} \cos(kx - \omega t), \\ \frac{\partial U}{\partial t} &= -\frac{H}{2} gk \frac{\cosh[k(h+z)]}{\cosh(kh)} \sin(kx - \omega t). \end{aligned} \tag{2.7}$$

where g is the gravitational acceleration, $k = 2\pi/L$ is the wave number, $\omega = 2\pi/T$ is the angular frequency, L is the wavelength and x is the horizontal coordinate positive in the wave direction. Substituting Equations 2.7 in Equations 2.5 and 2.4 and integrating, the expressions for the wave force components are obtained:

$$F_D = C_D \rho g \frac{DH^2}{32} \tanh(kh) \frac{2kh + \sinh(2kh)}{\sinh^2(kh)} |\cos(kx - \omega t)| \cos(kx - \omega t), \tag{2.8}$$

$$F_I = C_M \rho g \frac{\pi D^2}{4} \frac{H}{2} \tanh(kh) \sin(kx - \omega t). \tag{2.9}$$

As already stated, the total force is calculated as the sum of the two contributions. Extensive works have been carried out to compute the hydrodynamic coefficients to use in Equation 2.6. Among the most important, it must be highlighted the work of Sarpkaya (1976) that correlated C_D and C_M to the dimensionless parameters Re and KC (Figure 2.4).

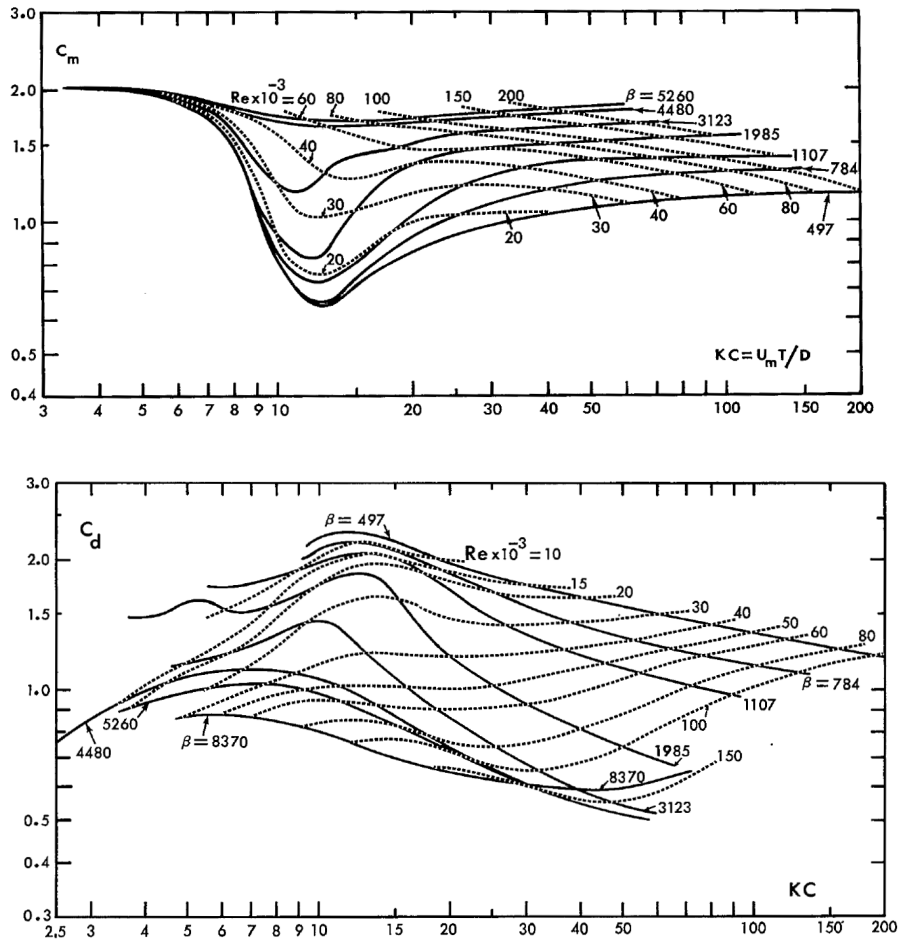

Figure 2.4: Results of Sarpkaya (1976). Evaluation of C_M (upper panel) and C_D (lower panel) with respect to KC for various values of Re or $\beta = Re/KC$.

Tests were conducted in the horizontal portion of a U-tube forced by a harmonic oscillation. More than 300 tests were conducted with different piles, analysing hydrodynamic conditions characterized by KC up to 150 and Re up to $2.5 \cdot 10^4$. The results of this work can be summarized in two figures in which the hydrodynamic coefficients depend on both the dimensionless parameters (Figure 2.4).
The wave tank tests of Chakrabarti (1980) on a vertical cylinder produced similar results in terms of C_D and C_M. In that work, a huge number of tests were performed measuring the total force and the surface elevation and reconstructing the kinetics with the stream function wave theory (Figure 2.5).

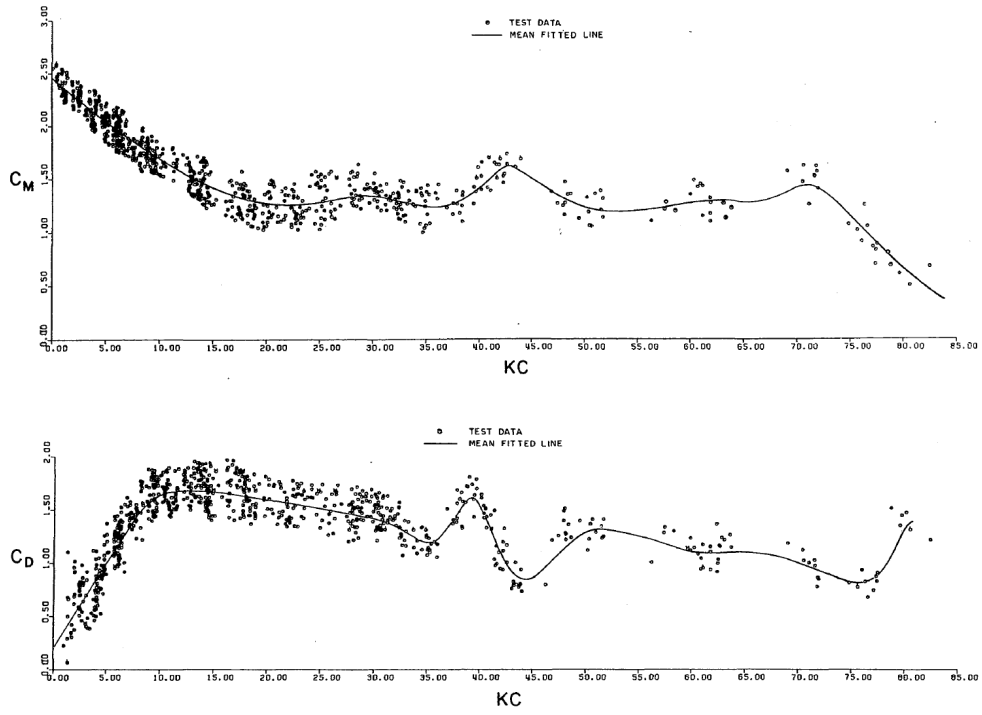

Figure 2.5: Results of Chakrabarti (1980). Evaluation of C_M (upper panel) and C_D (lower panel) with respect to KC for values of Re in the range 2-3·10^4.

A good relation with KC, ranging from 0 to 85, is obtained but the results, differently from those of Sarpkaya (1976) where the hydrodynamic conditions were better controlled by the U-tube, present a high scatter for the same KC values (e. g. for KC=5, C_D varies from 1.4 to 2 and C_M from 1.5 to 1.9).
The application of Equation 2.6 has proved to give a good estimation of the total force over a vertical cylinder until the field conditions keep similar to the assumptions made for the resolution of the problem. In particular, the limitations of the formula have been already argued by several authors (Dean, 1976; Journée and Massie, 2001; Vongvisessomjai, 1976):

- the integration is performed considering a small amplitude wave, this condition is not suitable for real waves in shallow/intermediate depths where the nonlinearity is higher and the use of linear theory for the calculation of velocity and acceleration is not recommended
- the choice of the coefficients C_D and C_M plays a primary role on the evaluation of the total force. These coefficients are obtained experimentally; among the others, Sarpkaya (1976) made an extensive work providing results obtained with U-tube tests depending on the values of Re and KC and Chakrabarti (1980) performed wave tank tests. However, these values show an elevated scatter and they are highly dependent on the type of facilities used (e.g. wave or U-tube) and on the method used for the processing of data (a more detailed description of the tests and of the results is reported in Section 4.1.2). A review of the most used

methods for the evaluation of the coefficients C_D and C_M is reported in Journée and Massie (2001), where, among the others, are explained the *Morison* method, the *Fourier* averaging technique and the least square technique. Isaacson (1979) noted how the choice of the method highly influences the results; starting from the same initial data set, each method gives a different pair of coefficients and the scatter between them can be consistent

- as highlighted also by different authors (Dean, 1976; Journée and Massie, 2001), the force measured in the drag regime can be used only for the drag coefficient evaluation and, vice versa, the inertia coefficient has to be studied with a force in the inertia regime

- when no direct measurement of water particle velocity and acceleration is available the choice of the proper wave theory for their determination is very important and it can lead to an under/over-estimation of the total wave force

- the coefficients are considered constants depending on the shape and roughness of the pile and on both the KC and Re parameters. However, in an oscillatory flow, those parameters should not be considered constant and, thus, C_D and C_M should change depending on the wave phase and, furthermore, should not be considered constant in the vertical integration of Equations 2.4 and 2.5.

For all these reasons, the choice of the right coefficients must be done considering all the exposed factors. One should know if the data set derives from U-tube or wave flume tests, if the kinematics is measured or computed and, if computed, which type of theory is used and which data processing method is used for the computation. In addition, the improvement in the calculation of the coefficients under laboratory conditions needs the verification and the validation in full-scale prototype situations.

Chapter 3

Experimental set-up and Analysis

Experimental tests were carried out at the wave flume of the Hydraulics and Maritime Construction Laboratory of the Università Politecnica delle Marche (Ancona, Italy). The general description of the flume and of the laboratory facilities is reported in Section 3.1. Two different experimental campaigns were performed to fully understand how the presence of a pile in the marine environment influences the hydro and the morpho-dynamics induced by the wave action.

- the first experimental campaign (Section 3.2) consisted in a rigid bed model for the evaluation of the total wave force acting over the pile and of the velocity field with particular attention on the vortex generation and evolution. Hence, an aim of this campaign is to evaluate the influence of the nonlinearity of the waves in comparison with the results that could be obtained considering the wave as linear. To do so, the *Fourier* decomposition approach is used for the evaluation of the velocity and the acceleration of water particles and also for the comparison of the force in conjunction with the well known formula of Morison et al. (1950). Moreover, for the better understanding of the process of formation, growth and detachment of vortices, also pressure gradients are measured. Even if they are indicated as the main responsible of the vortex detachment, not many works are carried out on these topics and, thus, further research is needed. Finally, for the visualization of vortices, the PTV technique on different horizontal and vertical planes has been applied and the results are integrated with those from pressure measurements and from the mobile bed experiments for the characterization of the scour depth and patterns. It is clear that a measurement obtained in rigid bed condition does not perfectly represents the movable bed in which the scour hole and the deposition zones affect the velocity field and, hence, the coherent structures. However, this effect can be considered negligible in the result obtained for integral variables such has the total force over the pile. Moreover, near-bed flow visualization and analysis is often studied in rigid bed conditions in the literature (Ting, 2013; Henriquez et al., 2014) because of the complexity induced by the interaction between the sediment phase with the seeding and the arduous procedure for the identification of each part (Miozzi et al., 2019).
- the second experimental campaign (Section 3.3) consists in the evaluation of

the scour patterns around the vertical cylinder associated to different wave conditions. Even if various studies have been conducted in the literature for regular and random waves, here the focus is on nonlinear waves. The aim of the study is to evaluate which type of morphological pattern is generated depending on the wave conditions and to evaluate the maximum value of the scour depth. A critical review of the available formulations in the literature is done and new approaches are studied for the scour evaluation under regular or random waves. For these reasons, a mobile sandy bed model is made and several wave conditions are tested.

The results of the experimental tests are reported in Section 4.

3.1 Laboratory facilities

The experiments were carried out at the wave flume of the Hydraulics and Maritime Construction Laboratory of the Università Politecnica delle Marche (Ancona, Italy). The wave flume (Figure 3.1) is 50m long, 1m wide and 1.3m high. The wave motion was forced by a pyston-type wavemaker that operates up to a maximum run of 0.5m (semi-stroke) and a maximum velocity of 0.8m/s.

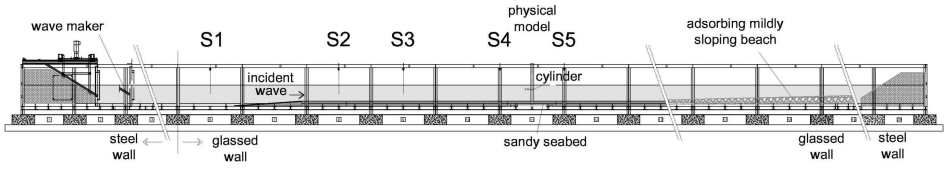

Figure 3.1: Global sketch of the wave flume for the mobile bed model realized in the Hydraulics and Maritime Construction Laboratory of the Università Politecnica delle Marche (Ancona, Italy)

An absorbing mildly sloping beach (slope 1:20) made of coarse gravel, was used to reduce the wave reflection and to guarantee an undisturbed flow in the measuring area located at about 17m from the wave paddle in order to preserve undisturbed flow conditions in the measurement area. The wave reflection was evaluated with the nonlinear method proposed by Lin and Huang (2004) and it was lower than about 4-5%. The side walls of the flume are glassed for the central 36m and enable one to videorecord and carry out optical measurements.
The acquisition of all the measuring instruments used in the present work were made by means of a home made software named *WaveLogger* that synchronizes the data by using *TTL* signals. A brief description of all the laboratory facilities is reported:

- *Free water surface gauges*: eight *HR Wallingford* electro-sensitive elevation gauges are used to measure the water level. The wave probe operates by measuring the current that flows between two stainless steel wires that are immersed in the water. This current is converted to an output voltage that is directly proportional to the immersed depth. The frequency of acquisition used is of 35Hz.

- *Pressure sensors*: four relative pressure transmitters *Keller 23SY* and four miniature ruggedized absolute pressure transducers *Kulite XTL-190SM* are used

to measure the pressure around the pile. A resistive pressure transducer has strain gauges bonded to the surface of the non-media contacted side of the diaphragm so that any change in pressure will cause a momentary deformation of the elastic material resulting in a change of the resistance of the strain gauge that is converted into a useable electrical signal. For both types of transducer the frequency of acquisition was set to 100Hz.

- *Load cell*: the biaxial shear beam load cell *Deltatech P500.BIAX-S/400N* is used to measure the total wave force on the pile. The core component of a shear beam load cell is a spring element. This element is a piece of metal that is elastically deformed under load and recovers once the load is removed. This deformation or strain is picked up by strain gauges installed on the metal element and converted into an electrical signal. The frequency of acquisition was set to 35Hz.

- *Acoustic Doppler Velocimeter (ADV)*: The *Vectrino* velocimeter, produced by *Nortek*, is used to measure the three-dimensional velocity of the water particles at specific locations around the pile and at different water depths. The instrument measures the velocity of water by using a physical principle called the Doppler Effect. The Doppler Effect is the change in frequency of a wave when a wave source moves with respect to an observer, or when the observer itself moves relative to the wave source. The *Vectrino* is a high-resolution acoustic velocimeter used to measure the three components of the water velocity within a very small sampling volume and at sample rates up to 200Hz. It is ideal for near-boundary flow measurements or to capture any highly dynamic phenomena in a hydraulic tank. The chosen frequency of acquisition was 100Hz.

- *Laser distance-meter*: the *Leica DISTO^{TM} D2* is a laser distance meter operating with a class 2 laser, used for the evaluation of the scour after the equilibrium condition is reached. A laser distance meter emits a pulse of laser at a target. The pulse then reflects off the target and back to the sending device. This "time of flight" principle is based on the fact that laser light travels at a fairly constant speed through the Earth's atmosphere.

- *Light source*: the *LED* line light *COBRA^{TM} Slim*, produced by *PROPHOTONIX*, can generate a high intensity linear light suitable for *PIV* or *PTV* applications. Three modules with a length of 100mm each one are used to generate the lighting plane. The light is white with a wave length of 550nm and a luminance of 709kLux. It is also possible to use the lamp with the strobe function in order to increase the efficacy of the illumination and to synchronize it with the *TTL* signal.

- *Scientific camera*: the camera *Flare 12M125*, produced by *IO Industries*, is a high resolution and high frequency camera with a 12MP *CMOS* sensor (4096x3072) able to acquire images at full resolution with a frame rate of 124fps. Reducing the size of the image, the frame rate could be increased up to 1863fps (with a 640x480 resolution). The camera is equipped with a *ZEISS Milvus 1.4/50* lens which has a focal ratio of 1.4 that guarantees an high level of illumination. The chosen frame rate of acquisition was 120fps.

The specific application of these instruments is exposed in the following Section 3.3 and Section 3.2 where the experimental set-up configurations are reported.

3.2 Rigid bed model

In this section the rigid bed campaign is reported. This series of experiments was carried out at the wave flume of the Hydraulics and Maritime Construction Laboratory of the Department of Civil and Building Engineering, and Architecture (DICEA) of the Università Politecnica delle Marche (Ancona, Italy) described in Section 3.1. The water surface is measured by means of 8 electro-resistive free water surface gauges at different locations of the flume positioned according to Figure 3.2.

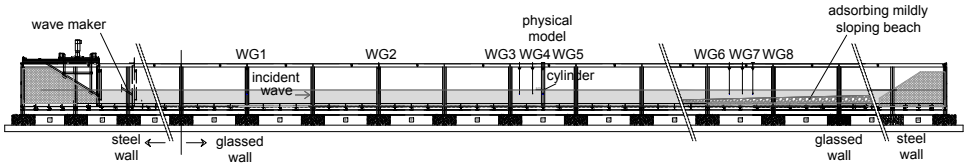

Figure 3.2: Wave gauges positioning for the rigid bed experimental campaign

In particular, two free water surface gauges ($WG1$ and $WG2$) were used to check the wave generation phase, three free water surface gauges were used in the surroundings of the model where the generate wave is stable at $\approx 3 - 5L$ from the generation ($WG3$, $WG4$ and $WG5$) and the last three ($WG6$, $WG7$ and $WG8$) were used to check the reflection in correspondence of the adsorbing beach at the end of the flume. The model has been made in rigid-bed conditions for the evaluation of the hydrodynamic and kinematic characteristics of the flow. In the study area it was placed a vertical cylinder made by PVC with a diameter D=11cm.
The pile was equipped with eight pressure transducers placed over the same vertical line at different depth from the bottom as shown Figure 3.3a.
The 4 lower sensors (*Keller 23SY*) are placed at 8-16-24-32cm from the bottom. The others (*Kulite XTL-190SM*) are placed in the surroundings of the free surface at 40-50-55-60cm. At the bottom of the pile there was a hinge which allow the complete rotation around its axis (yaw) and a very limited (<15°) rotation on the longitudinal and transversal ones (pitch and roll). In fact, the pile was fixed by means of a load cell *Deltatech P500.BIAX-S/400N* at the top of it for the total force measurement. The pressure sensors were placed along the same vertical line, so, in order to obtain a good discretization of the pressure distribution around the cylinder, it was necessary to repeat each wave condition 7 times. After each test the cylinder was rotated by 30° to modify the reference position as shown in Figure 3.3b (φ from 0° to 180° where 0° corresponds to the stagnation point using the same reference system described in Figure 3.9). The water gauge $WG5$ was placed in correspondence of the pile, on its lateral side, at 30cm from it and was used for the measurement of the reference water level over the pile and the synchronization of the different tests within the same wave conditions.

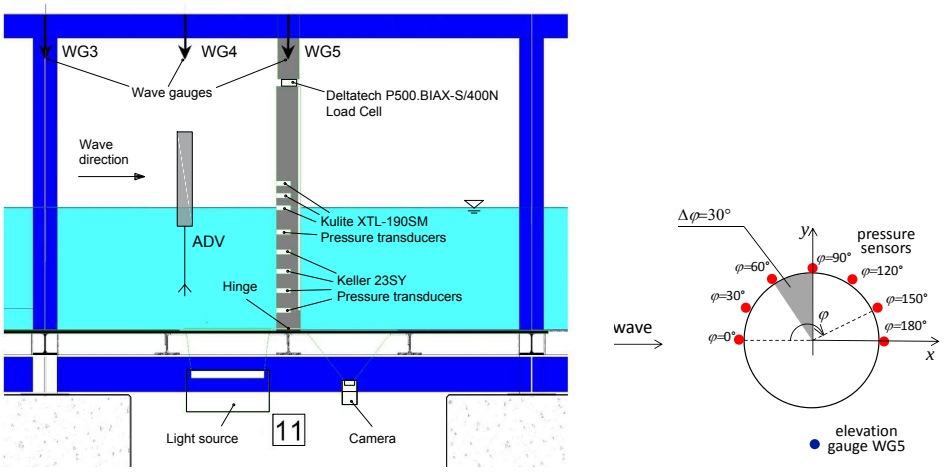

Figure 3.3: Longitudinal cross-section of the physical rigid bed model and measurement instruments (a) and sketch of the rotations in which pressure measurements are performed (b)

The analysis of the velocity of the particles has been carried out by means of the ADV at different depths z_b from the bottom of the flume (from z_b=4cm to z_b=37cm). The ADV is placed before the cylinder, in correspondence of the wave gauge $WG4$ in order to obtain a vertical distribution of the velocity which can be representative of the wave that impacts on the pile but not so close to it to be affected by its presence ($> 2D$ for the tested range of KC according to Sumer et al., 1997). In any case, when velocity measurements are performed, no measurement of pressure and force over the pile are carried out because of the possible influence on the results by the presence of the "obstacle" before the pile (Figure 3.3a). Meanwhile the wave-maker was running, the velocimeter was lifted among the different depths and, in each position, velocity measurements were performed until a satisfactory number of waves were recorded for the evaluation of the mean characteristics of the periodic phenomenon (more than 30). The main disadvantage of this procedure is that the time series of velocity measurements does not corresponds to that of pressures and force. In the first case, the record starts with a completely developed flow and lasted for approximately 60s, while each pressure measurement starts in quiet conditions and reaches the steady condition after a ramp time period.
Moreover, Figure 3.3a shows the presence (before and after the pile) of a lighting system and a camera. Optical measurements (PTV technique) were possible thanks to the glassed lateral wall and two glassed windows on the bottom of the flume. The analysis by means of optical measurements of the velocity and vorticity field induced around the pile, allow to better understand the conditions of generation and separation of coherent structures, such as lee wake vortices. In order to reconstruct the three-dimensional dynamics around the cylinder, both horizontal and vertical planes have been analysed by PTV measurements. 17 regular wave tests were performed with a constant water depth of h=0.50m; each test lasted for 5min (≈100-150 waves). The wave characteristics of the rigid bed experiments are summarized in Table 3.1.

Table 3.1: Characteristics of regular waves at wave gauge $S4$ for rigid bed model.

Name	H (m)	T (s)	Re ($\times 10^4$)	KC (-)	Ur (-)	L (m)
R2	0.19	2.74	7.0	10.0	52.0	5.80
R3	0.19	2.74	8.3	10.8	50.0	5.80
R5	0.19	1.83	3.5	5.8	20.1	3.64
R6	0.22	1.83	4.4	6.5	23.6	3.64
R7	0.16	1.83	2.3	4.7	16.8	3.64
R8	0.16	2.19	2.8	5.6	25.8	4.51
R9	0.19	2.19	5.1	7.6	31.3	4.51
R10	0.20	2.19	6.8	8.8	33.1	4.51
R15	0.13	2.74	3.3	6.8	35.9	5.80
R17	0.16	2.74	4.8	8.2	41.7	5.80
R21	0.16	2.00	2.9	5.4	21.1	4.06
R22	0.19	2.00	3.9	6.3	25.0	4.06
R23	0.23	2.00	4.8	7.1	30.5	4.06
R24	0.15	2.35	2.6	5.6	28.2	4.89
R25	0.17	2.35	3.5	6.5	32.0	4.89
R26	0.20	2.35	4.4	7.4	37.6	4.89
R27	0.21	2.35	5.9	8.5	39.8	4.89

Different wave periods (T) were analysed from 1.83s to 2.74s associated to different wave heights (H) in the range 0.13-0.23m.
The wave conditions reach the maximum values of $KC = 11$ and $Re = 8 \times 10^4$, but, for most of the tests, the $Ursell$ parameter is below the threshold value of 40 for the application of the linear theory (detailed description in Section 3.3).
Other important dimensionless parameters for the determination of the hydrodynamic regime (see Chakrabarti, 1987), are $\pi D/L$ and H/D. The results for the experimental wave conditions are plotted in Figure 3.4.

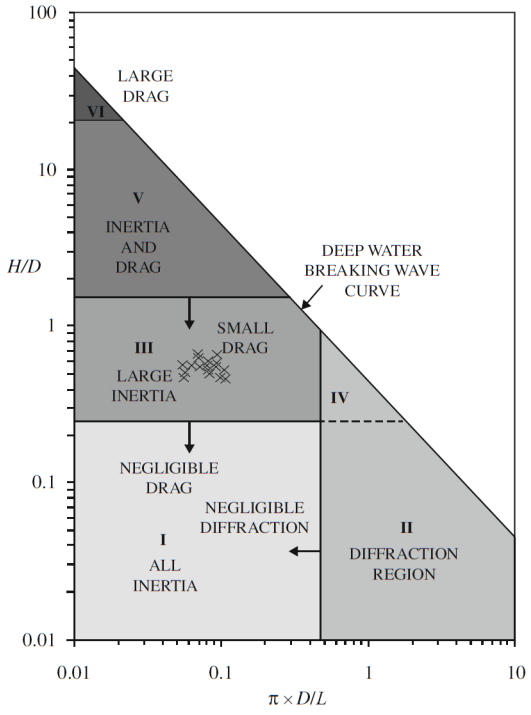

Figure 3.4: Regime classes of drag and inertia forces (Chakrabarti, 1987)

Therefore, in this campaign the inertia component on the total force is dominant but the drag contribution cannot be considered negligible. However, as already stated, different authors (Dean, 1976; Journée and Massie, 2001), stated that if one regime is dominant on the other, only the evaluation of the corresponding coefficient can be considered reliable.
The pile of the rigid bed model was equipped with a hinge at the bottom and it is fixed with the load cell on the other end at the upper side. According to this set-up, the measured horizontal force at the load cell is elaborated to obtain the wave force over the pile that depends on the lever arm between the line of application of the force and the hinge (b_w). Knowing the distance between the load cell and the hinge (b_c=1.04m) and estimating for each time the distance b_w, the wave force is computed. The estimation of this distance is performed according to the methodology presented in the Shore Protection Manual (Coastal Engineering Research Center, 1984) where the values are obtained by the integration over the surface of the pile using the *Airy* wave theory. The lever arm of the wave force, hence, depends on the dynamic regime of motion. For the inertia regime it can be written as:

$$b_{W,inertia} = h\left(1 + \frac{1-\cosh(2\pi h/L)}{(2\pi h/L)\sinh(2\pi h/L)}\right) \tag{3.1}$$

while for the drag regime:

$$b_{W,drag} = h\left(1/2 + \frac{1}{4n_w} + \frac{1-\cosh(4\pi h/L)}{2n_w(4\pi h/L)\sinh(4\pi h/L)}\right) \tag{3.2}$$

in which $n_w = C_g/C$ is the wave group factor, C is the wave velocity and C_g is the wave group velocity. Note that the difference between those formulations is very small. Anyway in the further elaborations, under the wave crest phase (when the velocity and, thus, the drag are maximum) Equation 3.2 is used, while in the phases in which the acceleration is maximum, Equation 3.1 is used. An interpolation between those equations is used for the remaining phases.
A calibration process of the load cell has been performed, applying different controlled horizontal forces (F_w) at different depths (b_w), knowing the position of the load cell (b_c) and recording the force (F_c).

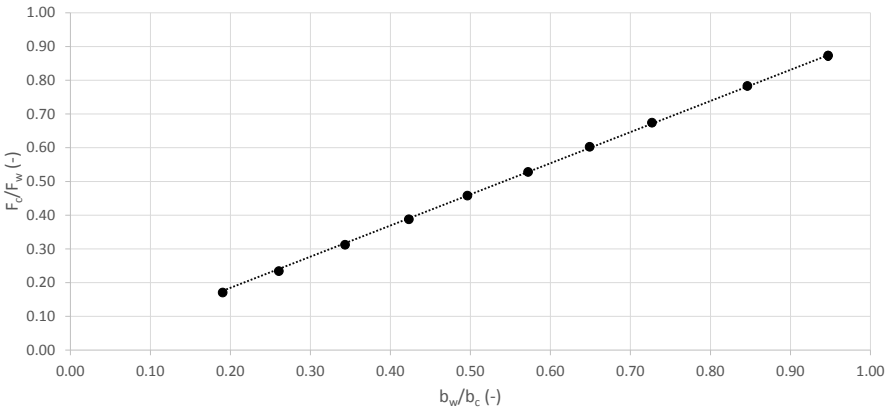

Figure 3.5: Load cell calibration: linear relation between the dimensionless ratios F_c/F_w and b_w/b_c

In Figure 3.5 the results of the calibration process are shown. In particular, a linear relation ($r^2 = 0.9997$) between the dimensionless measured forces and their relative lever arms is found (Equation 3.3).

$$\frac{F_c}{F_w} = 0.9233\frac{b_w}{b_c} \tag{3.3}$$

Hence, the wave force is computed estimating the lever arm with Equations 3.1 and 3.2 and re-arranging Equation 3.3 to:

$$F_w = 1.083\frac{b_c}{b_w}F_c \tag{3.4}$$

An indirect verification of the goodness of this method is achieved by the comparison between the force computed with this equation and that obtained from the integration of the pressure distribution recorded around the pile. Although the discretization of the pile surface is not much detailed ($\Delta\varphi = 30°$, $dz \approx$10cm), the qualitative results obtained confirm the reliability of the procedure (Figure 3.6).

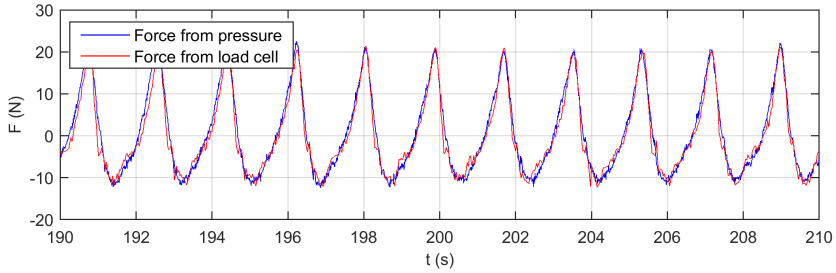

Figure 3.6: Comparison between the force computed from the load cell measurements (F_w) and that from the integration of the pressure on the surface of the cylinder.

The goodness of the comparison confirms the validity of the model just described. A very small scatter is recorded on the wave crest and though phase, possibly due to the integration of the pressure sensors that are not representing the whole surface of the pile but just a discretization of it (every 30° with dz that varies from 5 to 12cm).

3.2.1 Particle Tracking Velocimetry set-up

Among the optical methods for the undisturbed fluid velocity measurement, the *Particle Tracking Velocimetry* (PTV) technique plays a primary role. When the seeding concentration is low, a *lagrangian* approach is used; single particles are tracked between different frames and the velocity field is hence reconstructed. The accuracy of both methods depends on the effectiveness of the illumination, usually done by means of a laser with pulsed or continuous light to guarantee a high visibility of the seeding particles introduced in the system. The size of the particles must be chosen adequately (Hadad, 2013). In particular, their diameter must be small enough to improve the quality of the tracking but large enough to guarantee a good illumination of each particle. Moreover, the seeding size has to be as uniform as possible in order to avoid an higher brightness of the bigger particles that causes a disturbance over the image and a wrong evaluation of the characteristics of the smaller ones. The PTV technique allows the tracking of the particles referring their characteristics on a local

coordinate system which moves with the particle at each frame. The position of the centre of gravity of the particles in two following images is used to identify which is their trajectory (Lewis et al., 1987; Kobayashi et al., 1989) depending on criteria of maximum displacement, maximum acceleration and on the existence of a prevalent direction of fluid motion.
Due to the high computational costs, PTV analysis is only performed for tests $R2$, $R8$, $R9$ and $R15$, among the wave conditions of Table 3.1, with the same configuration of Figure 3.3. Those conditions are chosen in order to have values of KC in the range from 5 to 10, which is significant for the vortex generation. The phenomenon of vortex formation is highly three-dimensional and, thus, for its analysis a volumetric approach with a set-up made by at least 3 cameras (Miozzi et al., 2019) is recommended. However, as already done in the literature, in this thesis the three dimensional problem has been simplified, by passing from a $3D$ problem to a series of $2D$ problems. The volume of interest is analysed by means of several horizontal planes at different heights from the bottom (Figure 3.7a) and two vertical planes along the centre line of the flume (Figure 3.7b), before and after the pile.

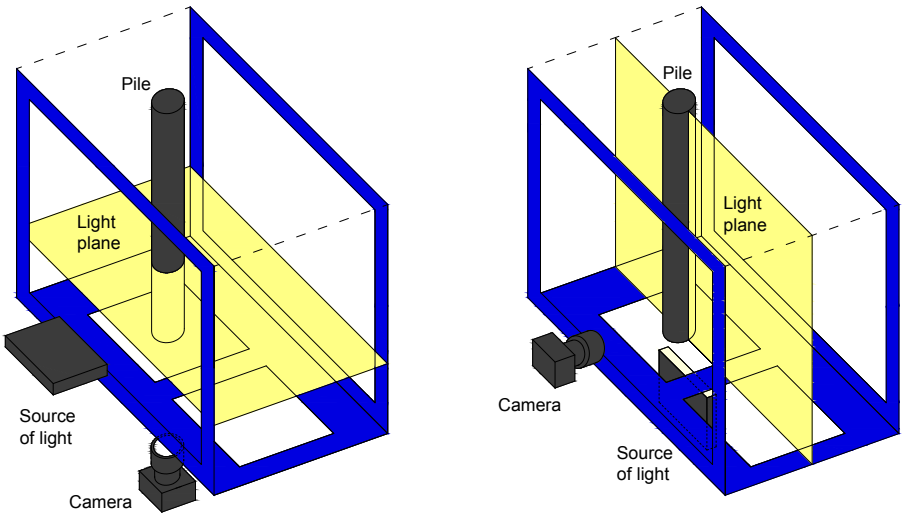

Figure 3.7: Sketch of the PTV tests configurations: camera on the bottom of the flume for horizontal plane recordings (panel a), camera on the lateral side of the flume for vertical plane recordings (panel b)

Before each test, the calibration of the image field has been performed with a specific target, perpendicular to the camera which allows to set up the focus of the lens and to evaluate the correct ratio between image (px) and real (cm) dimensions. The vertical planes are useful to obtain information on the generation of the horseshoe vortices on the bottom of the flume. Horizontal planes are studied at different values of height from the bottom (z_b=4.6cm, 10.6cm, 20cm and 30cm) to evaluate the intensity and the detachment of lee-wake vortices. Because of the dimension of the camera, of the available space under the flume and of the focal length of the lens, the horizontal plane closest to the rigid bottom was at z_b=4.6cm, because it was not possible to analyse planes with z_b <4.6cm which resulted out of focus.

3.3 Mobile bed model

The mobile bed campaign consisted in a physical model with a length of 1.5m, a width of 1m and seabed thickness of 0.16m performed in the wave flume of the Hydraulics and Maritime Construction Laboratory of the Department of Civil and Building Engineering, and Architecture (DICEA) of the Università Politecnica delle Marche (Ancona, Italy) described in Section 3.1. In the central part of the mobile seabed a vertical steel cylinder with a diameter D=10cm was fitted (see Figure 3.8). The diameter of the cylinder in this model is slightly different from the one in PVC used in the rigid bed model ($D = 11cm$) because of the commercial sizes of the different materials. Two values of still water depths (h) over the physical model were used: 50cm and 40cm. Twenty regular waves (fifteen with water depth of 50cm and five with 40cm) and nine random waves (water depth of 50cm) were tested. The mobile seabed was made of sand with mean diameter d_{50}=0.6mm, standard deviation σ=0.21mm, density ρ_s=2630Kg/m^3 and uniformity parameter (defined as $\sigma_D = 1/2(d_{84}/d_{50} + d_{50}/d_{16})$) equal to 1.25. The grain size statistical parameters were evaluated by using the graphical techniques of Folk and Ward (1957).

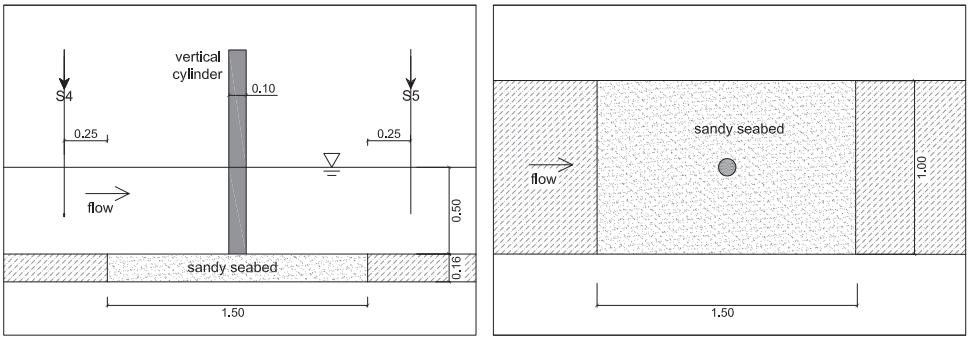

Figure 3.8: Longitudinal cross-section (left panel) and plan view (right panel) of the physical mobile bed model.

The model has been designed accordingly to the indications given in Whitehouse (1998). In particular, the blockage ratio, defined as the ratio between the pile diameter and the width of the flume ($\approx 1/10$) is kept smaller than 1/6 as suggested and water depth effects are avoided because $h \geq 4D$. The water level evolution, and thus wave heights, at different locations of the flume was measured and monitored by seven electro-sensitive free surface gauges (see Figure 3.1). In particular, elevation gauges $S4$ and $S5$ were placed, respectively, upstream and downstream of the cylinder at a distance of 1.0m from the centre of the pile (see Figure 3.8). The incident wave characteristics were measured at wave gauge $S4$. The water surface time series did not display disturbed profiles, in agreement with Van Weele and Herbich (1972) that found an averaged pile reflection of about 5%, hence, as usually done in the literature, reflection off the pile has been taken to negligibly influence the wave height.
For both regular and irregular waves after each test the water was removed from the wave flume to measure the seabed elevation in dry condition. In order to maintain an unaltered seabed a very slow draining process was induced; in particular for this experimental setup, 2 days was a conservative time period to achieve the required

dry and unaltered seabed morphology. The scour depth was measured over a grid of 1cm×1cm by using a laser distance meter located at a fixed and known vertical distance from the horizontal bottom and by moving it over a regular horizontal grid with the same spacing of 1cm×1cm. No reflection due to the undrained water in the soil was observed.

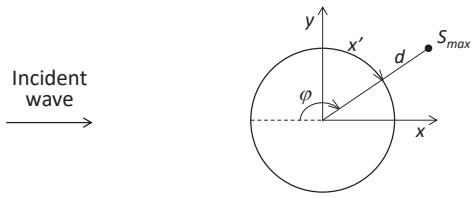

Figure 3.9: Sketch of the reference systems used in this work.

These values were interpolated and plotted as a surface in an orthogonal Cartesian x, y, z coordinate system, where the x axis was in the direction of the flow with the wave propagating from negative to positive values; the y axis was horizontal and transversal to the incoming wave direction and z was vertical, coinciding with the pile's axis. To identify the location of the maximum scour, the distance d from the centre of the pile has been used: $d = (x^2 + y^2)^{0.5}$. Two additional coordinate systems have been used: curvilinear (x') and angular (φ) coordinates. The x' coordinate gave the distance along the cylinder surface from the stagnation point. φ was the angle measured from the x axis and centred in the middle of the pile. The reference systems are illustrated in Figure 3.9.
Table 3.2 shows the characteristics of the tested regular waves, measured at wave gauge $S4$.

Table 3.2: Characteristics of regular waves at wave gauge $S4$.

Name	h (m)	H (m)	T (s)	Re_D ($\times 10^4$)	KC (-)	Ur (-)	ε (-)	θ (-)
R0	0.5	0.12	1.83	2.2	4.0	13.1	0.243	0.04
R1	0.5	0.14	2.74	3.0	8.1	40.2	0.290	0.06
R2	0.5	0.21	2.74	4.3	11.7	57.5	0.415	0.11
R3	0.5	0.28	2.74	5.7	15.7	77.3	0.557	0.19
R4*	0.5	0.35	2.74	7.1	19.6	96.7	0.697	0.28
R5	0.5	0.20	1.83	3.7	6.7	22.2	0.409	0.10
R6	0.5	0.25	1.83	4.4	8.0	26.7	0.492	0.13
R7	0.5	0.16	1.83	2.9	5.2	17.4	0.321	0.06
R8	0.5	0.16	2.19	3.1	6.8	27.0	0.321	0.07
R9	0.5	0.19	2.19	3.7	8.1	32.3	0.384	0.09
R10	0.5	0.23	2.19	4.5	9.9	39.1	0.465	0.13
R11	0.5	0.14	2.19	2.8	6.1	24.1	0.286	0.06
R12*	0.5	0.36	2.74	7.4	20.2	99.9	0.720	0.30
R13	0.4	0.17	2.74	3.9	10.8	74.2	0.421	0.10
R14	0.4	0.19	2.74	4.5	12.3	84.5	0.479	0.12
R15	0.5	0.17	2.74	3.6	9.8	48.4	0.349	0.08
R16	0.4	0.14	2.19	3.1	6.7	37.3	0.344	0.07
R17	0.5	0.19	2.74	3.9	10.6	52.1	0.376	0.10
R18	0.4	0.16	2.19	3.7	8.0	44.3	0.408	0.09
R19	0.4	0.21	2.19	4.8	10.4	57.6	0.531	0.15

Note: * Breaking wave.

Here h is the water depth, H is incident wave height, Re_D is the pile Reynolds number, θ is the *Shields* parameter, KC is the *Keulegan-Carpenter* number and, lastly, ε is the wave nonlinearity and Ur is the *Ursell* number, which are defined as follow:

$$\varepsilon = \frac{H}{h} \quad , \qquad Ur = \frac{HL^2}{h^3}, \tag{3.5}$$

The presence of a seaward ramp, needed to reproduce the mobile seabed model, altered both the shape and characteristics of the generated waves (as observed by the elevation gauges located along the wave flume, see Figure 3.1). The Ur number, evaluated at wave gauge $S4$, was large because of the nonlinearity of the measured waves: the wave crest became shorter in time and more peaked, the intensity of the flow was higher compared to a linear wave, flow reversal occurred for wave phase ωt smaller than 180° as for a sinusoidal wave, the wave trough was flattened and its amplitude decreased.
Figure 3.10 shows the free surface evolution for different values of Ur.

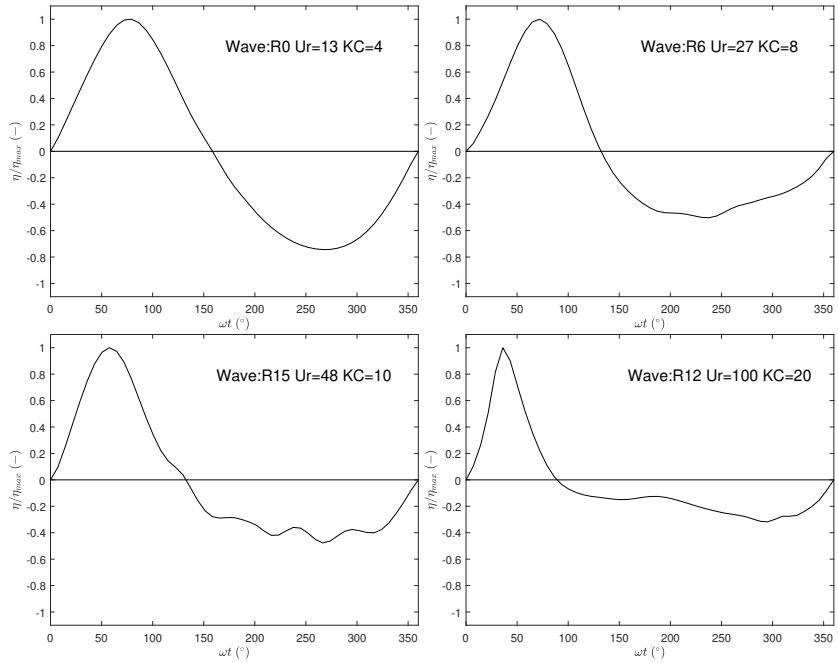

Figure 3.10: Phase-averaged water surface elevation at wave gauge $S4$. Waves R0, R6, R15 and R12.

Wave R0 was characterized by the smallest value of Ur ($Ur \approx 13$), it was almost sinusoidal but a small difference between the crest ($\approx 6cm$) and the trough ($\approx 5cm$) could be appreciated. By increasing Ur, the nonlinearity grew and the shape of the wave changed substantially. The maximum value of Ur (≈ 100) was reached for wave R12 where the free surface evolution became similar to that of a cnoidal wave (peaked crests and flat troughs), the wave led to breaking condition. Hence, the role of the wave nonlinearity should be taken into account when evaluating the scour process. The wave condition at the wavemaker corresponds to those of the mobile bed

campaign, however here the *Ursell* parameter at the pile is lower, because the wave propagates in a horizontal bottom, with the absence of the ramp that was responsible of nonlinear effects on the wave shape.
Combinations of two different water levels h (50cm and 40cm), three wave periods T (1.83s; 2.19s and 2.74s) and different wave heights H (0.12m-0.36m) were studied and the resulting KC of all the experiments were in the range 4-20. Larger values of KC were not used in this experimental setup (wave alone conditions and a single pile diameter D=10cm), because the waves started to break at $KC \approx 20$ (waves R4 and R12) and hence larger values of U_m were not obtained.
KC has been evaluated by means of Equation 2.1 where U_m has been computed according to the linear theory: $U_m = \omega a/\sinh(kh)$. In previous studies (Corvaro et al., 2014; Miozzi et al., 2015) the authors found a small discrepancy between measured and predicted (by linear theory) horizontal velocity over an impermeable bed, even for waves characterized by significant asymmetric free surface profile. In particular, it was found that the difference of the horizontal velocity between the linear theory and the measured data was smaller than 5% for Ur <40, and for Ur >40 the linear theory under-predict the measured data. The maximum discrepancy was of about 15%, hence, the errors in the computation of U_m and, thus, of KC can be considered as acceptable. Such consideration is also confirmed by Le Méhauté (1976), which shows that the horizontal velocity can be well predicted by the linear theory, even if the water surface elevations displays strong nonlinearities.
Table 3.3 summarizes the characteristics of the random waves.

Table 3.3: Characteristics of random waves at wave gauge $S4$.

Name	h (m)	H_s (m)	T_p (s)	Re_D ($\times 10^4$)	KC_{rms} (-)	ϵ (-)	$Ur_1(-)$	$S_1(-)$	θ_{rms} (-)
NR1	0.5	0.12	2.69	2.4	6.4	0.984	1.09	0.015	0.04
NR2	0.5	0.15	2.66	3.0	8.0	0.958	1.36	0.019	0.06
NR3	0.5	0.19	2.77	3.7	10.1	0.961	1.79	0.021	0.09
NR4	0.5	0.21	2.69	4.0	10.7	0.970	1.84	0.025	0.10
NR5	0.5	0.16	1.91	3.0	5.7	0.999	0.70	0.041	0.07
NR6	0.5	0.18	1.82	3.3	6.0	0.987	0.70	0.051	0.08
NR7	0.5	0.14	2.24	2.8	6.3	0.993	0.90	0.026	0.06
NR8	0.5	0.17	2.15	3.2	6.8	0.991	0.94	0.033	0.07
NR9	0.5	0.20	2.11	3.7	7.7	0.988	1.03	0.040	0.09

Here, H_s is the significant wave height, T_p is the peak period and KC_{rms} corresponds to the rms value computed according to Ong et al. (2013) as:

$$KC_{rms} = \frac{2\pi a_{rms}}{D\ \sinh(k_p h)} \tag{3.6}$$

where k_p is the wave number corresponding to the peak frequency $\omega_p = 2\pi/T_p$, $A_{rms} = \sqrt{2}\sigma_\eta$ and $\sigma_\eta^2 = \int_0^\infty S_\eta(f)\ df$ where $S_\eta(f)$ is the wave spectrum of the instantaneous free surface elevation $\eta(t)$. Note that by using in Equation 2.1 the rms value of U_m computed according to the linear theory, i.e. $U_{rms} = \omega A_{rms}/\sinh(k_p h)$, Equation 3.6 is recovered.
For random waves, the Ursell number Ur_1 and the wave steepness S_1 are, respectively, defined as:

$$\begin{aligned} Ur_1 &= \frac{H_s}{k_1^2 h^3} \\ S_1 &= \frac{2\pi}{g}\frac{H_s}{T_1^2} \end{aligned} \tag{3.7}$$

where H_s is the significant wave height, T_1 the spectral mean wave period and k_1 its corresponding wave number. The definition of the *Ursell* number here used for random waves has been proposed by Forristall (2000), and differs from that widely used for regular waves (see Equation 3.5) by a factor $1/(2\pi)^2$.
The spectral width parameter introduced by Cartwright and Longuet-Higgins (1956) is defined as:

$$\epsilon = \left(1 - \frac{m_2^2}{m_0 m_4}\right)^{1/2} \tag{3.8}$$

The nonlinearity induced by the presence of the ramp at the beginning of the flume was confirmed by the large values of *Ursell* number. Furthermore, the values of ϵ of these experiments were close to unity, meaning that the spectrum had to be taken as broad-banded and the wave height distribution was not suited for application of the Rayleigh theory. The probability exceeding the reference peak was compared both with the *Rayleigh* and Klopman (1996) distribution (Figure 3.11). Here, both distributions were applied to the crest height η_c instead of the wave height H, to take into account the effects of nonlinearity.

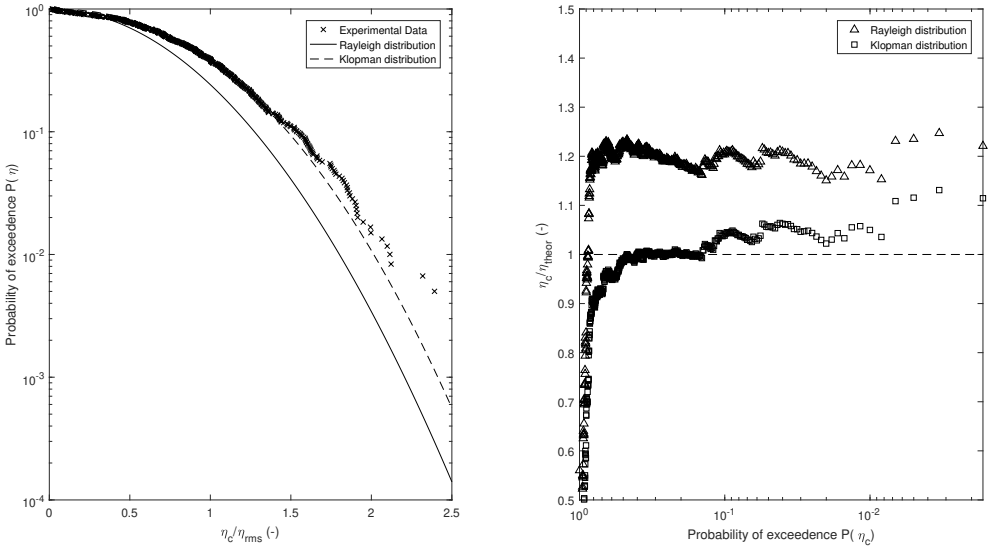

Figure 3.11: Left panel: comparison of the experimental exceeding probability of the dimensionless crest heights with both *Rayleigh* and *Klopman* distributions (the crest heights η_c are normalized by the *rms* crest height). Right panel: comparison of the crest height normalized with the crest height predicted at given exceeding probability levels by both *Rayleigh* and *Klopman* distributions. Non-linear random wave test NR6.

The scatter between the experimental data and the Rayleigh solid line confirms the nonlinearity of the random waves. Therefore, the Rayleigh distribution cannot be taken as suitable for the random wave conditions of the present study. However, the Klopman (1996) distribution, which better represents random waves in finite waters, fits better the probability of exceedance of the tests of the present study.

Time scale of scour

The scour develops towards the equilibrium stage (equilibrium scour depth) through a transient period, as noted by Sumer and Fredsøe (2002). The analysis starts by determining the time scale of the scour evolution. As described by Sumer and Fredsøe (2002), such time scale can be defined as:

$$T_S = \frac{D^2}{(g(s-1)d_{50}^3)^{1/2}} T^* \tag{3.9}$$

where $T^* = 10^{-6}(\frac{KC}{\theta})^3$ is the dimensionless time scale ($KC = KC_{rms}$ has been used for random waves), which depends on the Shields parameter computed according to its definition reported in Section 2.2. Tables 3.2 and 3.3 summarize the values of the Shield parameters obtained for both regular and random waves. Furthermore, the critical Shields parameter for the sediment initiation of motion can be defined as proposed by Soulsby (1997):

$$\theta_{cr} = \frac{0.3}{1 + 1.2d_*} + 0.055[1 - \exp(-0.02d_*)] \tag{3.10}$$

in which $d_* = d_{50}[(s-1)g/\nu^2]^{1/3}$ is the dimensionless grain size. In the present study θ_{cr} was equal to 0.03. For both regular and random waves of the present experiment the values of θ and θ_{rms} are always larger than θ_{cr} (see Tables 3.2 and 3.3), hence condition of "live-bed" scour was obtained. This is in agreement with the tests of Sumer et al. (1992) performed in live bed conditions, for which the value of the Shields parameter (in the range 0.04 to 0.37) was very similar to this campaign (see Table 3.2) and it had no discernible effect. For each regular wave, the time scale T_S of Equation 3.9 is always smaller than 500s ($T_S \cong$50s-500s), so every experiments cautionary lasted 10min (see Figure 3.12 as an example for wave $R15$).

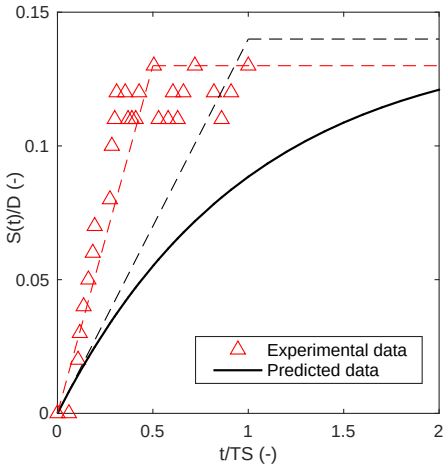

Figure 3.12: Time evolution of the measured and predicted scour depth $S(t)/D$ for wave $R15$: predicted data (black), measured data (red). Dashed lines represent the tangent to the curve at the origin (from $t/T_S = 0$ to $t = T_S$) and the horizontal asymptotic limit for $t \to \infty$.

Figure 3.12 shows the comparison in time between the measured and predicted dimensionless scour depth $S(t)/D$ around the surface of the cylinder, with $S(t)$ being defined as:

$$S(t) = S(1 - \exp(-t/T_S)) \tag{3.11}$$

in which S is the equilibrium scour depth. The timescale needed to reach the equilibrium scour depth (red dotted line in Figure 3.12) was found to be about one-half of the predicted value. After about 70 wave cycles, the system leads to an equilibrium state where the bed morphology changes only over the wave phases.
For random waves, the length of each test was primarily chosen in order to guarantee that a complete wave packet could be analysed (around 500 waves). The test duration was in the range of 16min-24min, depending on the wave peak period T_p. Application of Equation 3.9 for random waves led to values of T_S $\cong$90s-600s, hence smaller or equal to 10min. Therefore, the durations used for random wave tests were sufficient to achieve equilibrium scour condition.

Chapter 4

Experimental Results

In the present chapter the main results of the two experimental campaigns are reported. In particular, the results are arranged in the order that better explain the obtained achievements in relation with the objectives of the thesis (see Section 1). In Section 4.1.1 an analysis of the undisturbed wave kinematic is made in order to compare the experimental data with the theoretical ones obtained or by the application of the linear wave theory or by using a *Fourier* decomposition method to take into account the wave nonlinearity. Moreover, the analysis of the total force over the pile is performed (Section 4.1.2). The *Fourier* decomposition method is applied to all the tested waves in order to evaluate its effectiveness for the evaluation of both the peak force (maximum force) and its occurrence (wave phase in which the maximum force occurs). In this section, the results are also compared with those obtained with the linear wave theory which represents the usual practice formula applied in the design process. Section 4.1.3 reports the results concerning the pressure distribution around the pile and the estimation of the pressure gradients. The presence of adverse pressure gradients is highlighted as one of the main effects of the generation and transport of vortices around the cylinder but their direct measurement is not usually done in the literature. The results of the mobile bed campaign are reported in the following sections. In particular, in Section 4.2.1 the effect of nonlinear regular waves on a sandy seabed is analysed in order to evaluate the maximum scour and the threshold scour conditions; the results are hence compared with the main formulas available in the literature (Sumer et al., 1992; Carreiras et al., 2000). For the evaluation of the scour under random waves, in Section 4.2.2 a modified version of the Ong et al. (2013)'s method is proposed to take into account the cumulative distribution of the crest heights. Finally, to improve the understandings of the generation of vortices in relation with the scour patterns reported in Section 4.2.1, the results of the velocity fields obtained by means of PTV technique are reported in Section 4.3. The analysis of the velocity fields in horizontal and vertical planes allows to evaluate the vorticity around the cylinder.

4.1 Rigid bed model

In this section the results and the main findings obtained from the experimental rigid bed campaign described in Section 3.2 are reported. In Section 4.1.1 the velocity measurements made by means of the ADV are compared with theoretical values obtained from linear theory and from *Fourier* decomposition. In Section 4.1.2 those

two approaches are used to study the total force over the pile and, finally, in Section 4.1.3 the pressure distribution around the pile at different wave phases is analysed as well as the pressure gradients which are the main responsible for vortex formation. Note that the results of the PTV campaign are reported in Section 4.3 after the results of the mobile bed tests, even if they were performed during the rigid bed experiments, in order to correlate them with the scour patterns. As above reported, it is well known that the mobile bed condition induces different nearbed dynamics, however a qualitative comparison of the seabed morphology and the vortices can help the understanding of the complex physical process of the wave-structure interaction.

4.1.1 Velocity

The characterization of the forces and the application of Equation 2.6 (Morison et al., 1950), begins with a deep comprehension of the behaviour of water particles under nonlinear waves. Le Méhauté (1976) stated that horizontal particle velocity under waves that present an high nonlinearity in terms of free surface shape, can be well predicted by the linear theory. As explained in Section 3.2, different ADV measurements were carried out for each wave condition at different depth from the bottom ($z_b = h + z$), with the instrument placed in correspondence of the free surface gauge $WG4$ in order to measure the associated water level. In the following analysis the so-called phase average of the data (velocity, force and pressure) is used, in order to obtain values that express correctly the statistics at the wave phases of interest (ωt). The phase average consists in fixing the phase (ωt) and averaging arithmetically all the "waves" of each test. The reference wave phases ωt are defined according to the water level evolution η measured at elevation gauge $WG4$, by assuming that $\omega t = 0°$ corresponds to the up-crossing of the water level signal.
In this thesis, nonlinear effects are taken into account by the application of the spectral decomposition to the measured water level time series for the computation of the kinematics of the wave. The detailed description of the method is remanded to Section 5.1 as it is the core of the new wave generation boundary condition (BC) implemented in the OpenFOAM® numerical model. In shorts, a *Fourier* analysis is performed in which the free surface elevation time series is decomposed by means of the *fft* technique. The time series of regular waves is treated as an irregular wave and, thus, the vertical distribution of the horizontal velocity its computed summing the contribution of each spectral component by the application of the linear wave theory. Therefore, in the new BC of the numerical model the input is represented by the spectral components (frequency, amplitude, phase) and, therefore, the water level time series at the inlet wave generation boundary is re-computed and it perfectly corresponds to the original one.

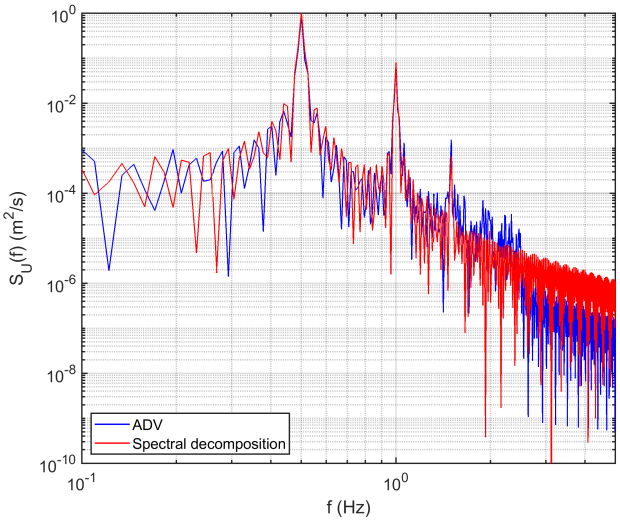

Figure 4.1: Comparison between velocity spectrum directly measured from ADV and computed by water elevation spectral components for wave test $R23$ at z_b=15cm.

To understand the efficiency of this approach, the power spectrum of the horizontal velocity ($S_u(f)$) is computed. The *fft* to compute the spectrum is directly applied to the measured time series of the velocity data in which a low-pass filter was applied in order to remove noise and outliers from the signal. Note that the choice of the best filter to smooth the signal could be a hard task especially if the aim of the analysis is the turbulence measurements for which the identification of noise from turbulence is not easy. The spectrum of the velocity, calculated from the water level time series with the methodology presented here and explained in details in Section 5.1, is compared with the one obtained directly from experimental data. In Figure 4.1 the comparison for the severe wave condition of test $R23$ is reported at the depth from the bottom of z_b=15cm. This graph is chosen as representative for all the analysed depths and waves which give quasi-identical results. The main frequency of this wave condition (T=2.0s) is f_1=0.5Hz and the main higher harmonics are visible (f_2=1.0Hz and f_3=1.5Hz). The three main frequencies are perfectly reproduced by the application of the *Fourier* decomposition method and even the corresponding values of spectral density are well represented. Moreover, the energy decay at higher frequencies occurs with the same velocity; the method seems to represent very well the characteristics of the wave not only considering their first component (that corresponds to that of the linear *Airy* approach) but taking into account the higher harmonics that give a non-negligible contribution to the particle velocity.
In Figure 4.2, the results of the analysis of the velocity for waves with different periods are displayed; in each subplot both the profile under crest phase and trough phases are shown. One wave condition for each period is reported (Figure 4.2a: R7 for T=1.83s, Figure 4.2b: R23 for T=2.00s, Figure 4.2c: R10 for T=2.19s, Figure 4.2d: R25 for T=2.35s; Figure 4.2e: R15 for T=2.74s).

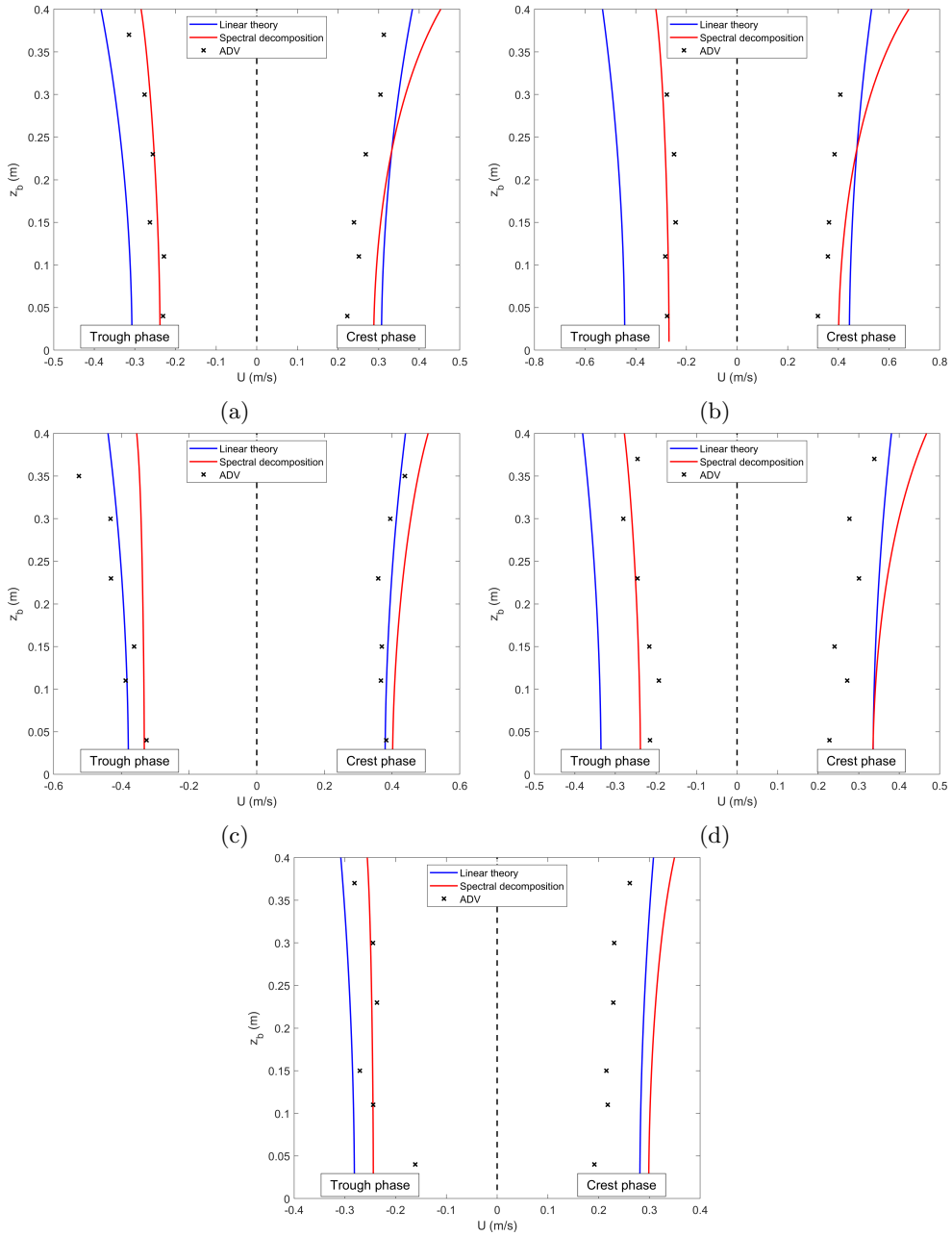

Figure 4.2: Horizontal water particle velocity under the trough and the crest of the wave for test R7 (a) with T=1.83s, R23 (b) with T=2.00s, R10 (c) with T=2.19s, R25 (d) with T=2.35s, R15 (e) with T=2.74s; experimental values and computed according to linear theory and spectral decomposition.

As already argued, even if wave surface is highly nonlinear (Figure 3.10), the linear theory gives a good estimation of the particle velocity even if it tends to overestimate the absolute value both during the trough and the crest phases. On the opposite, the

application of the reconstruction of the velocity profile from the spectral components in comparison with the linear theory leads to similar results for the crest phase (with a slight overestimation of the values), but, due to higher order harmonics effects, it gives very good prediction of negative velocity values during the trough phase which are almost perfectly representing the experimental results. Moreover, the analysis of the phase in which the maximum velocity peak occurs, is of primary interest for a good representation of the behaviour of a wave with higher order harmonics effects. The phase in which the horizontal velocity U is maximum is analysed ($\phi(U_{max})$) by the computation of the percent error (PE) according to the following expression:

$$PE = \frac{|\phi(U_{max,c}) - \phi(U_{max,r})|}{\phi(U_{max,r})} \tag{4.1}$$

in which $\phi(U_{max,c})$ is the computed value in which the maximum velocity occurs by using both linear theory or spectral decomposition method, $\phi(U_{max,r})$ is the reference value directly measured with ADV.

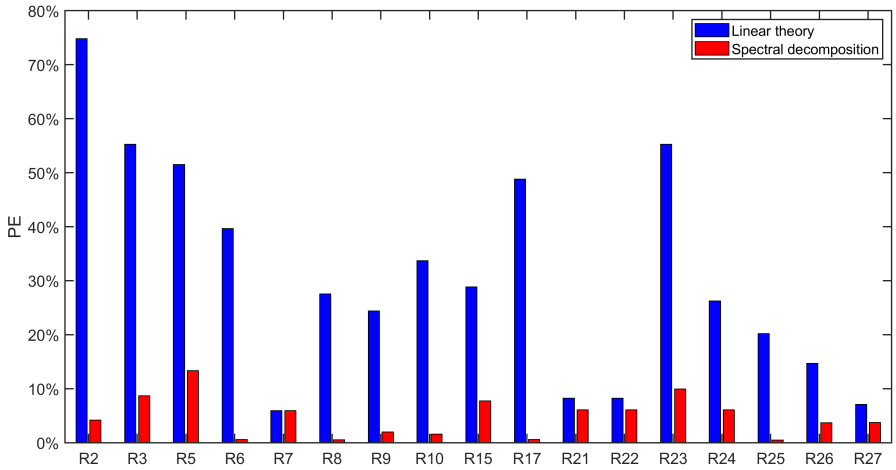

Figure 4.3: Values of the percent error (PE) of the phase in which the maximum velocity occurs for all the wave conditions of Table 3.1.

Figure 4.3 summarizes the results of this analysis. The mean value of PE for the phase shift with respect to the up-crossing with the application of the linear theory ($\phi(U_{max}) = 90°$) is of an order of 20-30% with a good representation of the waves that have small nonlinearities in their shape and in which the maximum value of water elevation, and thus of velocity, occurs for a wave phase of $\approx 90°$. On the contrary, the spectral decomposition method to reconstruct the local velocity lead to a very good estimation of the maximum velocity phase. In particular, the errors are always smaller than 15% with a mean value of PE of 5%.

4.1.2 Force over the pile

The main parameter of the design process of a marine structure is the total force acting on it. This series of experiments aim to find the method that better allows its estimate and to give the better reproduction during the entire wave period. What is usually done in the literature is to search a relation between some dimensionless

parameter (e.g. *Re*, *KC*) and the hydrodynamic coefficients C_D and C_M. In this thesis, in comparison with the main studies reported in the literature (see Section 2.3), the number of tests is rather limited and the small range of variability of KC do not allow to find a proper relation between the dimensionless parameters and the computed coefficients from experimental data that would result in a sparse cloud.
Therefore, here the approach of Morison et al. (1950), described in Section 2.3 with Equation 2.6, has been used for the evaluation of the total force acting over the pile using the literature coefficients in comparison with the experimental values where the force is obtained from the load cell on the top of the cylinder (Section 3.2). To reconstruct the kinematics of the wave (particle velocity and acceleration) both the linear theory and the *Fourier* decomposition method presented in Section 4.1.1 have been applied. A similar approach was used by other authors (Boccotti et al., 2012; Finnegan and Goggins, 2015) in random waves in which the velocity was computed from the spectral decomposition of the water elevation signal. They showed the validity of the method in terms of normalized frequency spectra of F with fitted coefficients (Boccotti et al., 2012) and in comparison with other numerical *Computational Fluid Dynamics* (*CFD*) models (Finnegan and Goggins, 2015). In this work, the same approach is used and, to consider nonlinear effects, the comparison is made in time-domain in which the information about the wave phases is preserved.
Considering the main works of previous authors (Figures 2.4 and Figure 2.5), it is reasonable to assume constant the hydrodynamic coefficients for the whole set of data due to the low variation in terms of KC (5-10) and Re (3-8·10^4). In particular, because of the higher range of Re of this study with respect to that of Chakrabarti (1980), the results of Sarpkaya (1976) are chosen as a reference from which the drag coefficient is set equal to $C_D = 0.9$ while the inertia coefficient is set equal to $C_M = 2.0$.
For all the wave tests of Table 3.1, the water surface and the total force are measured, the velocity profile is reconstructed from $\eta(t)$. The total force during the wave period is, hence, calculated with the hydrodynamic coefficients from the literature, both applying the linear theory (Equation 2.8 and Equation 2.9) and the *Fourier* approach. In the following figures (from Figure 4.4 to Figure 4.20), the results of the analysis are reported. In particular, in each figure the upper panel show the phase averaged measured free-surface elevation in comparison with the linear theory; the lower panel shows the measured force from the load cell over the wave period compared with the total force which is compared with the linear theory (red line) or with the spectral decomposition method (green line). Note that on the upper panel it is not plotted the result for the second method because, by its definition, the free surface reproduces perfectly the measured one.

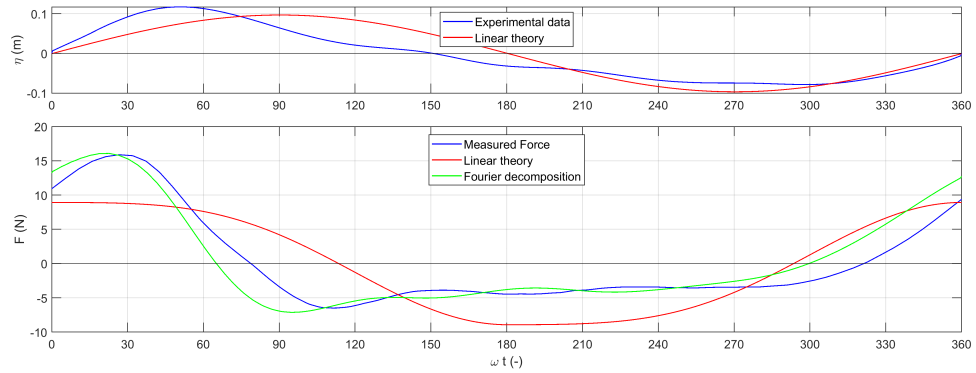

Figure 4.4: Phase averaged water level surface (upper panel) and force (lower panel): measured values and computed with linear theory or *Fourier* decomposition approach for wave test $R2$. Constant coefficients $C_D = 0.9$; $C_M = 2.0$

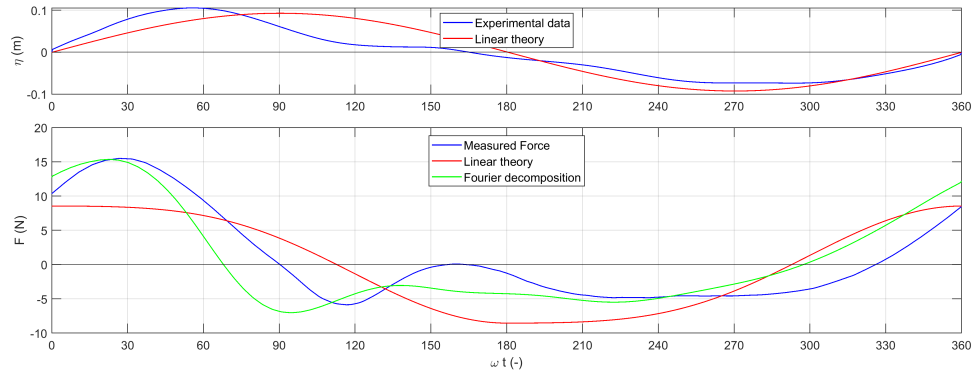

Figure 4.5: Phase averaged water level surface (upper panel) and force (lower panel): measured values and computed with linear theory or *Fourier* decomposition approach for wave test $R3$. Constant coefficients $C_D = 0.9$; $C_M = 2.0$

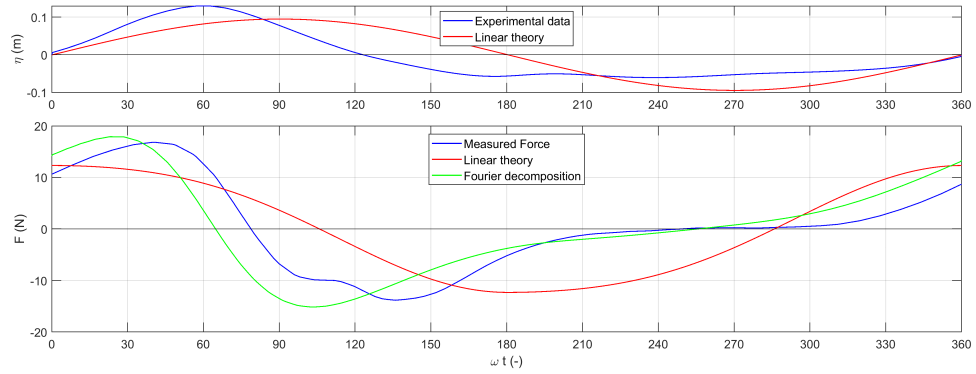

Figure 4.6: Phase averaged water level surface (upper panel) and force (lower panel): measured values and computed with linear theory or *Fourier* decomposition approach for wave test $R5$. Constant coefficients $C_D = 0.9$; $C_M = 2.0$

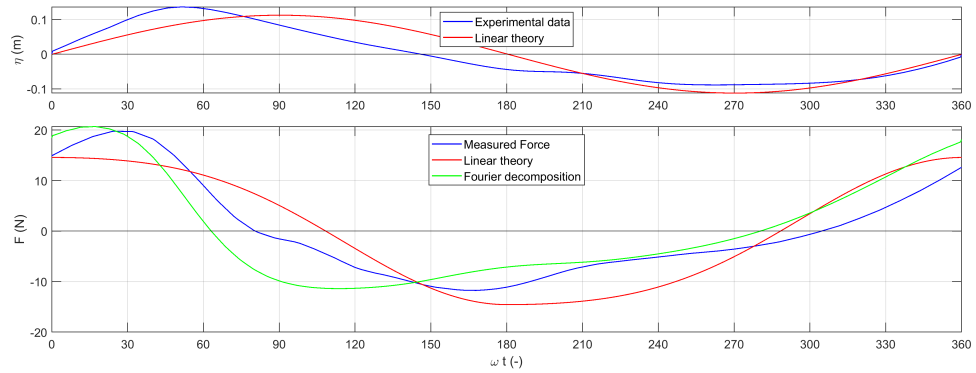

Figure 4.7: Phase averaged water level surface (upper panel) and force (lower panel): measured values and computed with linear theory or *Fourier* decomposition approach for wave test $R6$. Constant coefficients $C_D = 0.9$; $C_M = 2.0$

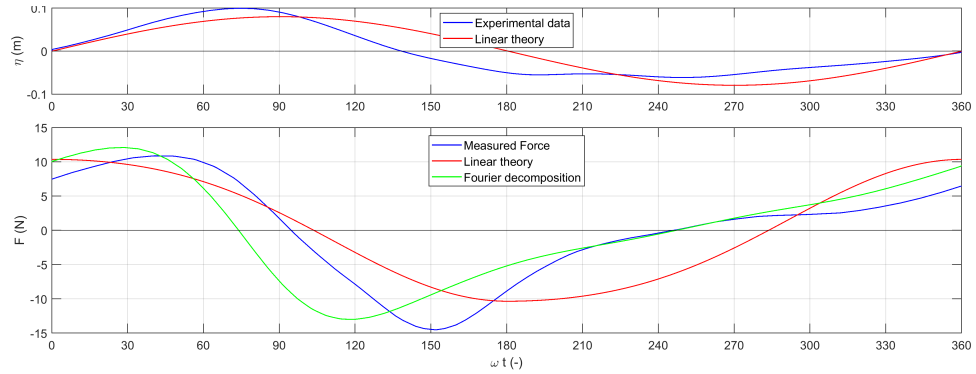

Figure 4.8: Phase averaged water level surface (upper panel) and force (lower panel): measured values and computed with linear theory or *Fourier* decomposition approach for wave test $R7$. Constant coefficients $C_D = 0.9$; $C_M = 2.0$

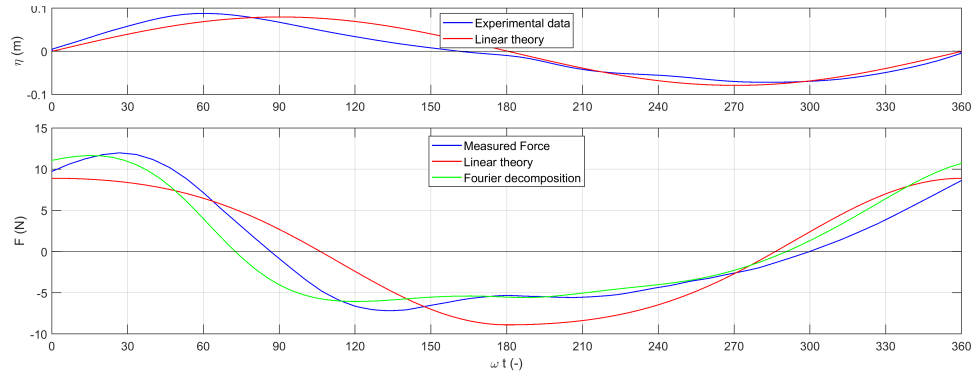

Figure 4.9: Phase averaged water level surface (upper panel) and force (lower panel): measured values and computed with linear theory or *Fourier* decomposition approach for wave test $R8$. Constant coefficients $C_D = 0.9$; $C_M = 2.0$

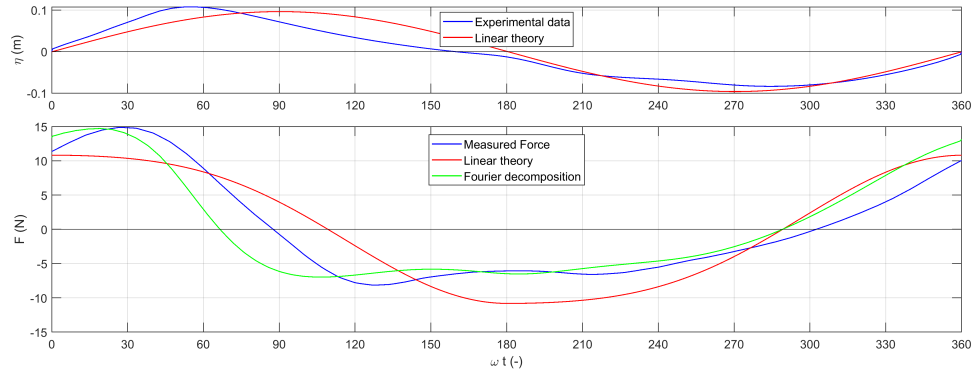

Figure 4.10: Phase averaged water level surface (upper panel) and force (lower panel): measured values and computed with linear theory or *Fourier* decomposition approach for wave test $R9$. Constant coefficients $C_D = 0.9$; $C_M = 2.0$

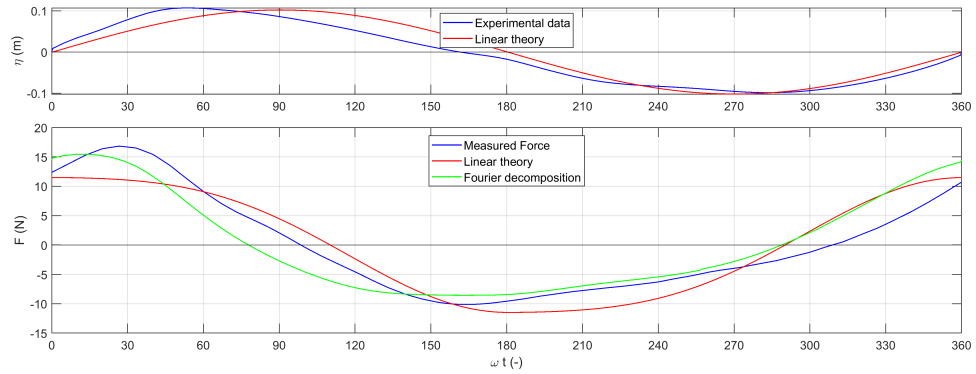

Figure 4.11: Phase averaged water level surface (upper panel) and force (lower panel): measured values and computed with linear theory or *Fourier* decomposition approach for wave test $R10$. Constant coefficients $C_D = 0.9$; $C_M = 2.0$

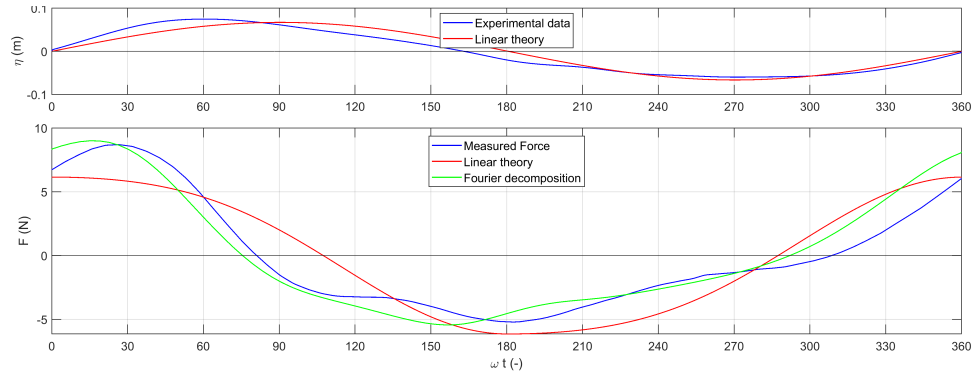

Figure 4.12: Phase averaged water level surface (upper panel) and force (lower panel): measured values and computed with linear theory or *Fourier* decomposition approach for wave test $R15$. Constant coefficients $C_D = 0.9$; $C_M = 2.0$

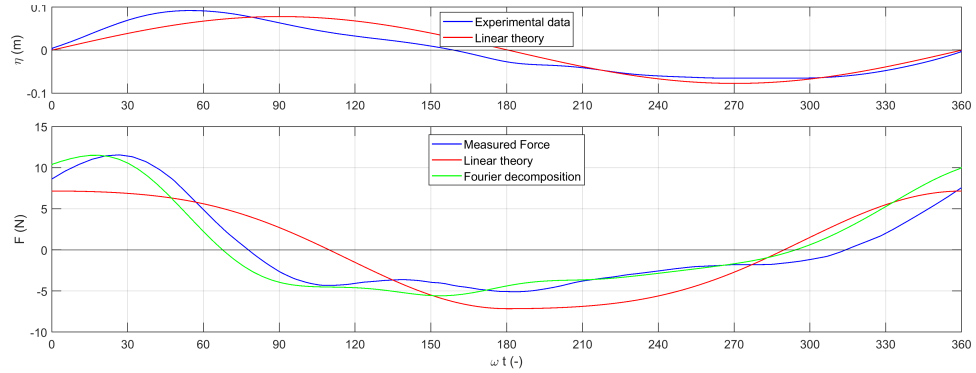

Figure 4.13: Phase averaged water level surface (upper panel) and force (lower panel): measured values and computed with linear theory or *Fourier* decomposition approach for wave test $R17$. Constant coefficients $C_D = 0.9$; $C_M = 2.0$

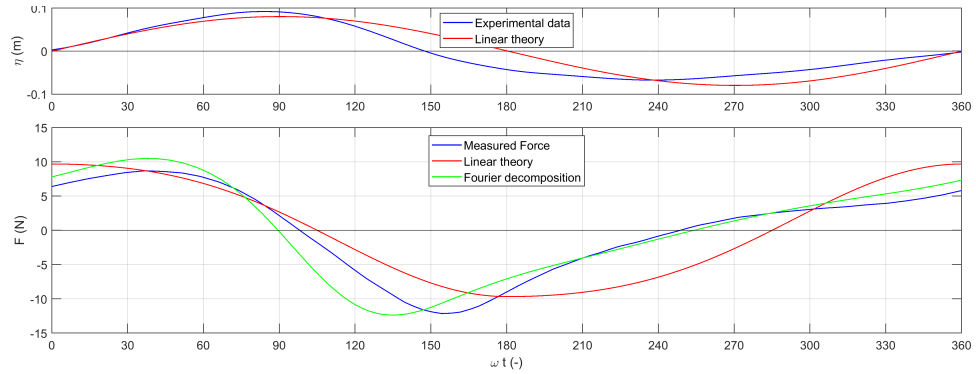

Figure 4.14: Phase averaged water level surface (upper panel) and force (lower panel): measured values and computed with linear theory or *Fourier* decomposition approach for wave test $R21$. Constant coefficients $C_D = 0.9$; $C_M = 2.0$

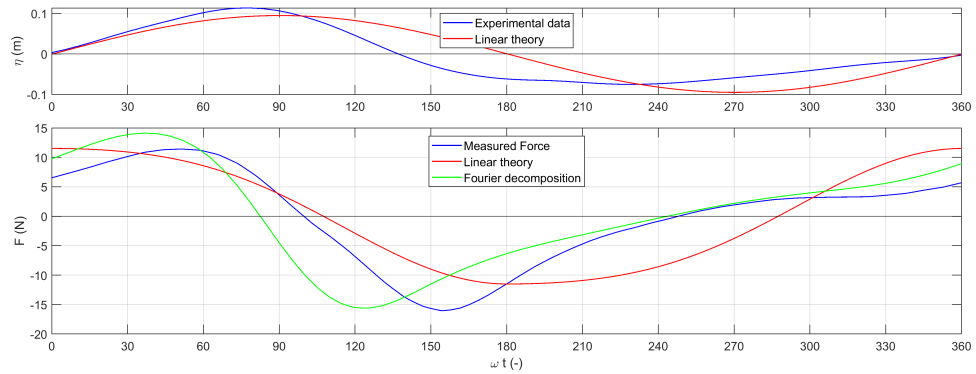

Figure 4.15: Phase averaged water level surface (upper panel) and force (lower panel): measured values and computed with linear theory or *Fourier* decomposition approach for wave test $R22$. Constant coefficients $C_D = 0.9$; $C_M = 2.0$

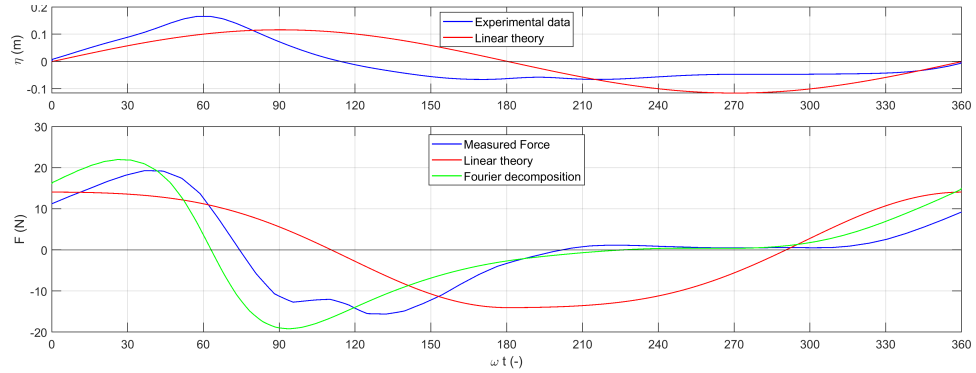

Figure 4.16: Phase averaged water level surface (upper panel) and force (lower panel): measured values and computed with linear theory or *Fourier* decomposition approach for wave test $R23$. Constant coefficients $C_D = 0.9$; $C_M = 2.0$

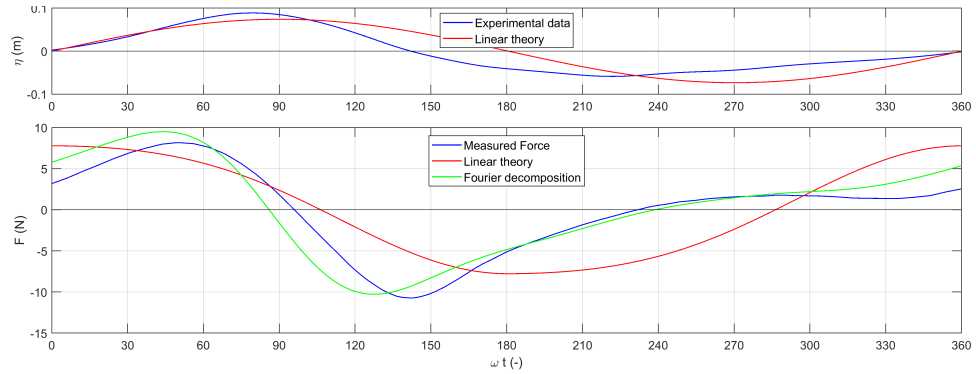

Figure 4.17: Phase averaged water level surface (upper panel) and force (lower panel): measured values and computed with linear theory or *Fourier* decomposition approach for wave test $R24$. Constant coefficients $C_D = 0.9$; $C_M = 2.0$

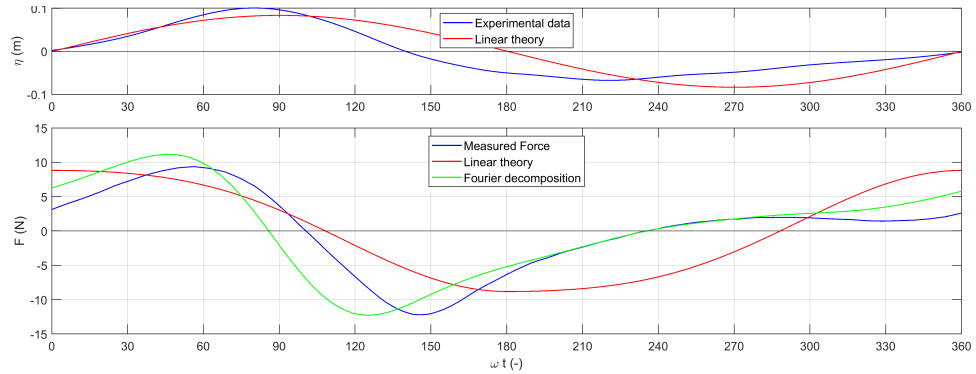

Figure 4.18: Phase averaged water level surface (upper panel) and force (lower panel): measured values and computed with linear theory or *Fourier* decomposition approach for wave test $R25$. Constant coefficients $C_D = 0.9$; $C_M = 2.0$

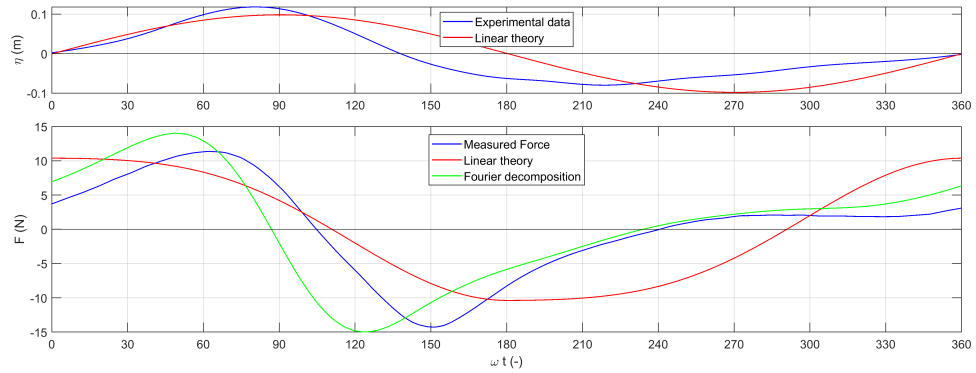

Figure 4.19: Phase averaged water level surface (upper panel) and force (lower panel): measured values and computed with linear theory or *Fourier* decomposition approach for wave test $R26$. Constant coefficients $C_D = 0.9$; $C_M = 2.0$

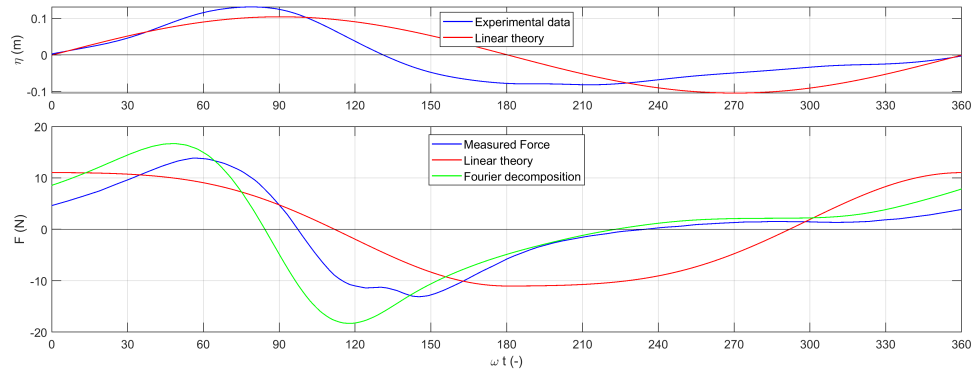

Figure 4.20: Phase averaged water level surface (upper panel) and force (lower panel): measured values and computed with linear theory or *Fourier* decomposition approach for wave test $R27$. Constant coefficients $C_D = 0.9$; $C_M = 2.0$

From the analysis of Figures 4.4-4.20 it is evident the advantage of using the *Fourier* spectral method to reconstruct the velocity field. Considering that the hydrodynamic coefficients are chosen as constant for all the tests and they are not fitted to better adapt on the experimental data, the evaluation of the total force only from the measurement of the water level gives very good results. The deviation from the results of the *Fourier* approach and the measured values between ωt of 60° to about 150° is due to the choice of the hydrodynamic coefficients. Indeed, if a best fit analysis is performed, a better agreement is obtained. As an example the result of the fitting for the wave condition $R27$ that showed a difference in the results in those phases (Figure 4.20) is reported. The best fit coefficients resulted to be $C_D = 1.2$ and $C_M = 1.2$ and the phase averaged force is shown in Figure 4.21.

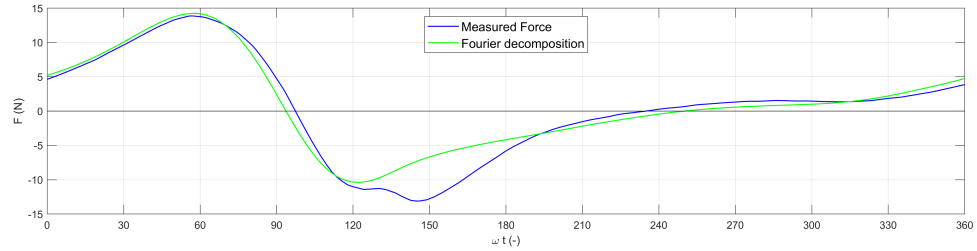

Figure 4.21: Phase averaged force: measured values and computed with *Fourier* decomposition approach for wave test $R27$. Fitted coefficients $C_D = 1.2$; $C_M = 1.2$

The deviation between the two curves is reduced significantly, especially for the positive elevation phases. However, as already said, the limited number of tests and of the KC range do not allow the investigation of a relation between the hydrodynamic coefficients and dimensionless parameters. The aim of this analysis is to study the efficiency of the *Fourier* method for the evaluation of the velocity, and thus force, under nonlinear waves by using validated relations for the evaluations of the coefficients. Even if a small drift with respect to the wave phase in which the maximum force occurs is observed, in the majority of the tests the maximum total force is estimated almost perfectly (tests $R2$, $R3$, $R5$, $R6$, $R7$, $R8$, $R9$, $R15$, $R17$) and in the others it slightly over predict the peak value. The only exception is represented by test $R10$ where the measured force is slightly higher than the computed one. Moreover, even the shape of the force, neglecting the phase shift between the curves, is very well reproduced; it means that the computation of velocities and accelerations made by following this approach is very valuable. On the other side, the application of the linear theory for the determination of the particle velocity does not lead to a good result on the total force estimation. In most of the cases the peak value is underestimated and, moreover, the trend of the force during the wave period is completely different. The visual representation of these results is found in Figures 4.22 - 4.23.

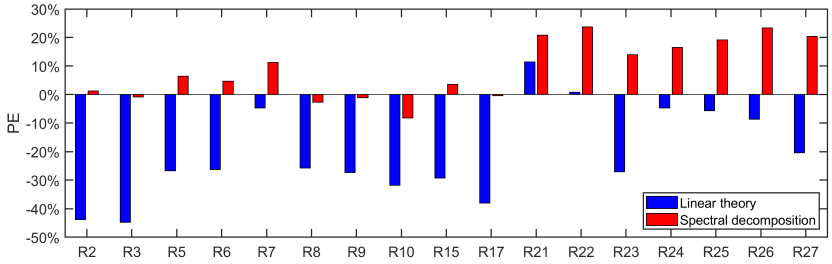

Figure 4.22: Values of the percent error (PE) of the maximum force for all the wave conditions of Table 3.1. Comparison between linear theory and spectral decomposition method.

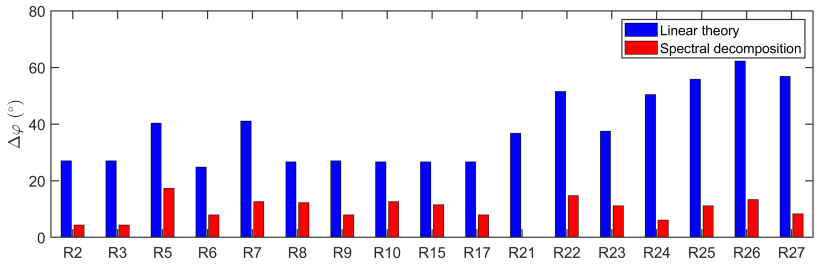

Figure 4.23: Values of the percent error (PE) of the phase in which the maximum force occurs for all the wave conditions of Table 3.1. Comparison between linear theory and spectral decomposition method.

With Figure 4.22 it is possible to understand which approach produces an underestimation ($PE < 0$), an overestimation ($PE > 0$) or a good estimation ($PE \approx 0$) of the total force over the pile. The PE value, described in Equation 4.1, is computed with the maximum values of measured force and computed force (with both linear theory and spectral decomposition approach). In Figure 4.23, the difference between the phases in which the maximum values of force occurred is reported ($\Delta\varphi = \varphi(F_{max,exp}) - \varphi(F_{max,th})$). The difference between the two methods is significant. The spectral decomposition model works very well on the estimation of the maximum force as already shown by Boccotti et al. (2012). Here, it is shown that also the phase shift among the peak values is very small (about 10°). The peak values are very well estimated in the majority the tests and in the others it slightly overestimates the value by 20% that could be a good compromise for design purposes because it results in a conservative but accurate approach to limit costs and guaranteeing the reliability of the structure. It must be noted that also the recommended practice Det Norske Veritas (2010) states that, if available, computation of the total particle velocities and accelerations based on more exact theories have to be preferred. The results obtained within this thesis show the suitability of this method for this purpose.
On the contrary, as already noted, the linear theory generally underestimates the peak values up to -40% and it must be noted that for the kinematic conditions of all the tests (see Figure 3.4) the inertia component is prevalent and, thus, the application of the linear theory with that specific values of C_D and C_M yields to a quasi negligible contribution of the drag on the total force. Therefore, the phase in which the maximum force is obtained corresponds to the phase in which the inertia force is maximum (up-crossing - $\varphi = 0°$) as it can be noted in Figures 4.4 - 4.20.

4.1.3 Pressure distribution around the pile

In the present section the analysis of the vertical pressure distribution and of the pressure gradients are reported. As already described, the cylinder is equipped with a hinge at its toe that enables rotations around its axis. Pressure gradients around the pile are studied with a discretization of reference vertical line of the pressure sensors of $\Delta\varphi = 30°$. The experimental pressure distribution around the pile is compared with the hydrostatic pressure profile calculated from the water depth. In Figure 4.24 the comparison of the vertical distribution of the total pressure measured in front of the pile ($\varphi = 0°$) and behind it ($\varphi = 180°$) is reported for an intense wave condition (wave $R2$).

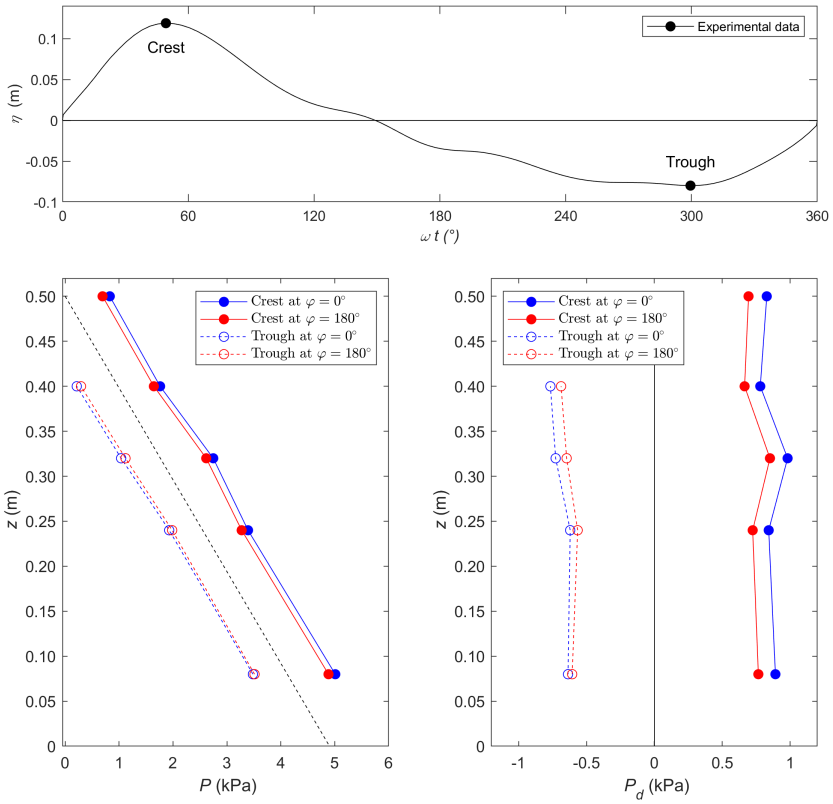

Figure 4.24: Vertical distributions of the total pressure P (left panel) and of the dynamic pressure P_d (right panel) for wave $R2$ at the crest (blue lines for $\omega t = 49°$) and at the trough (red lines at $\omega t = 300°$) phases. Results are plotted in two different positions: in front of the pile at $\varphi = 0°$ (solid lines) and behind it at $\varphi = 180°$ (dashed lines).

The phase averaged analysis of the water elevation η reveals that the wave crest occurs at wave phase $\omega t = 49°$ while the down-crossing occurs at a smaller wave phase for the experimental model ($\approx 150°$) with respect to the linear theory. The right panel of Figure 4.24 show the vertical distributions of the dynamic pressure P_d evaluated in front of the pile (blue lines for $\varphi = 0°$) and behind it (red lines for $\varphi = 180°$) for the crest (solid lines) and trough (dashed lines) wave phases. The analysis of the dynamic pressure distribution around the pile is very important because its asymmetry with respect to the vertical plane (yz-plane) produces a net horizontal force on the cylinder acting along the *x-axis*. During the growth of the positive water surface elevation (e.g. $\omega t = 49°$), a larger dynamic pressure P_d is observed in front of the pile with respect to the area behind it, hence, a positive horizontal force is expected, while during the negative water surface elevation (e.g. $\omega t = 300°$) the difference in pressure distributions at the two sides of the cylinder is smaller with a higher value on the wake of the pile, hence, for such wave phase the horizontal force along the *x-axis* is expected to be very small (in absolute value) and negative. Moreover, the dynamic

pressure data on the lateral sides of the cylinder at $\varphi = 90°$ and $\varphi = 270°$, here not shown, are similar, confirming that the horizontal force along the transversal direction y is expected to be negligible.
The measurements of the dynamic pressure around the pile also enable to confirm the presence, for specific wave phases, of positive pressure variations along the pile surface which induce the separation of the flow within the boundary layer which is the main condition for the subsequent generation of vortices.
In Figure 4.25 the plan view (xy-plane) of the dynamic pressure distribution around the pile is shown for the pressure sensor at the lower depth z_b=0.08m.

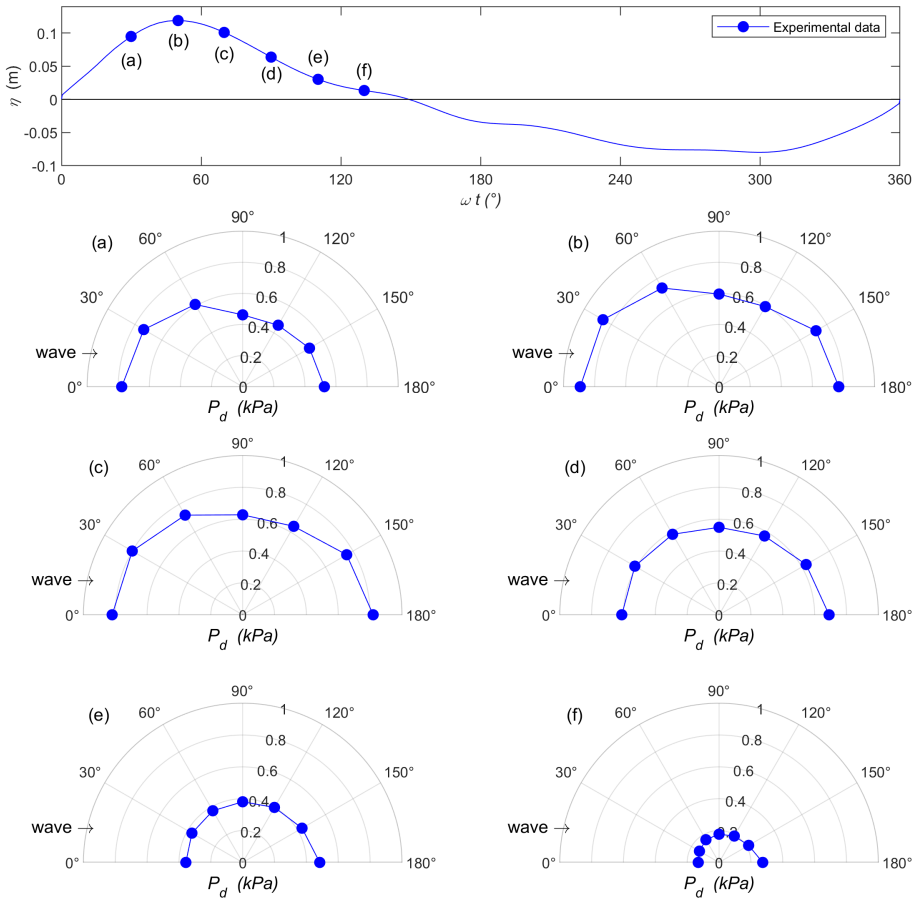

Figure 4.25: Phase averaged water elevation of wave $R2$ and plan view (xy-plane at z_b=0.08m) of the dynamic pressure P_d, for different wave phases: $\omega t = 30°$ (a); $\omega t = 50°$ (b); $\omega t = 70°$ (c); $\omega t = 90°$ (d); $\omega t = 110°$ (e); $\omega t = 130°$ (f).

It must be noted that the results for the sensor at z_b=0.50m under the trough phase are not plotted because the water level is lower than this position and, moreover, no results for the transducer at z_b=0.16m are present because of a water infiltration inside the sensor that compromised its reliability. The dynamic pressure distribution is reported for specific wave phases associated to the positive water surface elevation, in order to emphasize the pressure variations and, hence, to support the subsequent

analysis of the physical process. The first phase (panel "a" at $\omega t = 30°$) represents the rising of the wave, phases $\omega t = 50 - 70°$ (b-c) are representative for the crest condition, two other wave phases ($\omega t = 90°$ and $\omega t = 110°$) represent the decaying of the positive water surface elevation (d-e) and finally panel "e" at $\omega t = 130°$ is close to the down-crossing.
The pressure distribution shows an asymmetric shape with respect to the y-axis which changes with the wave phases. In addition, from Figure 4.25 it is possible to compute the pressure gradients along the surface of the cylinder ($\partial P/\partial x'$) for each wave phase (Figure 4.26).

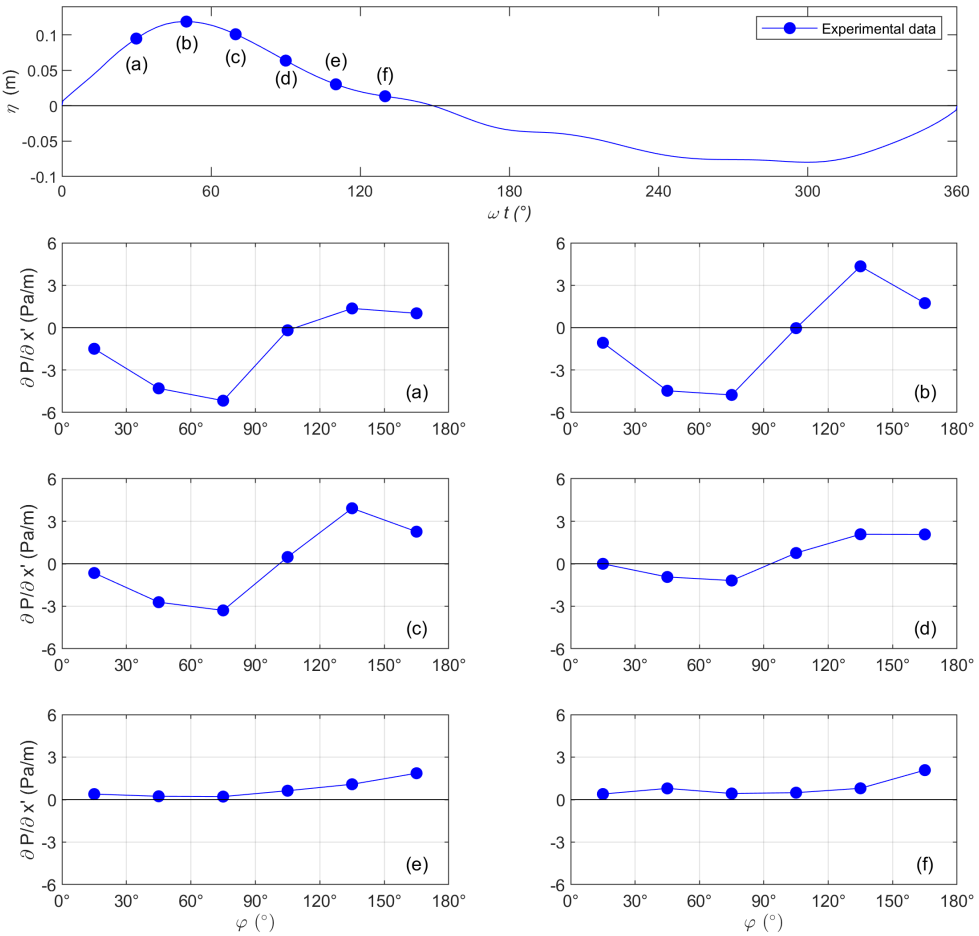

Figure 4.26: Phase averaged water elevation of wave $R2$ and pressure gradients ($\partial P/\partial x'$) along the surface of the cylinder at z_b=0.08m for different wave phases: $\omega t = 30°$ (a); $\omega t = 50°$ (b); $\omega t = 70°$ (c); $\omega t = 90°$ (d); $\omega t = 110°$ (e); $\omega t = 130°$ (f).

The coordinate x', used in this computation, is the curvilinear coordinate reported in Figure 3.9. Being $\Delta\varphi$ the angle between two pressure sensors, the curvilinear distance in between them is calculated as $\Delta x' = \pi D(\Delta\varphi/360°)$ and the pressure gradient is computed as $\partial P/\partial x' \approx (P(\varphi + \Delta\varphi) - P(\varphi))/\Delta x'$. When the flow is directed in the positive x direction, a positive pressure gradient is adverse to the flow and it can lead to a separation of the flow within the boundary layer that may origin

the detachment of the vortices. On the contrary, during the reverse flow (after the down-crossing) this condition of adverse gradient is represented by a negative value of $\partial P/\partial x'$. During the rising of the positive water surface elevation (panel "a"), a favourable pressure gradient (negative value) is observed around the pile, the pressure always decreases in the zone $\varphi = 0 - 105°$. Such condition is needed for the transport of the horseshoe vortices generated in front of the pile, as found during the mobile bed experiments (Corvaro et al., 2018b; Miozzi et al., 2019). During the crest phases (panels "b"-"c"), the pressure gradient is positive (adverse to the stream) at the back of the pile ($\varphi = 105° - 180°$) and its intensity and area of influence increase. A positive pressure gradient (for the first half cycle) in this area could lead to the separation of the flow within the boundary layer and, hence, to the formation of lee-wake vortices, which are the main responsible of the scour under wave action. When the flow approach to its reversal, the intensity of the dynamic pressure field diminishes due to the lower horizontal velocities that approach to zero at the down-crossing (panel "f"). Moreover, the distribution along the pile becomes symmetric with the decrease of the velocity (Figure 4.25 e-f). The intensity of the flow is not high enough to lead to the formation of vortices at these phases and, thus, the pressure gradient which is obtained is almost zero (Figure 4.26 e-f). As it will be discussed later, such findings are in agreement with the results of the vortex pattern reported in Sections 4.3 and 5.4.2 in which the formation, development and transport of the coherent structures is analysed by means of both experimental measurements and a numerical model.

4.2 Mobile bed model

In this section are reported the results obtained from the experimental mobile bed campaign (Corvaro et al., 2018b) described in Section 3.3. In Section 4.2.1, the identification of the scour pattern classes and the evaluation of the maximum values for regular waves are reported. In Section 4.2.2, a method for the evaluation of the scour under random waves is proposed.

4.2.1 Scour under regular waves

For each test of the mobile bed experiments, the equilibrium seabed location was measured by means of the laser distance meter in dry condition.
As above stated, in the present experiment θ was always larger than θ_{cr}, hence the scour could be classified as "live bed" type. Values of $\theta > \theta_{cr}$ lead to energetic nearbed dynamics that implies a significant formation of vortex ripples (Foti and Blondeaux, 1995), which cannot be avoided. In particular, the shape of the scour can be classified into 10 different classes as noticed by Umeda (2011) depending on the values of KC and θ: (I-1) small scour, (I-2) side scour, (I-3) wake scour, (I-4) wake and semi-cone scour, (I-5) truncated-cone scour, (II-1) detached scour, (II-2) wake scour with rolling-grain ripples, (II-3) truncated-cone scour with rolling-grain ripples, (III-1) vortex ripples, and (III-2) truncated-cone scour with vortex ripples. Some typical scour regimes of our experiments are shown in Figure 4.27.

Figure 4.27: Typical ripple classes: wave R0 (I-3), wake scour; wave R16 (II-2), wake scour with rolling grain ripples; wave R14 (III-2), truncated-cone scour with vortex ripples.

The presence of ripples highly influenced the seabed morphology, as expected for live bed conditions. Figure 4.28 maps our results as function of the classes found by Umeda (2011). The identification of the bedform types was not simple: although tests R13 and R16 have been classified as "II-2", in the downward side of the mobile bed model the vortex ripple generation seemed to lead to a "III-2" regime. Furthermore, R0 (considered as wake scour "I-3") could also be interpreted as a side scour ("I-2") because of the non-negligible scour in that area. Considering all these uncertainties, a quite good agreement has been found between the morphologies observed for each (KC,θ) pair and the findings of Umeda (2011).
Large values of KC and θ led to a significant formation of seabed ripples, most of the tests showed a scouring pattern identified as "III-2": truncated-cone scour with vortex ripples regime. For such waves a very good agreement was found between the morphologies observed and the classification proposed by Umeda (2011): the data are all within the boundaries of III-2 class. A weaker agreement was obtained for the waves identified as "II-2" (the data were close to the boundaries of II-2 class), while only for two tests (R0 and R1), for which the scour shape could be identified as a wake scour, the data was spread.

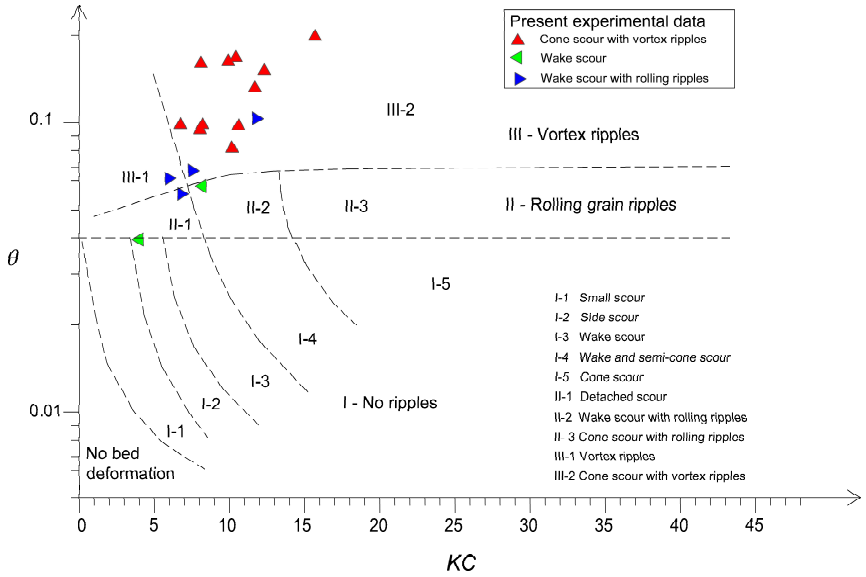

Figure 4.28: Scour regime classes proposed by Umeda (2011) and comparison with the present experimental data for regular waves.

Umeda (2011) used a different sand diameter in his experiments, hence, the value of θ_{cr} differs slightly (by applying Equation 3.10 θ_{cr}=0.04) from that of our experiments (θ_{cr}=0.03). This slight deviation can produce some changes in the boundaries of the scour classes. Table 4.1 summarizes the dimensionless values of the scour depth along the pile (S/D) and the maximum scour depth (S_{max}/D) around it.

Table 4.1: Scour depth for regular waves. S/D is the scour at the edges of the pile; S_{max}/D is the maximum scour around the cylinder.

Name	H (m)	T (s)	KC (-)	S/D (-)	S_{max}/D (-)	d/D	φ (°)
R0	0.12	1.83	4.0	0.00	0.15	1.08	124
R1	0.14	2.74	8.1	0.11	0.14	1.10	180
R2	0.21	2.74	11.7	0.15	0.20	1.00	180
R3	0.28	2.74	15.7	0.25	0.33	1.60	180
R4*	0.35	2.74	19.6	0.21	0.31	0.90	180
R5	0.20	1.83	6.7	0.01	0.13	1.10	180
R6	0.25	1.83	8.0	0.10	0.12	1.20	180
R7	0.16	1.83	5.2	0.02	0.18	1.66	123
R8	0.16	2.19	6.8	0.05	0.22	1.17	121
R9	0.19	2.19	8.1	0.12	0.19	1.50	180
R10	0.23	2.19	9.9	0.21	0.18	1.70	180
R11	0.14	2.19	6.1	0.10	0.18	1.25	119
R12*	0.36	2.74	20.2	0.21	0.27	1.30	180
R13	0.17	2.74	10.8	0.15	0.16	1.61	173
R14	0.19	2.74	12.3	0.13	0.23	1.70	180
R15	0.17	2.74	9.8	0.13	0.17	1.40	180
R16	0.14	2.19	6.7	0.10	0.20	1.63	133
R17	0.19	2.74	10.6	0.10	0.18	1.30	180
R18	0.16	2.19	8.0	0.10	0.11	1.40	176
R19	0.21	2.19	10.4	0.10	0.14	1.19	180

Note: * Breaking wave.

The scour depth S was evaluated as the maximum values measured at the edges of the pile at five points: (φ=0°, φ=45°, φ=90°, φ=135°, φ=180°). In this section also the values of the maximum scour depth S_{max} measured around the cylinder and not at its edges are reported, because, for the majority of the tests, it was larger than S.
In Table 4.1 the dimensionless distance (d/D) with respect to the centre of the pile and the angle φ where the maximum scour is located (d/D=0.5 means that the maximum scour occurs at the edge of the pile; for φ=180°, the coordinate d corresponds to x) are also reported.
The steady-state of the seabed morphology and the scour depth in the area around the cylinder are shown in Figure 4.29 (a symmetric scour is observed with respect to y-axis) in which the darkest blue parts correspond to the scour zone, while the red ones to the deposition areas. As expected, waves characterized by larger values of KC led to a larger erosion close to the cylinder, especially in the downstream area.
As long as KC increased, also the scour depth increased, as shown in Figure 4.30. The general expression of Equation 2.3 obtained by Sumer et al. (1992) is:

$$\frac{S}{D} = 1.3(1 - \exp[-m(KC - 6)]), \tag{4.2}$$

in which m=0.03 for linear waves.

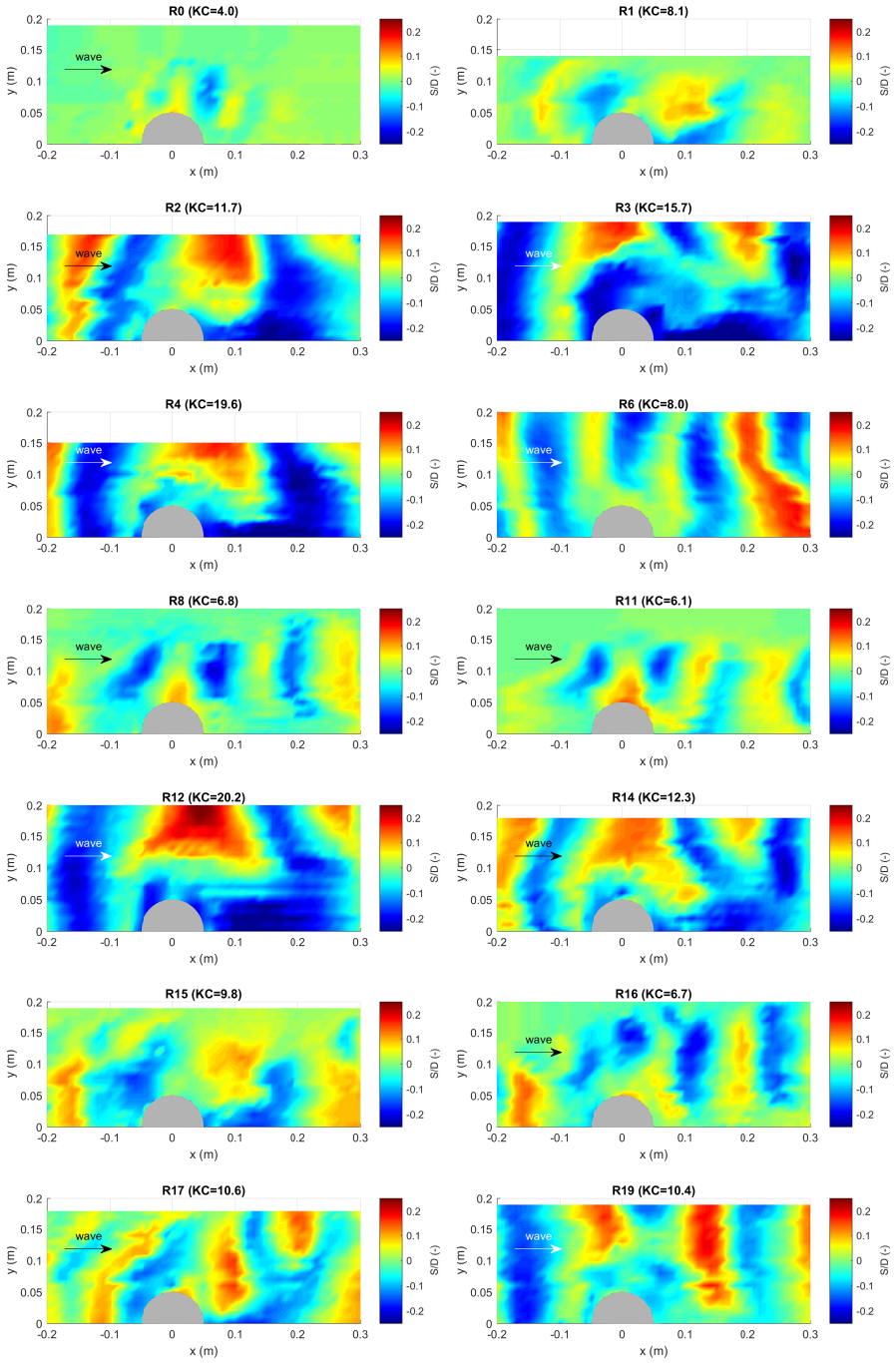

Figure 4.29: Seabed morphology under regular waves.

The experimental data of the present work are plotted together with those of the experiments of Sumer et al. (1992) in Figure 4.30. The comparison shows a good agreement between the two sets of experiments and, hence, the experimental data are well predicted by Equation 4.2.

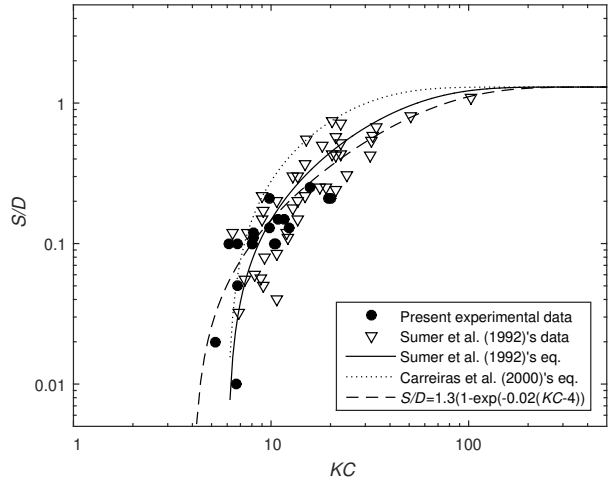

Figure 4.30: Comparison between the experimental data of the mobile bed campaign and those of Sumer et al. (1992). The continuous line is the Sumer et al. (1992)'s equation (see Eq. 4.2 with m=0.03, r^2=0.77), the dotted line is the Carreiras et al. (2000)'s equation (see Eq. 4.2 with m=0.06, $r^2 \approx 0$), while the dashed line is the proposed best-fit equation (r^2=0.81).

For nonlinear waves Carreiras et al. (2000) found that a better fitting was obtained by using a larger value of m (0.06 instead of 0.03) in Equation 4.2 and by evaluating KC as a function of the horizontal excursion according to Equation 2.2, instead of the horizontal velocity at the bed U_m. Even if the scour depth formula proposed by Carreiras et al. (2000) is obtained for nonlinear waves, Figure 4.30 shows a weaker adaption with the present experimental results ($r^2 \approx 0$), characterized by nonlinear waves. It was found that a smaller coefficient m (even smaller than 0.03) fitted the experimental data better, in disagreement with the findings of Carreiras et al. (2000). A possible explanation could be related to the water depth conditions: the experiments of Carreiras et al. (2000) were conducted mainly in shallow water conditions and over a sloping beach, while the present experiments used intermediate water conditions on an horizontal seabed. It is hence reasonable to suppose that the type and the degree of nonlinearity of the experiments of Carreiras et al. (2000) is higher with respect to the present thesis.
Therefore, a modified equation for the scour depth has been found, by considering the present experimental data and those of Sumer et al. (1992)). A new best-fit law has been obtained, keeping the same upper limit value ($S/D = 1.3$ for $KC \to \infty$) that corresponds to the steady current state condition and considering that the occurrence of scouring was observed for $KC < 6$, in particular the starting condition for the scour

process took place for $KC \approx 4$, thus, Equation 4.2 can be rearranged as:

$$\frac{S}{D} = 1.3(1 - \exp[-0.02(KC - 4)]) \tag{4.3}$$

which gives a value of $r^2 = 0.81$, as shown in Figure 4.30.
For design purposes, this update of Equation 4.2 considering new data, would result the most conservative for $KC \leq 7$, while the approach of Carreiras et al. (2000) is the most conservative for $KC > 7$. Inspection of the seabed morphology around the pile reveals the occurrence of seabed ripples, which could interfere with the expected results. In the literature the effects due to ripples are often regarded as negligible because the large increase of the velocities adjacent to the pile destroy such bedforms. However, in the present study, in which the waves are the only forcing, we found that the ripples were completely destroyed only very close to the cylinder and not in the surroundings of it, hence they do not influence only the evaluation of S, while they influence S_{max}. Different seabed morphologies around the pile can be observed for waves characterized by similar values of KC (i.e. waves R1 with KC=8.1 and R6 with KC=8.0). Such values can be obtained by different combinations of H and T (i.e. wave R1: H=0.14m, T=2.74s; wave R6: H=0.25m, T=1.83s). However, we believe that such behaviour is mainly due to the influence of both wave height and wavelength on the smaller-scale bedforms (ripple length and ripple height). This is also confirmed by their scour regime classes (R1 wake scour; R6 vortex ripples) as shown in Figure 4.28. From the results of these experiments, we observed that the wavelength influences the scour depth through KC (i.e. implicitly), while its explicit influence on the local bedforms does not impact upon the size of the scour. Therefore, even if the value of the maximum scour S_{max} might be affected by the ripples, the position where the maximum erosion occurs could be well identified (see Figure 4.29). This was located, as reported in Table 4.1, at a distance of about $d = 1D$ behind the pile. The increase of KC influenced the position where the maximum scour depth was observed. As shown in Figure 4.29, for KC <7 (R0, R7, R8, R11 and R16) the area where the deepest scour occurred was located at $\varphi \approx 100 - 130°$. If the energy of the waves increased (and, therefore, KC), the maximum scour depth area moved downstream reaching $\varphi = 180°$ ($KC > 8$). Sumer et al. (1992) found that for KC >6 a vortex street at the lee side of the pile is formed and its extent increased linearly with KC. In agreement with the findings of Sumer et al. (1992), it is observed that, as KC increased, the intensity of the lee-wake vortices became larger, vortex shedding occurred, meaning that the area exposed to such action and, hence, to scouring, became larger. This phenomenon occurred because the lee-wake vortices were not attached to the pile and, rather, they were shed from it. The favourable pressure gradient allowed the transport of the detached vortex in the area behind the pile, where the maximum scour was observed. The large orbital velocity under the wave crest induced a downstream movement of the separation point, therefore the maximum scour was located in the wake of the pile. Such a result revealed an asymmetric effect on the scour depth due to a lower energy of the reversed flow (negative internal wave velocities). This behaviour was more evident for nonlinear waves in which the wave crest was larger than the wave trough and, hence, the vortices, responsible of the scour processes, became even more energetic during the wave crest period.
The influence of breaking waves on the scour has been investigated in the literature, however the wave breaking process is influenced by the water depths. Bijiker and de Bruyn (1988) found that in shallow waters combined currents and breaking waves increase the scour with respect to the currents/non-breaking waves combination;

Nielsen et al. (2012) investigated on the scour produced by waves breaking in shallow waters, finding that for large piles the scour due to breaking waves can be an order of magnitude larger than those due to non-breaking waves. In the present experiments (intermediate water depths) a weaker effect on the seabed has been observed due to breaking waves (waves R4 and R12). In such water depths, the turbulence due to the breaking waves and reaching the seabed is not energetic enough, as observed by Corvaro et al. (2010) in the wave damping process, to induce a significant sediment motion, as expected for such large values of KC.

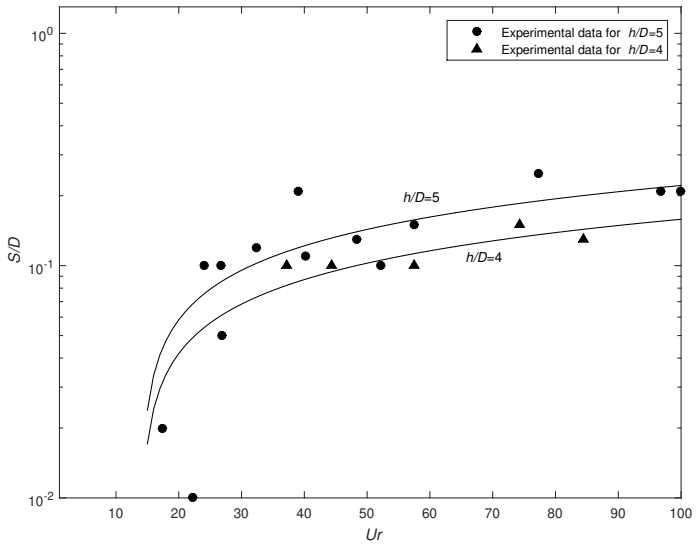

Figure 4.31: Influence of the Ursell number on the dimensionless scour depth.

Finally, in order to introduce the influence of the nonlinearity in the formula for the prediction of the scour depth, the influence of Ur on the scour depth has been investigated, as shown in Figure 4.31, by also considering the ratio between the water depth and the pile diameter h/D. The *Ursell* number indicates the degree of nonlinearity of gravity waves. As expected, an increase of the scour depth S/D with the Ur (its square root in particular) has been found: S/D=$0.002(h/D)^{1.5}(Ur\text{-}13)^{0.5}$ ($r^2 = 0.74$). Its validity is limited to the Ur range of the present data ($Ur \approx$10-100). Sumer et al. (1992) highlighted that the limiting value of scour depth under wave action is $S/D \longrightarrow 1.3$. In these experiments only a maximum value of $S/D = 0.25$ has been obtained, hence further studies are needed to extend the dataset to verify such dependence.

4.2.2 Scour under random waves

In order to evaluate the scour originated by a random sea state, nine different tests were performed. Three different peak periods were analysed ($T_{p,1} = 2.74$ s for the sea states from NR1 to NR4; $T_{p,2} = 1.83$s for NR5 and NR6; $T_{p,3} = 2.19$s from NR7 to NR9). For each peak period, different significant wave heights were used until breaking was reached by a large portion of the wave packet. In order to reproduce adequately all wave spectra, each test contained more than 500 waves. Therefore, the duration of each experiment (t_{max}) was different depending on the wave period T_p

($t_{max,1}$=24min; $t_{max,2}$=16min; $t_{max,3}$=20min).The steady-state measured morphology for each test is reported in Figure 4.32.

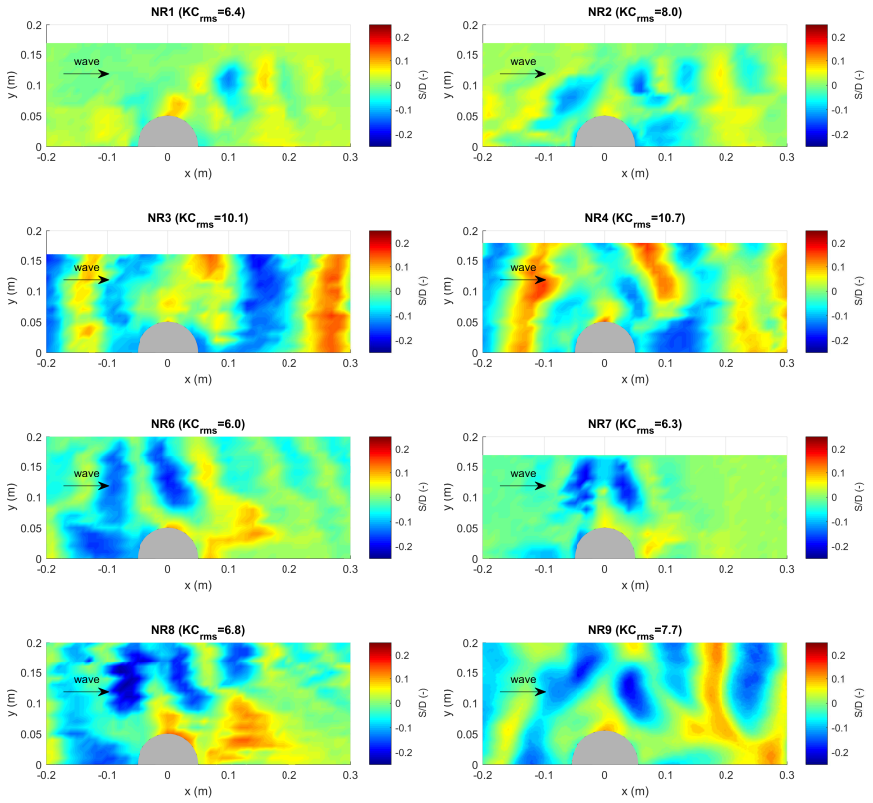

Figure 4.32: Seabed morphology under random waves.

In this case the formation of the ripples is less clear because of the nature of the irregular flow that moves the particles in both the directions with different intensity during the whole experiment. However, even in this more complex situation, it is possible to notice that when the overall wave energy was large (large KC) the maximum scour area moved downstream of the pile (see NR4 and NR1 in Figure 4.32). When KC increased, the flow was strong enough to generate vortices that, for $KC > 6$, were shed behind the cylinder.

Table 4.2: Scour depth for random waves. S/D is the scour at the edges of the pile; S_{max}/D is the maximum scour around the cylinder.

NAME	H_s (m)	T_p (s)	KC_{rms} (-)	S/D (-)	S_{max}/D (-)	d/D	φ (°)
NR1	0.120	2.69	6.39	0.05	0.13	1.49	132
NR2	0.160	2.60	7.99	0.10	0.15	1.08	124
NR3	0.192	2.77	10.14	0.13	0.17	0.50	180
NR4	0.212	2.69	10.74	0.12	0.19	1.20	180
NR5	0.160	1.91	5.68	0.10	0.14	1.32	99
NR6	0.184	1.82	5.95	0.11	0.17	1.12	100
NR7	0.144	2.24	6.26	0.12	0.18	1.17	110
NR8	0.168	2.15	6.83	0.10	0.17	1.24	104
NR9	0.198	2.11	7.68	0.05	0.18	1.21	114

However, unlike for regular waves, here the KC number alone cannot adequately describe the seabed patterns and scour depth values. For example, the wave condition $NR1$ is characterized by a quite high value of KC ($KC_{rms} = 6.39$), but the effect induced on the final scour map is smaller than for waves $NR5$ and $NR6$ probably due to the smaller significant wave height. Values of the dimensionless scour depth S/D and of the maximum scour S_{max} are summarized in Table 4.2. Even for random waves it was possible to evaluate the position of the maximum scour considering both the dimensionless distance d/D and the angle φ defined in Figure 3.9. As for regular waves, when the value of KC_{rms} increased, the maximum scour position was found for $\varphi \approx 180°$. The higher intensity and frequency of the flow pushed the vortices in the wake zone where they detached alternatively carrying away the sediment already put into suspension by the horseshoe vortex.
Due to the limited number of tests only an evaluation of the scour depth, according to Sumer and Fredsøe (2002), is done using Equation 4.2 with KC_{rms} computed as in Equation 3.6 instead of KC. Therefore, differently from the regular waves approach (Figure 4.30), here the data are not added to those of Sumer et al. (1992). Figure 4.33 shows a fair agreement between the experimental scour values and the formula: an underprediction is observed, in particular for random waves a significant scour has been found even for $KC_{rms} \approx 6$.

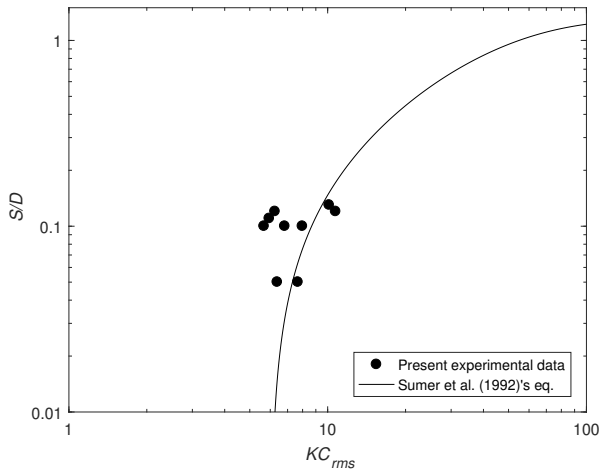

Figure 4.33: Comparison of experimental random wave scour with Sumer et al. (1992).

Ong et al. (2013) proposed a method of computation of the scour based on the assumption that just part of the waves (the highest portion) contributes to the process. Using this statistical methodology, a random sea state associated to $KC_{rms} < 6$ contains, in its wave packet, higher waves able to induce scouring.
In the experience of Ong et al. (2013), the water elevation spectrum was used as input for the computation through the water level time-series given by the Sharma and Dean (1981) method and by assuming the waves to be a stationary narrow-banded random process. In the present work the input time-series was measured at the free surface gauge located just upstream the pile and then the wave spectrum was computed. The advantage of this kind of computation is that the evaluation of the scour depth is based on measured data and not on a numerical solution. However, one limitation is the length of the test. To minimize this effect we decided to set the test length to guarantee that at least 500-600 waves were examined. As shown in Equation 2.1 it is possible to associate a KC_{rms} value to each sea state, composed by individual waves with crest elevation η_c. Defining the dimensionless, nonlinear crest elevation $w_c = \eta_c/A_{rms}$ it is possible to apply the Forristall (2000) crest height distribution taking the waves as long-crested. The cumulative distribution function (*cdf*) of the two-parameter *Weibull* distribution can be written as:

$$P(w_c) = 1 - \exp\left[-\left(\frac{w_c}{\sqrt{8}\alpha}\right)^{\beta}\right]; w_c \geq 0 \tag{4.4}$$

where α and β are the 2D Weibull parameters. Forristall (2000) expressed these values as function of the wave steepness (S_1) and Ursell parameter (Ur_1) defined in Equation 3.7:

$$\begin{aligned} \alpha &= 0.3536 + 0.2892S_1 + 0.1060Ur_1 \\ \beta &= 2 - 2.1597S_1 + 0.0968Ur_1^2. \end{aligned} \tag{4.5}$$

These formulations were obtained from 2D second-order wave theory simulations and compared with data measured during extreme events (hurricanes and storms). To represent the laboratory characteristics of every random wave test, the values of α and β were obtained fitting the experimental crest height distribution with the *cdf* of Weibull distribution given in Equation 4.4. It is reasonable to assume that laboratory characteristics are different from extreme field conditions. An example of the excellent agreement obtained is shown in Figure 4.34.

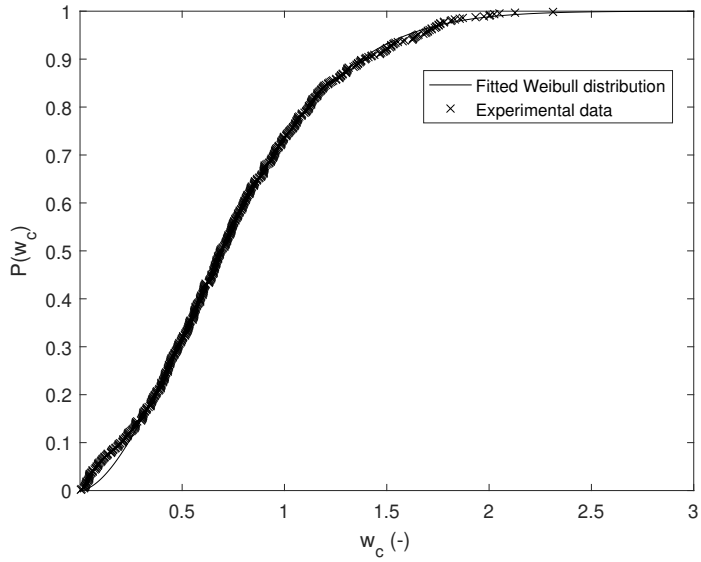

Figure 4.34: Comparison between the experimental data and the fitted Weibull cumulative distribution function for the test NR1.

The evaluation of these parameters according to this method allows to take into account the nonlinear effects induced by the ramp at the upstream end of the flume. Assuming a value of n as the reference value to identify the part of the highest waves that caused the maximum equilibrium scour, the individual waves of the sea state can be sorted in descending order of w_c. Two different threshold values can be evaluated:

$$w_{c1} = \frac{6}{KC_{rms}} \tag{4.6}$$

$$w_{c1/n} = \sqrt{8}\alpha \left[\ln n + \left(\frac{w_{c1}}{\sqrt{8}\alpha} \right)^{\beta} \right]^{1/\beta} \tag{4.7}$$

w_{c1} is the lower threshold value of w_c of the Weibull truncated distribution, meaning that the *cdf* expressed in Equation 4.4 becomes:

$$P(w_c) = \frac{\exp\left[-\left(\frac{w_{c1}}{\sqrt{8}\alpha} \right)^{\beta} \right] - \exp\left[-\left(\frac{w_c}{\sqrt{8}\alpha} \right)^{\beta} \right]}{\exp\left[-\left(\frac{w_{c1}}{\sqrt{8}\alpha} \right)^{\beta} \right]}; w_c \geq 0 \tag{4.8}$$

$w_{c1/n}$ is a limiting value that, among the waves higher than w_{c1}, identifies the waves that give a contribution to the scour process (e.g. if $n = 1$, $w_{c1/n} = w_{c1}$; if $n > 1$, $w_{c1/n} > w_{c1}$, hence the largest waves are retained for the computation). In more detail, the $(1/n)^{th}$ portion of the highest crests, among those exceeding the limiting value w_{c1}, are used in the computation.
The Heaviside-function $H(w_c - w_{c1/n})$, defined as 1 for $w_c > w_{c1/n}$ and 0 elsewhere, is introduced to avoid the contribution of the waves smaller than $w_{c1/n}$. Moreover, defining $p(w_c) = dP(w_c)/dw_c$ it is possible to compute the mean dimensionless scour

according to Ong et al. (2013).

$$\frac{S}{D} = 1.3n \int_0^\infty Y(w_c) p(w_c) H(w_c - w_{c1/n}) dw_c \tag{4.9}$$

where $Y(w_c) = 1 - \exp(-0.03(KC_{rms} w_c - 6))$.
Different values of n have been used to estimate which one fits best the experimental results (S). The values obtained are summarized in Table 4.3. To evaluate the scatter between the computed and the measured data, for each test and each value of n, the relative error has been defined as:

$$\delta_i = \frac{|S_n - S|}{S_n}. \tag{4.10}$$

Therefore, it was also possible to compute the average value and the corrected standard deviation as:

$$\begin{aligned} \bar{\delta}_n &= \frac{1}{N} \sum_{i=1}^{N} \delta_i \\ s_n &= \sqrt{\frac{1}{N-1} \sum_{i=1}^{N} (\delta_i - \bar{\delta}_n)^2} \end{aligned} \tag{4.11}$$

where $N = 9$ is the number of the samples for each n.
These values are shown in Figure 4.35, where the line on the graph represents the average value and the error bar is the standard deviation.

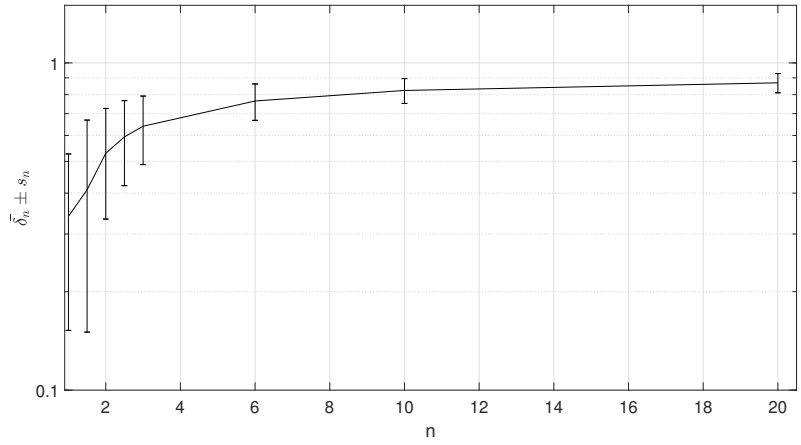

Figure 4.35: Relative error between the evaluated and the measured scour depth depending on n.

The values of n that fitted best the experimental data were those in the range n=1.0-2.0, where the difference between the experimental data and the theoretical result was smaller. According to Table 4.3, using a value of $n = 2$ gave a fairly good conservative estimation of the equilibrium depth. Ong et al. (2013) suggested to use n=10 to reproduce the upper values of the random wave-induced scour data for design purposes. In our experiments the value of n=10 led to an overestimation

Table 4.3: Measured and predicted scour for random waves.

WAVE	S(cm)	$S_n(cm)$							
		n=1.0	n=1.5	n=2.0	n=2.5	n=3.0	n=6.0	n=10.0	n=20
NR1	0.5	1.0	1.4	1.7	2.0	2.3	3.5	4.6	6.8
NR2	1.1	1.6	2.3	2.8	3.3	3.7	5.9	8.2	11.4
NR3	1.3	2.1	2.9	3.6	4.2	4.7	7.1	9.2	12.6
NR4	1.2	2.1	2.9	3.5	4.1	4.5	6.4	8.2	10.5
NR5	1.0	0.9	1.3	1.6	1.8	2.0	3.0	4.1	4.6
NR6	1.1	0.8	1.2	1.5	1.8	2.0	3.2	4.4	6.4
NR7	1.2	0.9	1.2	1.6	1.8	2.1	3.2	4.2	5.7
NR8	1.0	1.0	1.5	1.9	2.2	2.5	3.8	5.0	7.2
NR9	0.5	1.3	1.9	2.4	2.8	3.2	5.0	6.6	10.0

of the scour of around 80-90%. In the present study, use of half of the waves higher than w_{c1} (n=2) gave an estimation of the scour depth that was more accurate than that obtained with n=10, always ensuring a conservative estimate of around 30-70%. To provide a more practical methodology, a different approach is here provided. For each value of n, it is possible to compute $w_{c,d}$ calculated as the average of w_c higher than $w_{c1/n}$. Therefore, from the definition of w_c, the dimensional design crest height is calculated as $\eta_{c,d} = w_{c,d} \cdot A_{rms}$. Therefore, similarly to Equation 3.6, KC_η was evaluated as:

$$KC_\eta = \frac{2\pi\eta_{c,d}}{D\ \sinh(k_p h)}. \tag{4.12}$$

After evaluating the scour depth using this approach for the estimate of KC to be used in the equation of Sumer et al. (1992), the average ($\bar{\delta}_\eta$) and the standard deviation (s_η) of the difference between the measured and predicted values could be evaluated, as already done in Equation 4.11. The results of this computation are summarized in Figure 4.36.

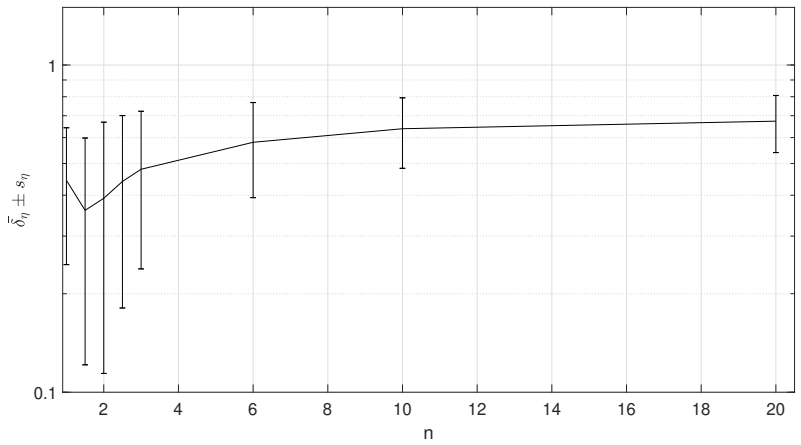

Figure 4.36: Relative error between the evaluated and the measured scour depending on every crest height $\eta_{c,d}$ associated to n.

The analysis of these data revealed that the method of Ong et al. (2013) was more conservative, always giving too large scour. However, the difference between these two methods is not so large and the choice of $n = 2$, even in this simplified method,

maintained some over-prediction of the scour depth (suitable for design purposes). Furthermore, the accuracy on the evaluation of the scour depth was around 10-60%, higher than that obtained previously. Therefore, the proposed simplification of the methodology of Ong et al. (2013) leads to a predicted value of scour which is similar but more accurate and always conservative for $n \geq 2$.

4.3 Particle Tracking Velocimetry (PTV)

The reconstruction of the velocity field by the non-intrusive method of *PTV* allows to obtain an undisturbed velocity field from which the study of the vortex generation and growth under waves can be carried out. In particular, in steady current conditions the horseshoe vortex is the most important phenomenon related to the scour formation while in wave only conditions, the lee-wake vortex can play a primary role. For this reason, the nearbed analysis refers to the horizontal plane closest to the bottom at the minimum $z_b = 4.6$cm. The trajectory of the particles has been reconstructed inside the *Region Of Interest*. The resolution of each single frame is 4096px×3072px and the camera is placed in a position in which it can record a whole quadrant guaranteeing an adequate overlapping zone between the upstream and downstream one (see Figure 4.37). The choice of the resolution of the camera depends on the area that has to be recorded, on its distance from the camera, on the lens characteristics and on the seeding size.

Figure 4.37: Example of a frame acquired for wave test $R2$: horizontal plane at z_b=4.6cm on the wake side of the pile.

The software used for this analysis is *YATS* (*Y*et *A*nother *T*racking *S*oftware) which has been presented in Miozzi (2004). Here, the *Feature Tracking* technique (Lucas and Kanade, 1981) is used for the individuation of particles at different frames. This method is based on the best correlation between two interrogation windows (time steps t and $t+1$), obtained by the minimum value of the *Sum of Squared Differences* (*SSD*) in terms of pixel intensity. The *SSD* is computed with:

$$SSD = \sum_{R} [J(W(\mathbf{x}, \mathbf{p})) - I(\mathbf{x})]^2 \tag{4.13}$$

in which I and J are the frames at time t and $t+dt$ and W is the warp operator which analyse the pixel $\mathbf{x}$ from frame I to J according to the translation and deformation parameters included in $\mathbf{p}$ (U, V, $\partial U/\partial x$, $\partial U/\partial y$, $\partial V/\partial x$, $\partial V/\partial y$). The minimum

value of SSD is obtained by solving iteratively the equation for small increments of the term Δp. The goodness of the tracking depends on the goodness of the image which must have a high luminosity gradient.
The first part of the analysis consists in the individuation of the particles and their hydrodynamic parameters (see Section 3.2.1). After the convergence of the iterative procedure is obtained, the informations about the seeding are obtained (positions and kinematic properties). Hence, those spread data are interpolated into a regular grid. This cell size must be chosen carefully because a coarser mesh could not allow a detailed analysis of the vortex pattern and a smaller one could give problem in the interpolation process if the seeding concentration is not large enough. After some preliminary tests it was found that, for this specific configuration, a discretization of 50px×50px represented the best compromise. The kinematic quantities, now located on a regular grid, are elaborated by means of the wave phase averaging technique described in Section 4.1.1 taking as a reference the water elevation signal of the gauge $WG5$ for the up-crossing. To associate a water level to each image, the elevation time series (acquired at 35Hz) has been interpolated in order to reach the frame rate of the camera (120fps). Each wave period has been divided in 80 phases by 4.5° each, in which the phase $\varphi = 0°$ corresponds to the up-crossing of η. Note that the crest phase does not correspond to $\varphi = 90°$ because of the nonlinearity of the wave.
In Figure 4.38 the results of the phase averaging for tests $R2$ and $R8$ are displayed. In particular, the velocities U (along x-axis) and V(along y-axis) used for the phase averaging are taken at a point of the image which is as far as possible from the cylinder in order to characterize the undisturbed flow.

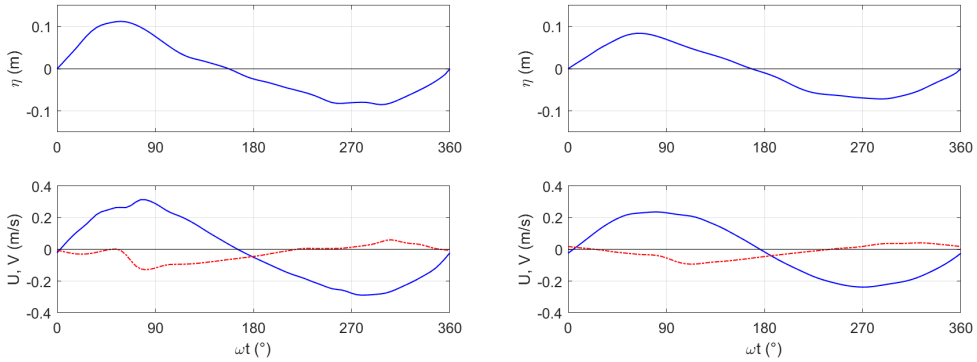

(a) (b)

Figure 4.38: Characterization of the phase-averaged undisturbed flow with PTV technique: measured water level at wave gauge $WG5$ (upper panels) and velocity along the x (blue line) and y (red line) axis (lower panels) for waves R2 (a) and R8 (b). Horizontal plane at $z_b = 4.6cm$.

Note that the horizontal velocity is almost zero in correspondence of the up-crossing, it is maximum under the crest and again zero at the down-crossing as expected. On the other side, the transversal velocity V should be always zero in an undisturbed x, z oscillatory motion. The separation of the waves of each test for the identification of the up-crossing is made by analysing the water surface signal at a point of the image far from the pile at a distance of $\approx D$ from it. Therefore, the presence of a small transversal component of the horizontal velocity V is expected

because the location where the analysis is conducted is not far enough from the pile, thus the streamlines are not perfectly parallel to the direction of the flume and a minimal influence of the contraction of the streamlines due to the presence of the obstacle still persists.
Equation 4.14 defines the vorticity as the curl of the flow velocity $\mathbf{U}(U, V)$ vector.

$$\omega = \nabla \times \boldsymbol{U} \tag{4.14}$$

Therefore, the vorticity can be used directly to identify vortices even if Kida and Miura (1998) highlighted how this method cannot distinguish between swirling motions and shearing motions; this is therefore a method for visualising vortices, not identifying their extension (Moin and Kim, 1985). Another method for vortex pattern identification, often used in oceanography or with bi-dimensional fluxes, is the *Okubo-Weiss* parameter (OW). Okubo (1970) analysed the dispersion of two particles, initially at the same position, studying their trajectories over the oceanic surface. He found out that the shape of the possible patterns of motion depends on the eigenvalues of the velocity gradient tensor. Weiss (1991) obtained a similar result using the enstrophy (integral of squared vorticity) of bi-dimensional turbulent flows. Therefore, the *Okubo-Weiss* parameter is obtained as:

$$OW = s^2 - \omega^2 \tag{4.15}$$

in which $s^2 = s_n^2 + s_s^2$ represents the deformation with normal component $s_n = \partial U/\partial x - \partial V/\partial y$ and tangential component $s_s = \partial V/\partial x + \partial U/\partial y$.
This parameter allows to separate the flow field into three different regions: elliptic regions (where $OW < 0$) which are dominated by vorticity, hyperbolic regions ($OW > 0$) dominated by deformations and intermediate regions ($OW \approx 0$).
The analysis of this parameter allows to identify the vortices as zones in which the presence of a vorticity region is surrounded by a deformation region.

Horizontal planes

Horizontal planes at z_b=4.6cm are studied according to the set-up of Figure 3.7a. An area of approximately 15cm×10cm after the pile is recorded. Four wave conditions of Table 3.1 have been analysed by means of the PTV technique: $R2$, $R8$, $R9$ and $R15$.

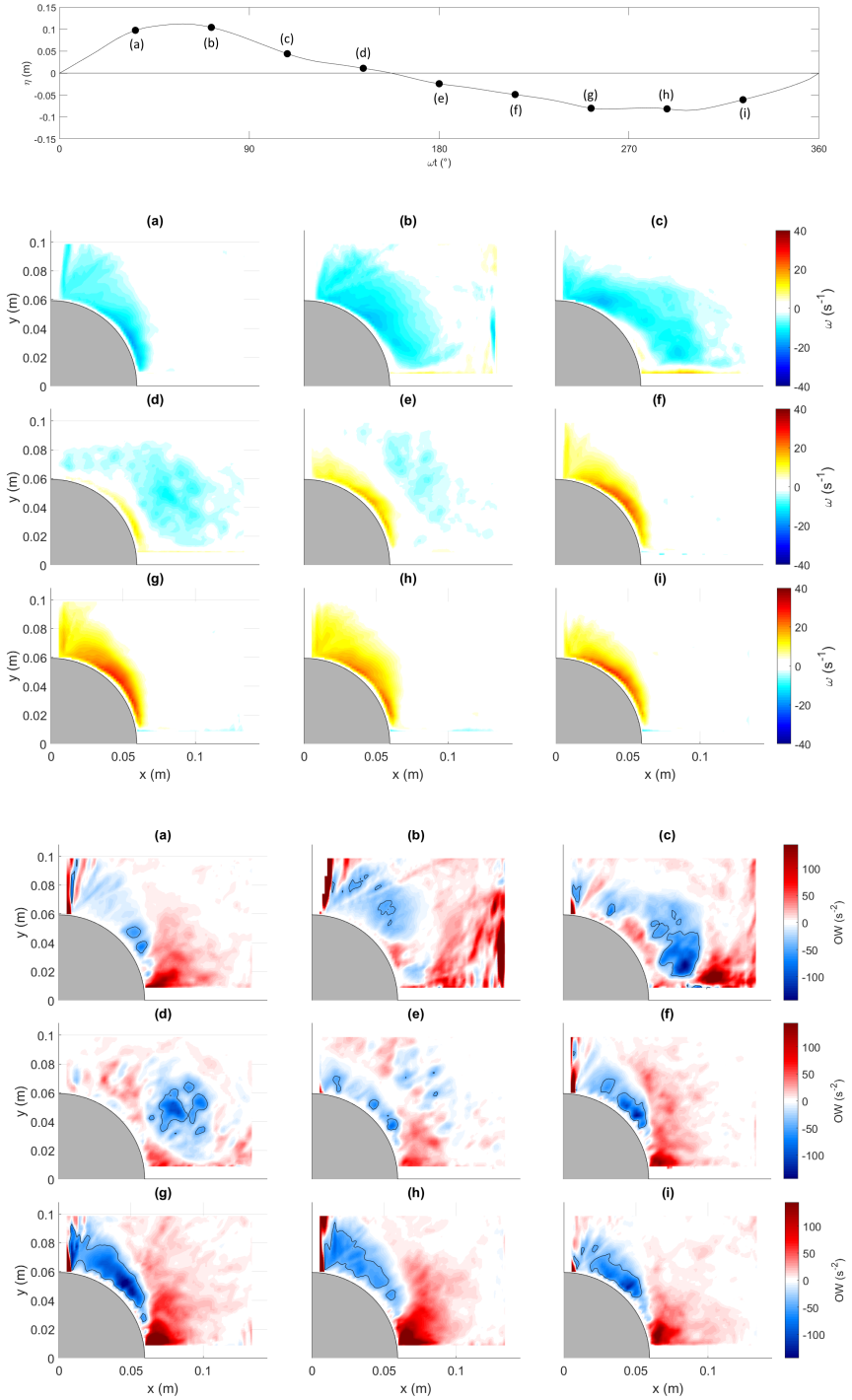

Figure 4.39: Vortex identification for wave $R2$. Upper panel: Phase-averaged wave and identification of main phases. 2D Vorticity maps ($s^{-}1$) (middle panels) and *Okubo-Weiss* contour (lower panels) for ωt=36°, 72°, 108°, 144°, 180°, 216°, 252°, 288° e 324° (a-i).

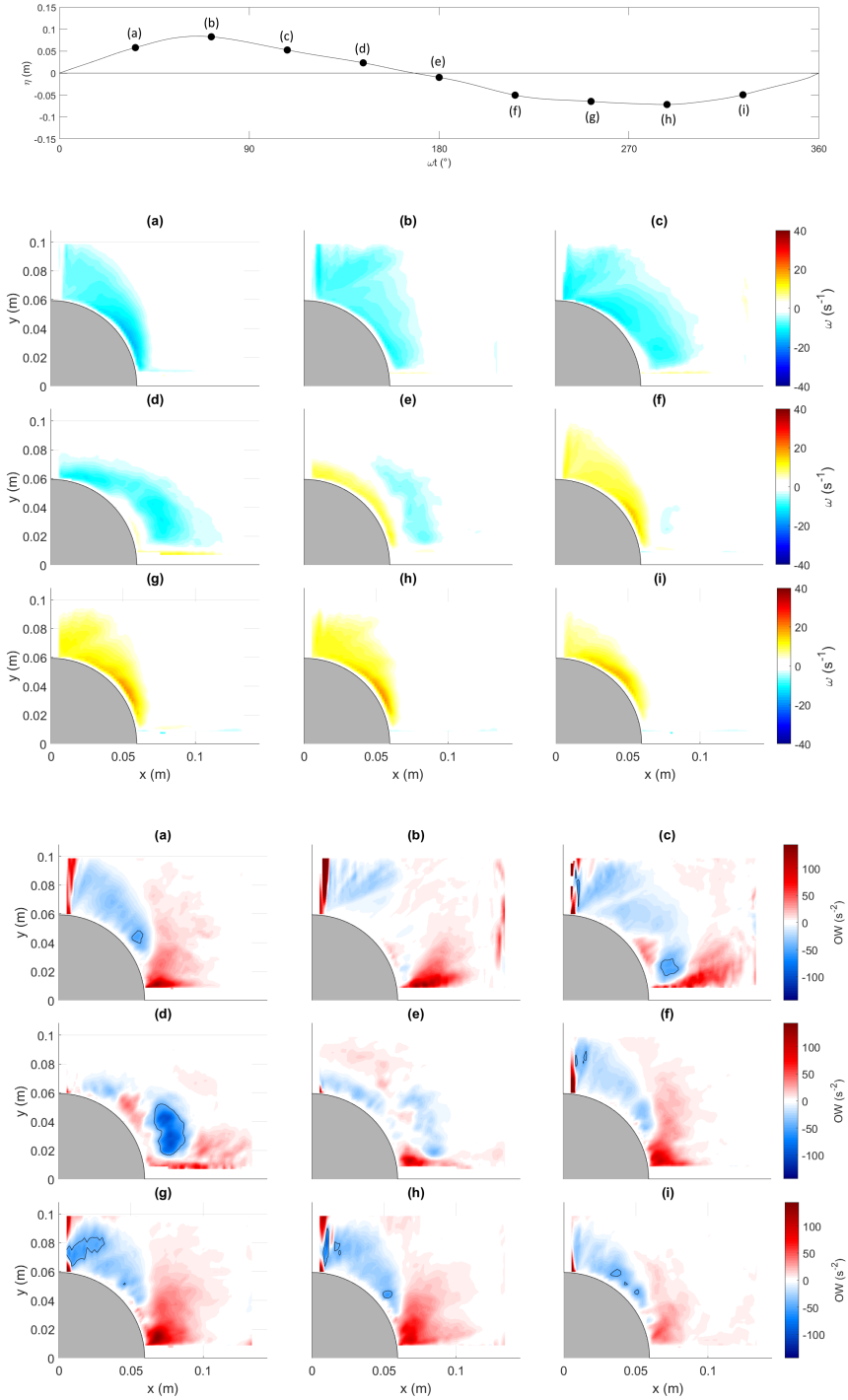

Figure 4.40: Vortex identification for wave $R8$. Upper panel: Phase-averaged wave and identification of main phases. 2D Vorticity maps ($s^{-}1$) (middle panels) and *Okubo-Weiss* contour (lower panels) for ωt=36°, 72°, 108°, 144°, 180°, 216°, 252°, 288° e 324° (a-i).

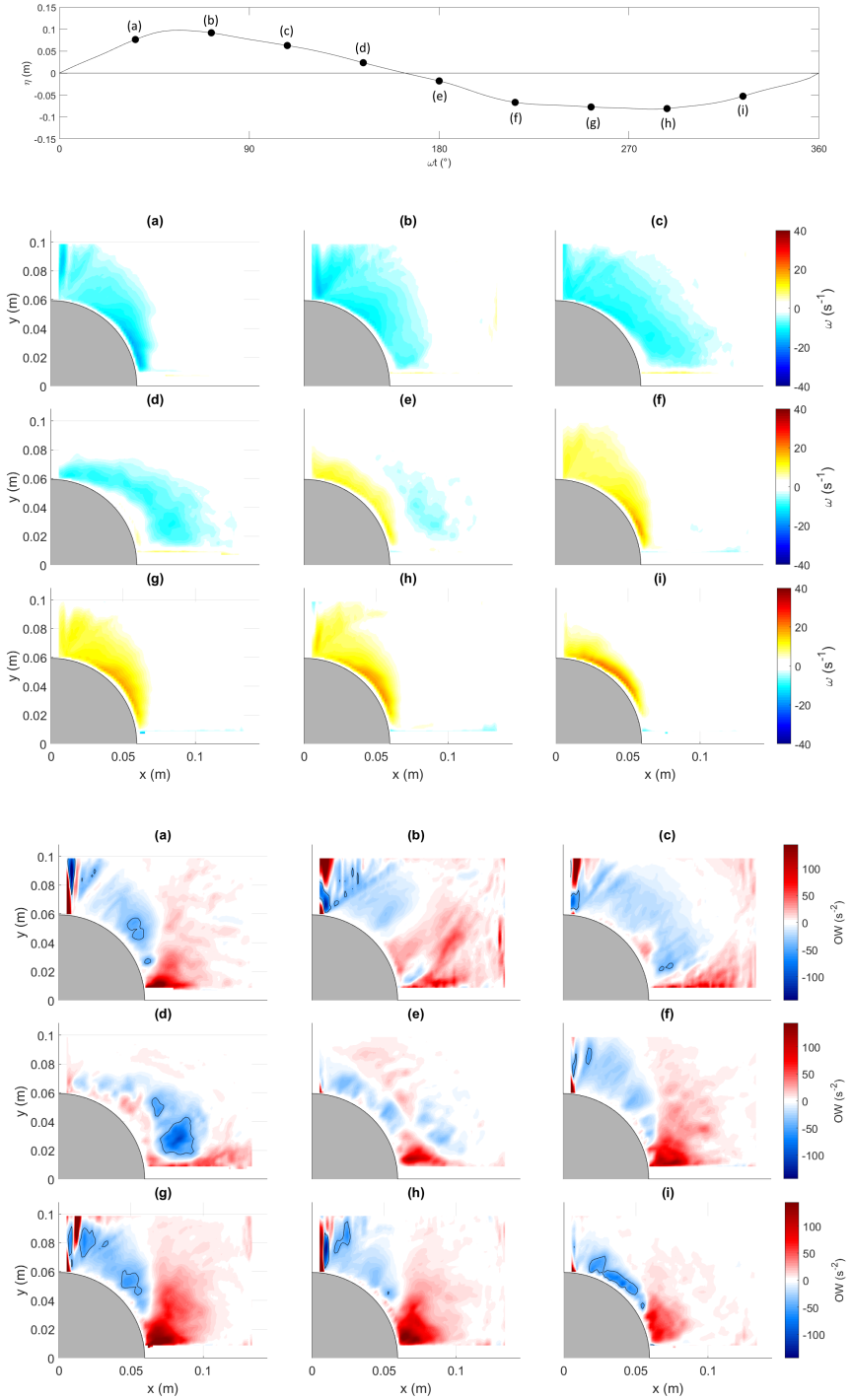

Figure 4.41: Vortex identification for wave $R9$. Upper panel: Phase-averaged wave and identification of main phases. 2D Vorticity maps ($s^{-}1$) (middle panels) and *Okubo-Weiss* contour (lower panels) for ωt=36°, 72°, 108°, 144°, 180°, 216°, 252°, 288° e 324° (a-i).

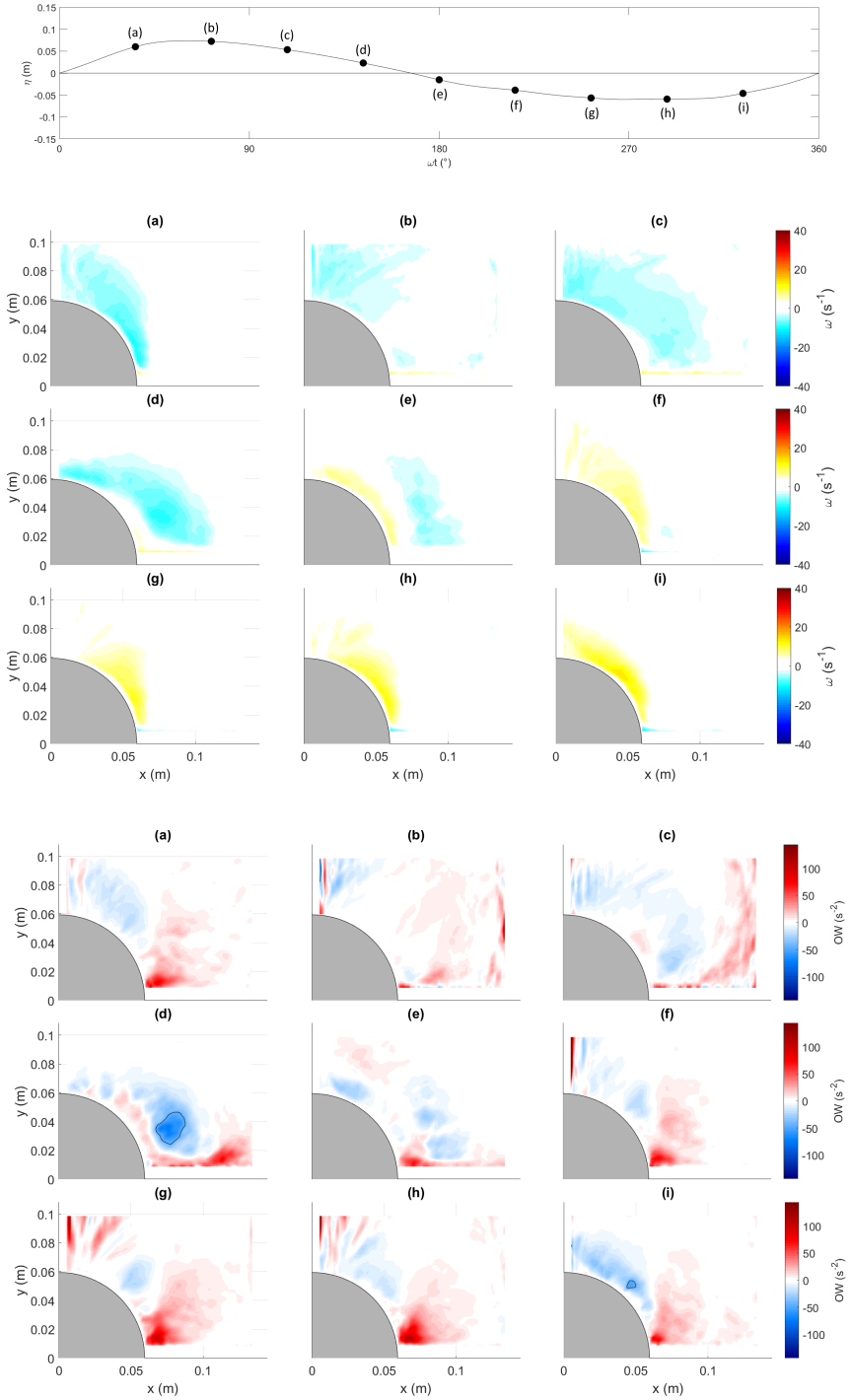

Figure 4.42: Vortex identification for wave $R15$. Upper panel: Phase-averaged wave and identification of main phases. 2D Vorticity maps ($s^{-}1$) (middle panels) and *Okubo-Weiss* contour (lower panels) for ωt=36°, 72°, 108°, 144°, 180°, 216°, 252°, 288° e 324° (a-i).

The wave conditions chosen for this analysis are representative of the hydrodynamic conditions in which the vortex generation starts (KC from 6 to 10 associated to two different wave periods). The results of Figure 4.39 to 4.42 show that, for all the selected wave conditions, after the passage of the crest ($\omega t \approx 110 - 130°$) a vortical structure is generated in the surroundings of the pile and than it grows. Than, it is shed and pushed laterally by the reversed flow ($\omega t \approx 170°$). The presence of the vortex is clear from the *Okubo-Weiss* parameter analysis; indeed, it is possible to find an inner blue zone (the core of the vortex where the vorticity is dominant and $OW < 0$) surrounded by a deformation zone where OW is greater than 0 (red colour). From the vorticity maps it is possible to visualize the vortices and their direction of rotation. In particular, in correspondence of the reversal of the flow, close to the pile it is generated a region in which the particles are moving anticlockwise (red colour), which becomes dominant with respect to the clockwise vortex (blue colour) generated in the positive elevation phases.
In Section 4.2.1 the results of the scour under regular waves are presented. The aim of the *Particle Tracking Velocimetry* analysis is to correlate the velocity and vorticity fields (studied in rigid bed conditions) to the seabed morphology at the equilibrium state. The correlation between the two experimental campaigns is not easy. Indeed, while the parameters that we showed to represent the velocity field depend on the wave phase, the scour plotted in Figure 4.29 represents an equilibrium condition obtained after the passage of a huge number of waves. The realization of a mobile bed model required the presence of a ramp along the flume in order to create a volume of sand (1.5m length, 1m wide, 0.16m thick) in which it was possible to allocate both the cylinder and the sand. The presence of the ramp in the first part of the flume, induces a large change in the shape of the waves which results more peaked in correspondence of the pile with respect to the wave generated at the paddle. Also in the rigid bed model a little variation of the wave (larger peaks) is observed with respect to that at the generation; however, such induced nonlinearity is smaller with respect to that induced in the mobile bed experiments by the presence of the ramp. On the other side, to record images from the bottom of the flume it is necessary to have a glassed window with no sediment over it. Therefore, it is impossible to perfectly reproduce the same wave characteristics on the two models, hence the same wave conditions at the paddle (here corresponding to the same wave name) will lead to different waves in correspondence of the pile. However, among the mobile bed tests (Table 3.2), similar conditions to the four wave conditions analysed with the PTV technique ($R2$, $R8$, $R9$ and $R15$ in Table 3.1) are found. The results of this comparison are shown in the following Table 4.4:

Table 4.4: Characteristics of regular waves at wave gauge in correspondence of the pile for both rigid bed model (left) and mobile bed model (right).

RIGID BED				MOBILE BED			
Name	H (m)	T (s)	KC (-)	Name	H (m)	T (s)	KC (-)
R2	0.19	2.74	10.0	R15	0.17	2.74	9.8
R8	0.16	2.19	5.6	R11	0.14	2.19	6.1
R9	0.19	2.19	7.6	R8	0.16	2.19	6.8
R15	0.13	2.74	6.8	R1	0.14	2.74	8.1

The correspondence between different tests has been done considering, among the waves with the same period which is kept constant in the two configurations, the conditions in which the wave height at the cylinder and, mainly, the KC number

(which is the main parameter in the scour evaluation) are more similar. It must be highlighted that the results in the analysis of the flow around the pile performed in rigid bed conditions, does not include the non-negligible effect of the seabed shape (ripples and scour) on the nearbed flow. The interpretation of the results must take care of this difference; however, the author believe that a qualitative interpretation of the results between the mobile bed and rigid bed campaigns can be done and can help the understandings of the physical processes.
The *Okubo-Weiss* contours in Figure 4.39 for wave $R2$ represents well the hydrodynamic of an intense flow around the pile. The vortex is generated in the wake side of the pile during the passage of the crest (phase b), it grows in dimension and intensity (c) until it completely detaches from the cylinder (d), it loses energy and it breaks and dissipates both laterally to the pile, driven by the reversal of the flow, and close to the cylinder surface. This analysis is in agreement with the results obtained from the pressure measurements. The phases of generation and growth of the vortex (phases "b"-"c" in Figure 4.39) corresponds to the phases in which the pressure gradient in the wake of the pile is maximum (phases "b"-"d" in Figure 4.26). Finally, when the vortex completely detaches from the pile (phase "d" in Figure 4.39) the pressure gradient becomes almost zero (phases "e"-"f" in Figure 4.26).
For a better comparison, in Figure 4.43 the corresponding scour equilibrium patterns with the test names of the rigid bed model according to Table 4.4 are reported.

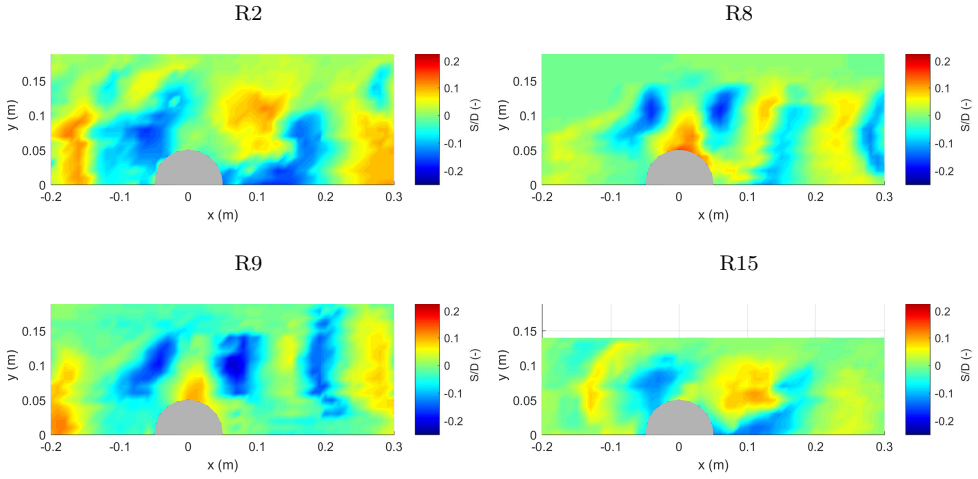

Figure 4.43: Seabed morphologies corresponding to the wave conditions analysed with PTV technique.

The vortex reaches the maximum intensity in the wake of the pile ($\varphi \approx 180°$) where the maximum scour for the corresponding wave occurs (blue zones in Figure 4.43). Hence, the vortex is driven on the lateral side and, decreasing in terms of intensity of vorticity (panels "e"-"f"), it releases the sediment particles that were previously put in suspension in the previous wave phases. Therefore, the sediment accumulates in the zone where the vortex loses intensity (lighter zones) leading to the formation of a deposit zone.
Wave $R8$ is characterized by a smaller period and height (and thus KC), so the intensity of the vorticity and of the scour is lower. However, it is quite clear the individuation of the position in which the boundary layer separates (after the passage

of the crest, $\omega t \approx 100°$ - panel "c", at $\varphi = 120° - 150°$). Here, the vortex is generated and grow up in intensity until it is dissipated from the flow (panel "h"). In this case the vortex is destroyed before being driven transversally on the lateral side of the pile. For this reason, in the corresponding scour map (Figure 4.43) is not found a deposit zone at $\varphi = 135°$ similar to that of the previous wave condition. The strong vorticity zone remains attached to the pile and, as a consequence, the sediment taken from the back of the pile, is not able to move away from it and it is deposited at $\varphi = 90°$. This deposit zone probably induced a small variation in the bottom profile that, wave after wave, amplifies this effect leading to the formations of the two small scour holes before and after this zone of accumulation of sediments (Figure 4.43).
Wave $R9$ has similar characteristics compared to wave $R8$, slightly higher wave height that leads to higher velocity at the bottom and, thus, KC. Therefore, the morphological pattern between the two corresponding waves (chosen more for their correspondence in terms of KC than in H) is similar even if in this situation, due to the higher intensity of the flow, the dimension of the ripples is more relevant. The analysis of the parameters for the visualization and individuation of vortices (Figure 4.41) gives the same qualitative results than the previous case. The shedding of the vortical structure from the cylinder occurs at $\varphi \approx 120°$ when $\omega t \approx 140°$ (panel "d"). Obviously the dimension of the vortex is larger compared to wave $R8$ but not as large as for wave $R2$. Therefore the vortex is divided at the reversal of the flow, one part is dissipated in the wake of the pile and a huge part is reversed and move back with the flow attached to the surface of the cylinder originating a deposition zone approximately at $\varphi = 90°$.
Among the analysed conditions, wave $R15$ (Figure 4.42) is the weaker one; thus, the intensity of both the vorticity and OW contours is the lowest. The total area of influence of the vortices is lower and, as a consequence, the zone where the scour takes place is smaller. In this case, from the vorticity map at $\omega t = 108°$, there is a zone at $\varphi \approx 120°$, attached to the pile, characterized by an absence of rotation ($\omega \approx 0s^{-}1$) where the shedding starts. When $\omega t = 144°$ (panel "d") the vortex is detached and it is immediately destroyed (panel "e"). Differently from the previous conditions, here there is not an intense anticlockwise vorticity (small yellow zone in panels "f" and "g") thus leading to a morphological configuration that differs from the previous of $R8$ and $R9$. For this reason, the sediment is not driven back completely up to $\varphi = 90°$ but in this case the deposition zone is placed at about $\varphi = 135°$ very close to the pile and the erosion occurred where the vortex was stronger, at the back of the pile. As already mentioned, the lower intensity of the flow leads to lower values of erosion/deposition.

Vertical planes

According to the configuration represented in the sketch of Figure 3.7b, two vertical planes are studied with a recorded area of approximately 10cm×20cm (before the pile) and 15cm×20cm (after the pile). The results for the *Okubo-Weiss* parameter of wave $R15$ are presented in Figure 4.44 and Figure 4.45.

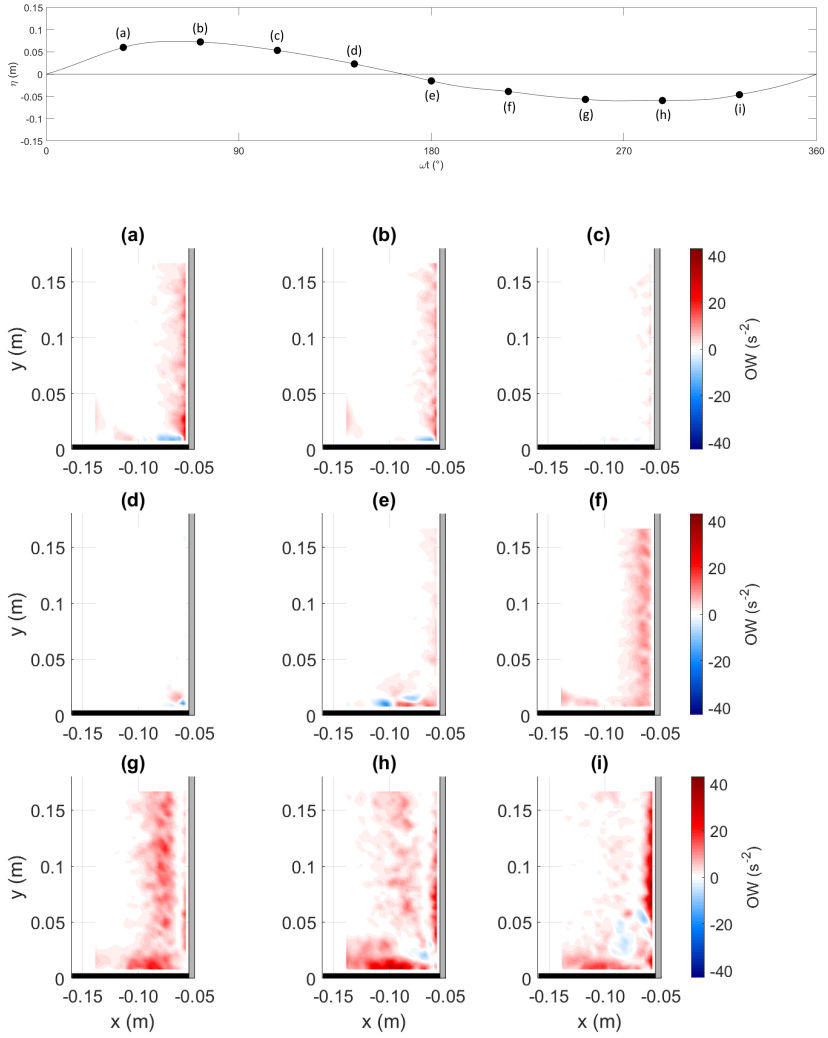

Figure 4.44: Vortex identification for wave $R15$. Upper panel: Phase averaged wave and identification of main phases. Lower panels: *Okubo-Weiss* contour for ωt=36°, 72°, 108°, 144°, 180°, 216°, 252°, 288° e 324° (a-i) for the vertical plane before the pile.

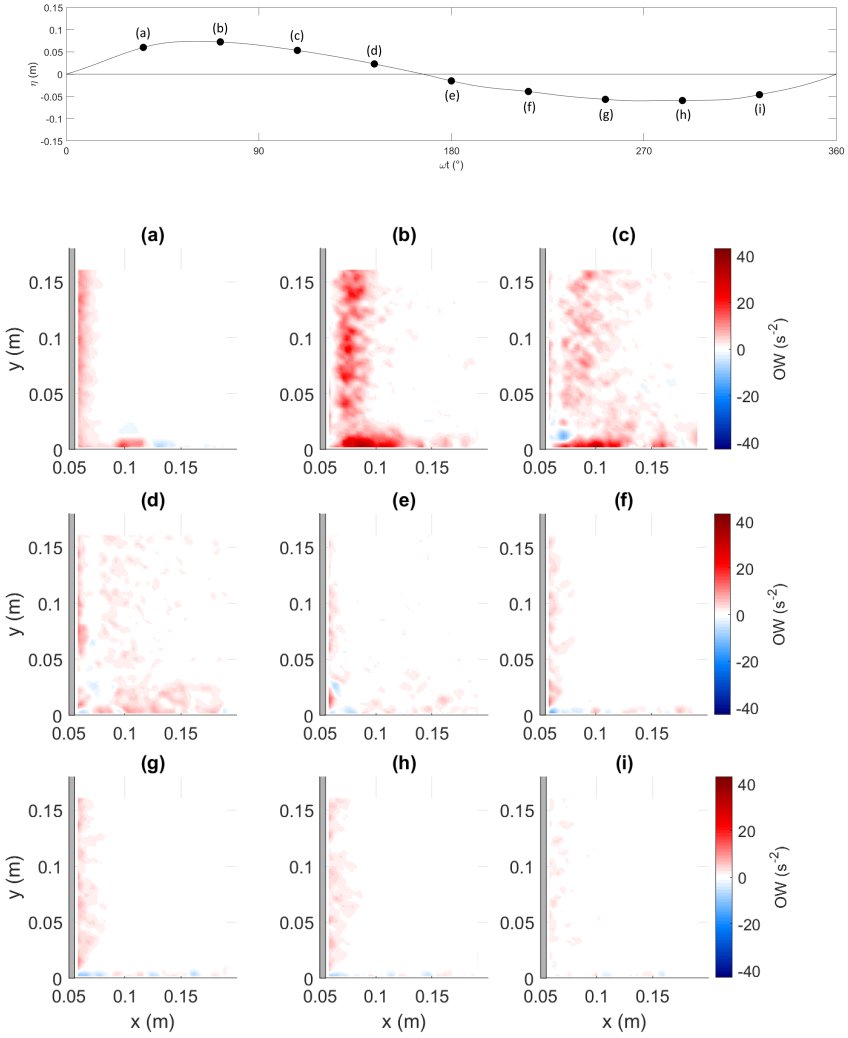

Figure 4.45: Vortex identification for wave $R15$. Upper panel: Phase averaged wave and identification of main phases. Lower panels: *Okubo-Weiss* contour for ωt=36°, 72°, 108°, 144°, 180°, 216°, 252°, 288° e 324° (a-i) for the vertical plane after the pile.

From these vertical planes it is possible to evaluate the formation of the horseshoe vortex at the stagnation point and the growth and destruction of the lee-wake vortices after the pile. The horseshoe vortex should appear as a vorticity zone (blue) surrounded by a deformation zone (red) in front of the pile (Figure 4.44) mainly under the crest phase (panels "a"-"b"). The results are in a quite good agreement with this; in panels "a" and "b" of Figure 4.44 it is possible to find this small area even if it is not so clear as expected. Probably, it depends on the characteristic of the flow; as the value of KC increases, as the relative importance of the horseshoe vortex increases (Sumer et al., 1997). Therefore, because of the value of the *Keulegan-Carpenter* parameter of this wave, the wake vortices are expected to be

dominant with respect to the horseshoe vortices. Even if this wave is not remarkably peaked, the crest phase lasts for a shorter time with respect to the trough phase. As an indirect consequence, the velocities under the crest are higher and, therefore, the lee-wake vortices on the back of the pile are expected to be larger than those in the front (originated from the reverse flow). It is possible to individuate the zones in which those vortices are present. In particular, in a vertical plane, a vertical axis vortex is not easily determined. Considering Figure 2.1, the lee-wake vortex tends to keep the particles in the wake zone of the pile, while the surrounding flow is moving downstream. The analysis of this phenomenon in a vertical plane will lead to the individuation of a zone in which the strain is really high (because of the high value of the term $\partial U/\partial x$ included in the deformation component s of Equation 4.15), this zone corresponds to the boundary between the wake vortex and the undisturbed flow and it is useful to have an idea of their area of influence. The core of the lee-wake vortices do not reach the vertical plane analysed (central axis of the cylinder) hence in such plane only the strain zone is present. It is found in the horizontal planes that lee-wake vortices were formed, hence such strain region visible in the vertical planes represents the surroundings of vortical zones. From Figure 4.44 the vortices in front of the pile are generate at the beginning of the trough phase (panel "f"), they grown in intensity reaching the peak at $\varphi \approx 250°$ and after they progressively disappear before the up-crossing. On the wake of the cylinder (Figure 4.45) almost the same considerations can be done with some difference. First of all, no significant presence of horseshoe vortex is highlighted. In front of the pile a small vorticity region possibly due to small vortices is observed during the crest phases (panels "a"-"b" in Figure 4.44). On the contrary, after the reversal of the flow it is expected the same effect on the wake of the pile during the trough phase (panels "f"-"h" in Figure 4.45). The almost complete absence of this vorticity region can depend on the intensity of the flow. Considering that it was not clear their visualization in front of the pile where they are supposed to be larger, on the back of the pile they seems not to be present at all. On the other side, the wake vortex is well identified by means of the strain region and it reaches his maximum value under the crest phase on the bottom of the flume and it extends up to x=0.15m, that perfectly coincides to the extension of the scour zone of the corresponding wave (Figure 4.43). Moreover, in comparison with the results of the vertical plane before the pile, the intensity of the OW parameter is higher but its duration is shorter because of the shorter duration of the positive elevation phases with respect to the negative ones (it is almost completely dissipated at $\varphi = 108°$ - panel "c").

4.4 Scale effects

Flume experiments on local scour around a vertical slender cylinder can be affected by scale effects. Scale effects were such that laboratory conditions gave values of relative scour depth larger than those that would occur in natural flows (Ettema et al., 1998). This indicates that experimental formulae generally overpredict scour depths (Ettema et al., 1998). Ettema et al. (2006) argued that there are three independent length scales in local scour experiments: the cylinder diameter D, the sediment particle diameter d_{50} and the flow depth h, hence, a full dynamic-similarity cannot be satisfied. In scour modelling, the pile *Reynolds* number (Re_D) is typically high and, hence, viscous effects are negligible. Therefore, conservation of the *Froude* number is

regarded as most relevant and the design of the experiments was based on *Froude* similarity. It is difficult to achieve high Reynolds number Re (in the present experiment $Re = AU_m/\nu$ is in the range $1.4 \times 10^4 - 2.4 \times 10^5$) and condition of fully turbulent flow in wave flume experiments, hence, being the flow in transition condition, some viscous effects exist, as well as some related scale effects.
As reported by Sumer et al. (1992) if the surface of the pile acts as an hydraulically smooth-surface, some influence of Re_D is expected on the downstream vortex shedding pattern. The pile Reynolds number can be neglected only if the flow around the pile is fully turbulent (Ettema et al., 1998). It has been found that, for the waves here analysed, the pile acted as a smooth wall. Therefore, as expected, the experimental results of the present study reveal that the Reynolds number influences the flow and, hence, the seabed morphology. In particular, a slight decrease of the scour depth has been found with an increase of Re_D. Such results are in agreement with the findings of Tavouktsoglou et al. (2017), that noted how an increase in Re_D leads to a decrease of the dimensionless scour depth.

4.5 Discussion on the experimental results

The two experimental campaigns have been realised for the better understanding of the hydro and morpho-dynamic processes related to the presence of a vertical cylinder in the marine environment. In particular, the thesis aims to give information that can be considered a useful support of the design process and, moreover, to increase the comprehension of a complex 3D physical phenomenon such as the vortex generation and detachment due to the wave-structure interaction. The evaluation of the force due to the wave action is of primary importance on the design of a piled structure. Wave forces on such slender structures are usually calculated by the *Morison* equation. Among the limitations of this approach, the use of the linear wave theory to real applications, in which the waves are characterized by nonlinear behaviour, is the stronger assumption. In the present thesis a method for the evaluation of the velocity, and thus forces, under nonlinear waves is proposed. It consists in the *Fourier* decomposition of the water elevation signal and the reconstruction of the velocity field as a superposition of the single components contribution computed with the *Airy* linear theory. The recommended practice (Det Norske Veritas, 2010) about wave induced loads on slender members suggests to use more exact theory for the total force evaluation. This approach could be chosen because it gave very good results especially for the evaluation of the total force. In particular, both the maximum values and the phase in which they occur are very well predicted and it could be a valid alternative to other wave theories to apply in the design process (e.g. *Stokes*, cnoidal, stream function).
The equilibrium seabed morphology under regular and random waves has been experimentally evaluated and the results are compared with the main formulas available in the literature. From the mobile bed experiments of this thesis, the scour process under nonlinear waves has been found to begin for values of $KC > 4$, differently from the results obtained from previous studies on linear waves ($KC > 6$). This finding would have a notable effect on the design of the protection at the base of such structures if the scour process starts for weaker wave conditions. However, the main scour formula of Sumer et al. (1992) appears to give a good estimation of the scour even if a spread of data is observed. Being nonlinear the waves analysed in the present thesis, a relation for the evaluation of the dimensionless scour depending on the Ur parameter

is presented, however further experiments are needed to be validated. For random waves, the equation of Sumer et al. (1992) did not give good results. Therefore, the method of Ong et al. (2013), depending on the cumulative distribution of the crest heights, has been applied and the results are very satisfying. However, due to the high complexity of the method, a simplification is proposed. The results obtained with this modified approach are almost equivalent to the original one but its application can be considered easier and more suitable for design purposes.
The analysis of the pressure gradients, in addition to the results of the PTV experiments, allowed to better explain the generation, growth and detachment of vortices under regular waves. The wave phases and positions in which the maximum values of the pressure gradients occur correspond to those in which the detachment of vortices is observed. From the interpretation of the contour maps of the vorticity and of the OW parameter it is possible to explain the scour patterns obtained in the mobile bed campaign. The zones in which the vortices have the maximum intensity correspond to those in which the sediment is put in suspension and hence carried with the flow until it lose energy and a deposition zone is generated (generally on the zone $\varphi = 135°$).
The results obtained from this experimental campaign allowed to extend the comprehension of the hydrodynamics and of the scour process around the pile by linking the variety of results (force, pressure gradients, velocities, vorticity, seabed morphology). By means of the inspection of such experimental results, useful information for the design process (force and scour estimation) of a cylindrical structures in the marine environment under the action of nonlinear waves were provided and one of the main objective of the thesis is achieved.

Chapter 5

Numerical set-up, Analysis and Results

Numerical modelling of wave-structure interaction is one of the most relevant challenges in coastal engineering research during the last years and, always more, it is a valid support to the design process because of its ability to obtain informations difficult to obtain with an analytical formulation or by an experimental model. The nonlinear waves of the rigid bed campaign are here reproduced for the better comprehension of the vortex formation process and for the estimation of wave run-up that is very important on the design of the access facility of marine structures such as oil platforms or monopile foundations of offshore wind turbines.
The hydro and morpho-dynamics under nonlinear waves is significantly different with respect to that induced by linear waves, as observed in the mobile bed experimental campaign (Section 3.3). To take into account the nonlinearity of waves in the evaluation of loadings and hydrodynamics on offshore structures, a combined use of experimental and numerical models is recommended. Nowadays, the mathematical modelling of waves and coastal structures is done by solving $RANS$-type equations, due to their good approximation of the physical phenomena and their relative small computational costs (with respect to LES and DNS models). However, the complexity given by the three-dimensionality of most part of wave-structure problems, demands overcoming existing modelling limitations.
OpenFOAM® (*Open* *F*ield *O*peration *A*nd *M*anipulation) is a robust *CFD* code widely used by a large number of companies and research institutes. It is an open source toolbox, so one of its main advantage is that it is free and the user can directly modify the source code and can control each step of the solving procedure. Finite volume discretization to solve different type of problems (hydrodynamic, electromagnetic, chemical etc.) is used. Among the solvers included in OpenFOAM®, "interFoam" solves the 3D *Reynolds Averaged Navier-Stokes* ($RANS$) equations for a two phase flow using the volume of fluid (VOF) method. According to Berberovic et al. (2009), each phase is described by a fraction α_i (usually α_i=0 for air and α_i=1 for water). Defining α_1 as the VOF indicator function, the density of the cell is computed as:

$$\rho = \alpha_1 \rho_{water} + (1 - \alpha_1)\rho_{air} \tag{5.1}$$

Moreover, the fluid movement is tracked by a classic advection equation:

$$\frac{\partial \alpha_1}{\partial t} + \nabla \cdot \mathbf{U}\alpha_1 \tag{5.2}$$

where $\mathbf{U}$ is the velocity vector. This scheme allows a quite easy representation of complex free surface configurations involving no mesh motion. The $RANS$ equations solved by "interFoam" consider the continuity of the fluid (Equation 5.3)) and the mass conservation (Equation 5.4):

$$\nabla \cdot \mathbf{U} = 0 \tag{5.3}$$

$$\frac{\partial \rho \mathbf{U}}{\partial t} + \nabla \cdot (\rho \mathbf{U}\mathbf{U}) - \nabla \cdot (\mu_{eff} \nabla \mathbf{U}) = -\nabla p^* - g \cdot \mathbf{X} \nabla \rho + \nabla \mathbf{U} \cdot \nabla \mu_{eff} + \sigma \kappa \nabla \alpha_1 \tag{5.4}$$

where μ_{eff} is the efficient dynamic viscosity, $\mathbf{X}$ is the position vector, κ is the curvature of the interface, p^* is the pseudo-dynamic pressure and σ is the surface tension coefficient. A detailed description of those parameters can be found in Higuera et al. (2013a).
Several turbulence models are supported. The $\kappa - \varepsilon$ model is quite accurate to simulate free flow regions whereas better results are obtained with $\kappa - \omega$ models that work better inside the boundary layer region. Menter (1994) developed the $\kappa - \omega SST$ model taking the best from the previous two models, using the first one in the free flow region and the second one closer to boundaries and a linear of them in the transition region. The goodness of this combined closure model has been extensively verified by Higuera et al. (2013b). In the present thesis, a $\kappa - \omega SST$ closure model with a stabilized version of the Reynolds-averaged stress ($StabRAS$) library has been used (Larsen and Fuhrman, 2018). In previous CFD studies it has been noted how the turbulence levels are often over-predicted due to the instability of two-equation turbulence closure models in the nearly potential flow region (Mayer and Madsen, 2000) which can lead to exponential growth of the turbulent kinetic energy and eddy viscosity. Significant advantages of using stabilized closures are demonstrated in the CFD simulation of both non-breaking and breaking waves. At the present, different wave theories can be supplied to generate waves (Stokes I,II and V, cnoidal, stream function or solitary wave) from static or moving boundary (Higuera et al. (2015)) with or without active wave absorption.

5.1 Model overview and new wave generation boundary condition

The numerical domain reproduces the investigation area of the experimental campaign of Section 3.2. In particular, according to Figure 3.2 it extends from the position of the wave gauge $WG2$ and it's 7.72m long, 1m wide (as the wave flume) and 1m high (Figure 5.1).

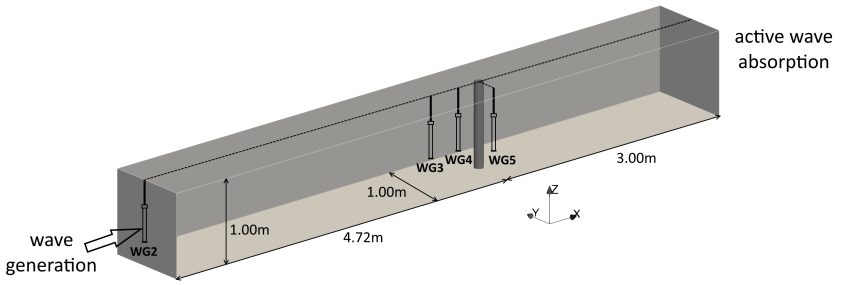

Figure 5.1: Sketch of the numerical model domain characteristics and wave gauges sensors positions

Different water level sensors were placed in the numerical domain in accordance with the physical set-up: $WG2$ in (-4.72; 0.00), $WG3$ in (-0.72; 0.00), $WG4$ in (-0.32; 0.00), $WG5$ in (0.00; -0.32). Furthermore, other numerical sensors are placed in the positions where the ADV is placed (in correspondence of $WG4$) for the analysis of the velocity and other control points are placed on the surface of the pile to measure the pressure in the position of the transducers over the surface of the pile (Figure 3.3). The generation of waves takes place on the boundary where the wave gauge $WG2$ is placed, on the opposite side an active wave absorption boundary is placed (Higuera et al., 2013a).
The two major mesh generation tools typically used in OpenFOAM® are called "blockMesh" and "snappyHexMesh". The principle behind "blockMesh" is to decompose the domain geometry into a set of 1 or more three dimensional, hexahedral blocks. Edges of the blocks can be straight lines, arcs or splines. "blockMesh" generates the mesh from a dictionary file which has to be prepared by the user according to the geometry to create. The user has complete control over the creation of the mesh which yields to a higher stability of the model both in terms of computational time and robustness (using only hexahedral cells). However, the compilation of the dictionary file can be a hard task for a geometry which is not so simple. The "snappyHexMesh" utility generates meshes containing hexahedra (hex) and split-hexahedra (split-hex) automatically from surface geometries in Stereolithography (STL) or Wavefront Object (OBJ) format. The mesh approximately conforms to the surface by iteratively refining a starting mesh and morphing the resulting split-hex mesh to the surface. Its main advantage is that the creation of the mesh is rather simple and it suits well to complex surfaces. On the other side, the presence of smaller tetrahedral cells to fit the surface increases noticeably the computational time due to the smaller time step needed to ensure an adequate *Courant* number. Because of the simplicity of the geometry and in order to obtain a model more robust and fast, the mesh is realised with "blockMesh" utility. Three different refinement levels were analysed to assess the sensitivity of the model grid. The domain is made by hexahedral cells only, with an uniform refinement level on the z direction and a coarser one on x, y in the zone far from the cylinder. The details of the different meshes around the pile are found in Figure 5.2 and the main characteristics are summarized in Table 5.1.

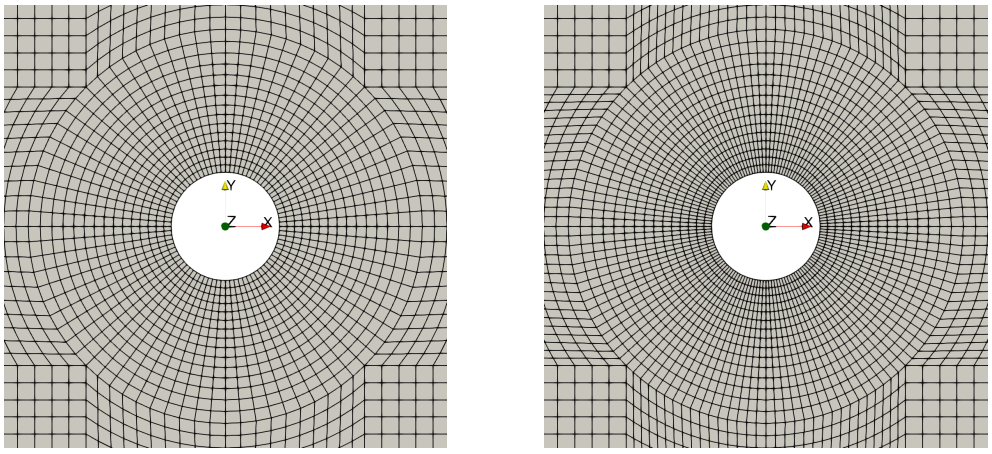

(a) (b)

Figure 5.2: Detail of the mesh around the pile for refinement levels 1,2 (a) and 3 (b)

The grid with the refinement level 1 is shown in Figure 5.2a. Here, the coarser part of the grid is made by cells with the approximate dimensions of 2×2.5cm; around the cylinder the resolution is higher, up to 0.43×0.75cm ensuring the presence of 80 cells along the circumference of the pile. The resolution over the z axis is kept constant and equal to 2.0cm. The refinement level 2 has the same horizontal discretization of level 1 (Figure 5.2a) but a higher refinement level over the z direction where the height of the cells is about 1.25cm. The higher refinement level 3 has the same vertical cells dimension than the previous one but the horizontal density of cells around the cylinder increases. Here, their size drop to 0.27×0.75cm and the number of cells around the circumference increases up to 128 (Figure 5.2b).

Table 5.1: Characteristics of regular waves at wave gauge $S4$.

Refinement Level	Elements along the circumference	Δz (cm)	Total num. of elements
1	80	2.00	1.1Mln
2	80	1.25	1.8Mln
3	128	1.25	2.3Mln

The total number of elements of the grids varies from 1.1Mln of the coarser mesh up to 2.3Mln. The maximum *Courant* number was set to be 0.5. The initial time step is 0.01s and it's adapted during the simulation according to the *Courant* number. The dependence of the numerical accuracy on the spatial grid resolution is studied through a mesh sensitivity analysis performed by checking the results in terms of total force over the pile, which is more sensible to a small variation of the mesh density. Indeed, no significant variations are recorded among the different domains in terms of water surface elevation in correspondence of the wave gauges.

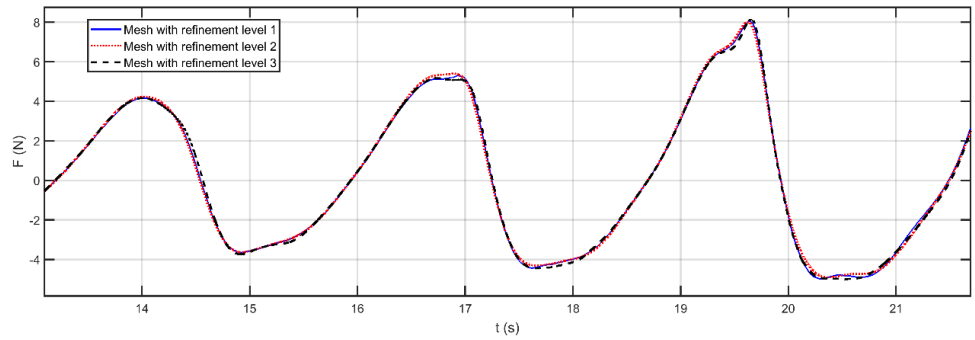

Figure 5.3: Time series of wave force over the pile using three different levels of mesh refinement

As shown in Figure 5.3, the time histories of the wave force with different mesh refinements does not show a notable scatter, hence the resolution of the grid can be considered accurate enough. The validation of the model and, thus, the comparison with the experimental data, have been performed by using the mesh corresponding to the refinement level 2, as a good compromise between the accuracy and reliability of the model and computational costs.
The aim of these numerical simulations was to reproduce in the better way the experimental tests. It must be noted that even if the wave generation in the physical flume occurs according to *Stokes I* order theory, a piston type wave maker in the wave generation generates nonlinear effects that modifies its characteristics especially during the wave propagation along the flume. As highlighted by Barthel et al. (1983), when first order wave generation theory is used, the group bounded wave is not reproduced and, thus, spurious free waves are generated into the flume introducing second order effect. For this reason, a new boundary condition was added to OpenFOAM® to allow the generation of waves from an experimental water elevation time series. The nonlinearity of the wave is taken into account by considering it as an irregular wave with specific spectral components (amplitude, frequency and phase) obtained by means of *fft* function as follows:

$$X_n = fft(\eta_0(t))/N_{tot} \tag{5.5}$$

where $\eta_0(t)$ is the experimental water elevation time series at the location of the wave generation, N_{tot} is the total numbers of samples of the time series and X_n is the complex amplitude for each wave component n_i. The complex amplitude associated to each component can be decomposed into its absolute part ($a_n = 2|X_n|$), which gives the amplitude of each wave component, and its phase angle ϕ_n. Therefore, the water surface elevation at the inlet boundary can be reconstructed as:

$$\eta_0(t) = \sum_{n_i=1}^{N_{tot}} a_n \cos(2\pi f_n t + \phi_n) \tag{5.6}$$

where f_n is the frequency of each wave component n_i.
The velocities (U and W) boundary conditions to be applied at the inlet patch of the numerical model are hence obtained as a linear superposition of the component

velocities computed according to *Airy*'s wave theory as follows:

$$U(z,t) = \sum_{n_i=1}^{N_{tot}} a_n 2\pi f_n \frac{\cosh(k_n(h+z))}{\sinh(k_n h)} \cos(2\pi f_n t + \phi_n) \tag{5.7}$$

$$W(z,t) = \sum_{n_i=1}^{N_{tot}} a_n 2\pi f_n \frac{\sinh(k_n(h+z))}{\sinh(k_n h)} \sin(2\pi f_n t + \phi_n) \tag{5.8}$$

in which k_n is the wave number associated to the frequency n_i. For the model to work properly, only the free surface (VOF function obtained from Equation 5.6) and velocities (Equations 5.7 and 5.8) are imposed as *Dirichlet* boundary conditions at the inlet patch. Pressure is computed using a *Neumann* boundary condition to avoid an overspecification of the case.
Note that Equations 5.7 and 5.8 are only valid in the case in which the direction of propagation of wave is orthogonal to the wave generating boundary, hence the component v is set to zero and no directional terms are present.

5.2 Model validation

The huge amount of available experimental data from the rigid bed experimental campaign allows a full validation of the numerical model. The test "R15" from Table 3.1 has been used for the validation of the results. The reasons of the choice of this wave condition are different. First, the wave period, and thus the wave length, is the largest. In particular, if the ratio between the wave length and the length of the domain is elevated, the length of the domain should be increased. However, the use of active wave absorption outlet condition, instead of a wave damping zone (Celebi et al., 1998; Jacobsen et al., 2012), allows the generation of waves with a length (≈5.80m in this case) which is comparable to that of the numerical flume (7.72m). Hence, if the model works well for these wave characteristics it can be considered reliable for the other conditions. Furthermore, this wave condition has been chosen as the reference condition because its hydrodynamics has been extensively studied in previous works (Miozzi et al., 2019; Corvaro et al., 2018b). The duration of this simulation was 60s and it took about 60h in 8 processors on a 3.6GHz machine to be completed.
In the following subsections the validation of the results is reported. In particular, the comparison of the recorded and measured time series of all the hydrodynamic quantities analysed (water level, horizontal velocity, pressure and total force over the pile) is reported. The comparison reported in the following sections has been done in the time period from 25s to 60s, after the experimental ramping time period.

Water level

The comparison of the water level time series is performed by the records of the four wave gauges that are placed into the numerical domain ($WG2$ to $WG5$ in Figure 5.1). The results of the comparison between experimental and numerical data are shown in Figure 5.4.

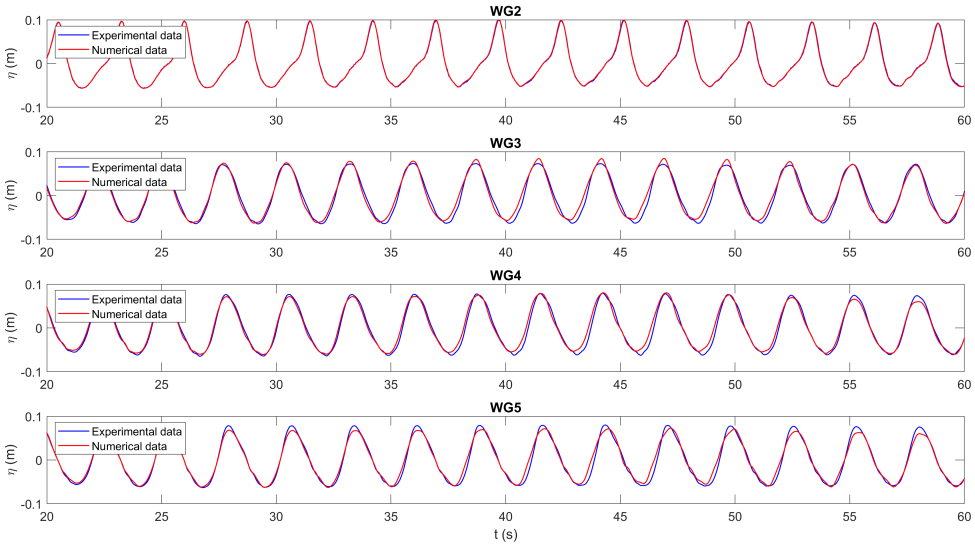

Figure 5.4: Water level time series: comparison between experimental and numerical data for test "R15"

The new wave boundary condition implemented in the code (Equations from 5.5 to 5.8) allows an excellent generation into the domain of the experimental signal. $WG2$ is placed at the beginning of the numerical domain and it is used to verify that the inlet water elevation is reproduced correctly. With this condition, it can be generated a wave not associated to a specific wave theory, thus including nonlinear effects. The wave propagation along the flume gives excellent results comparing the time series in correspondence of the other wave gauges. The superposition between the signals is very good; a small difference can be observed at $WG5$, which is located on the lateral side of the pile. This difference is assessed to be around 10% under crest phase and negligible under the though.

Horizontal velocity

One of the main advantages of numerical modelling is the possibility to measure different quantities at the same time in different locations without any kind of effort, except for computational costs. On the contrary, to perform experimental measurements of particle velocity the instrument must be placed into the water and it can represent an obstacle to the flow. For this reason, as previously explained, when ADV measurements are carried on, no measurements of pressure and force are done because the influence of the presence of the instrument cannot be considered negligible. The measurement of the horizontal velocity started when waves reached a "stationary" state and it was moved at different water depths without stopping the wave paddle.

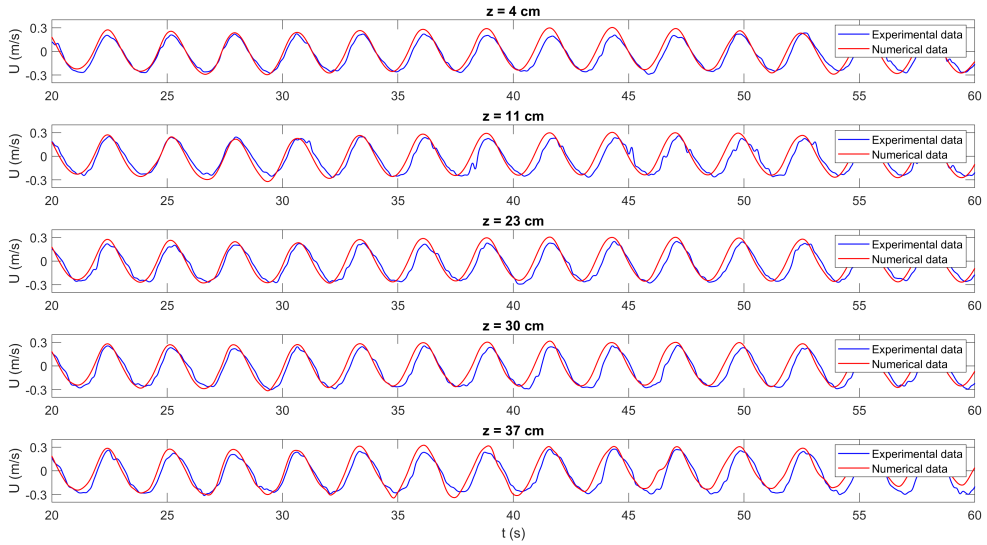

Figure 5.5: Horizontal velocity time series: comparison between experimental and numerical data for test "R15" at different depths from the bottom

The number of waves in each test is not enough to carry out turbulence measurement, but in the context of a qualitative comparison with a numerical model, the length of the time history is satisfactory. Here, the synchronization has been done according to the signal of the water level of the wave gauge $WG4$, in correspondence of the ADV.
As shown in Figure 5.5, using an acoustic method, such as an ADV, to measure the velocity of the particles could lead to results with spikes and unusual behaviour due to a momentary lack of seeding that influences the goodness of the measurement or some resonance effect depending on the length of the control volume with respect to the distance from the bottom of the flume. However, the aim of these kind of measurements was the macroscopic characterization of the velocity profile. As already described in detail in Section 3.2, during the ADV measurements, due to the possible influence of the presence of the instrument, the measurement of the other hydrodynamic quantities (pressure and forces over the pile) was not conducted. The numerical simulation reproduced the time series in which force and pressure measurements were carried on, when the velocimeter was not used. Therefore, the numerical time series differs from that of the experimental velocity measurement. Moreover, considering that: the paddle was not stopped before each ADV test; the presence of possible nonlinear effects; the small reflection of the dissipating beach at the end of the flume and re-reflection at the paddle due to the absence of active wave absorption at the generation could generate a not negligible disturbance inside the flume that could be responsible of the small difference between the two signals, especially for the phase drift that it is observed. However, the model reproduces very well the trend of the velocity time series and it allows a good estimation of its profile over the entire depth of the channel.

Pressure

According to Figure 3.3b, for each wave condition the test is repeated 7 times, one for each reference angle (φ), starting the test from the still water. The signal of each test water elevation has been synchronized referring to that one in correspondence of the pile ($WG5$). Furthermore, the different time series have been compared to ensure that the same wave conditions are reproduced. The results for the vertical line placed in $\varphi = 0°$ are shown in the graphs of Figure 5.6. Here, only the results of 5 pressure transducers over the 8 installed are reported. The results of pressure transducers 2, 7 and 8 respectively placed at z=16-55-60cm from the bottom are omitted. The ones which are placed above the still water level are omitted because the signal is almost zero during all the tests. Instead, the pressure transducer placed at z=16cm is not reported because it did not work properly for all the tests due to a problem of water infiltration.

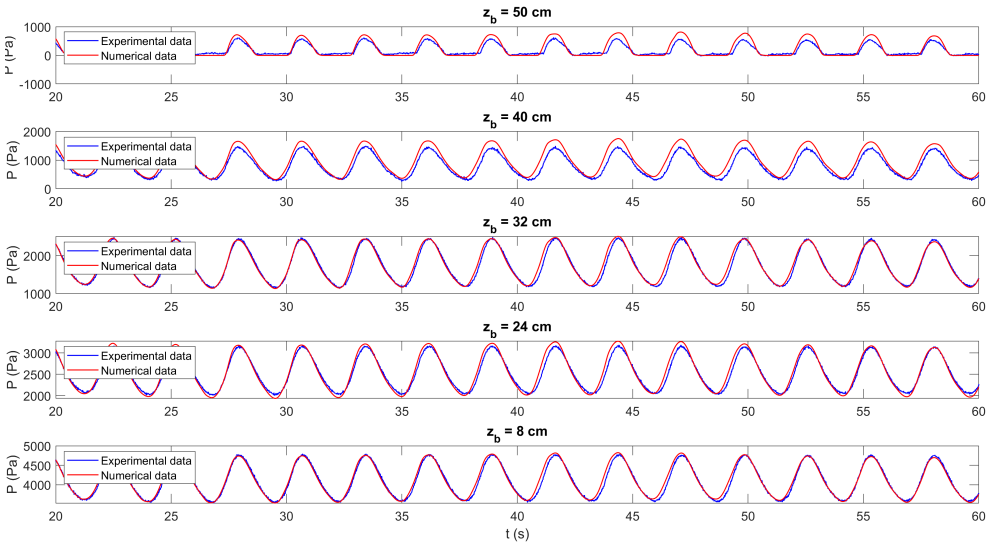

Figure 5.6: Pressure time series: comparison between experimental and numerical data for test "R15" at different depths from the bottom along the vertical line placed in correspondence of the stagnation point ($\varphi = 0°$ in Figure 3.3b)

The results of the numerical model are in a very good agreement with experimental data. The values of pressures are correctly represented both in terms of magnitude and trend under crest and trough phases. An almost perfect superposition is obtained for the pressure transducers located in the lowest part of the cylinder (until pressure transducer 4 placed in z=32cm from the bottom). In the higher part of the model, where a small difference in terms of water elevation lead to an high variation in terms of pressure, the differences are slightly larger, even in the order of 15-20% at z=50cm. In absolute terms the difference is in the order of about 200Pa, corresponding to 2cm of water column. The reason of this difference is probably due to a different reproduction of the run-up phenomenon over the surface of the pile. However, for the global representation of pressure the comparison is very good along the whole vertical line. The representation of those data, elaborated by means of the phase averaging technique described in Section 4.1.1, is summarized in Figure 5.7. Here, the comparison

in terms of vertical distribution of the total and dynamic pressure at different location and phases is reported. Here the crest (left panels) and trough (right panels) phases results of each data set is analysed even if there is not a perfect comparison of the wave phases in which they occur. The aim of this specific analysis is to evaluate the effectiveness of the model in the description of the pressure under this nonlinear wave conditions, hence the same representative phases are considered.

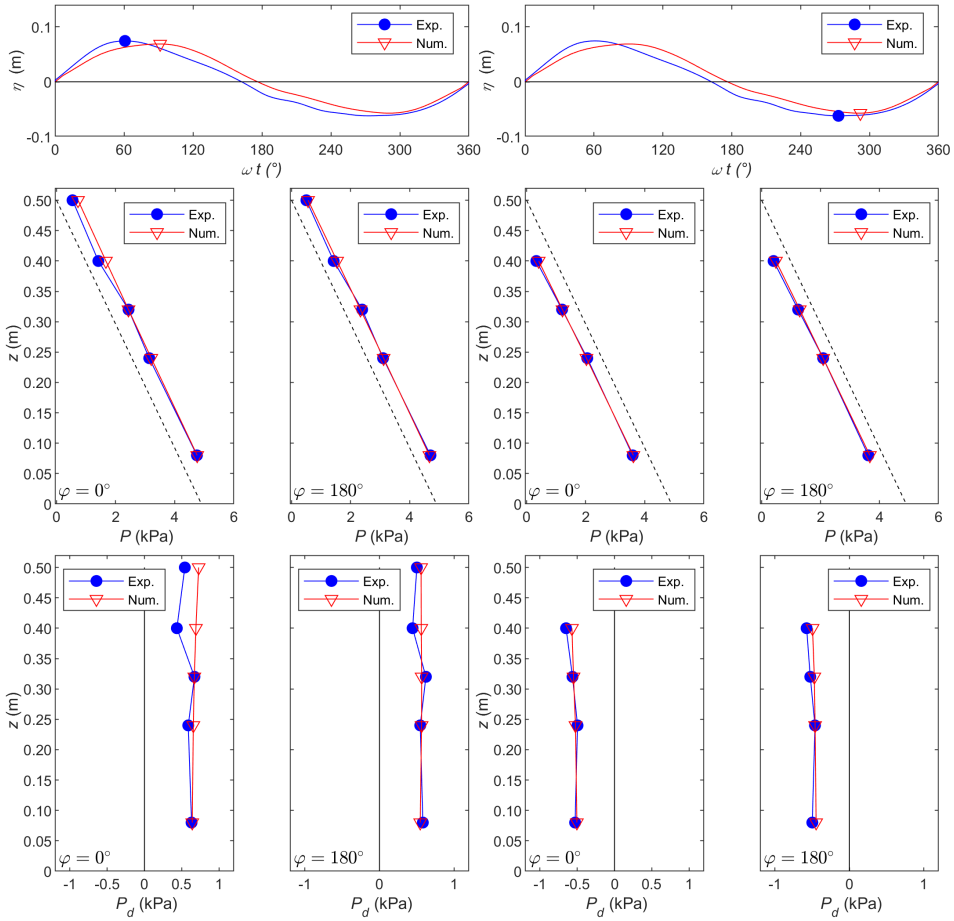

Figure 5.7: Experimental and numerical vertical distributions of the total pressure P (central panels) and of the dynamic pressure P_d (lower panels) for wave $R15$ at the crest (left panels) and at the trough (right panels) phases. Results are plotted in two different positions: in front of the pile at $\varphi = 0°$ (first and third columns) and behind it at $\varphi = 180°$ (second and fourth columns).

The panels in the central row represent the total pressure vertical distribution while the lower panels show the contribution of the dynamic pressure only. Two different position with respect to the cylinder are considered. According to Figure 3.9, the profiles are obtained in front of the pile ($\varphi = 0°$) and on the lee side ($\varphi =$

180°). The results are in good agreement especially in the analysis of the dynamic pressure which mostly depends on small variation of the hydrodynamics. The global distribution appears to be satisfactory along the vertical line even if some scatter is recorded for the pressure sensors in the higher position.

Total force

An OpenFOAM® tool has been used to directly export the total force over the surface of the cylinder in the numerical model, computed as the integral of the pressure field. In the experimental campaign, data of force are directly measured by the load cell at the top of the pile (Figure 3.3a) and, thus, elaborated according to the procedure explained in Section 3.2, Equations 3.1 to 3.4. The results of the comparison are presented in Figure 5.8.

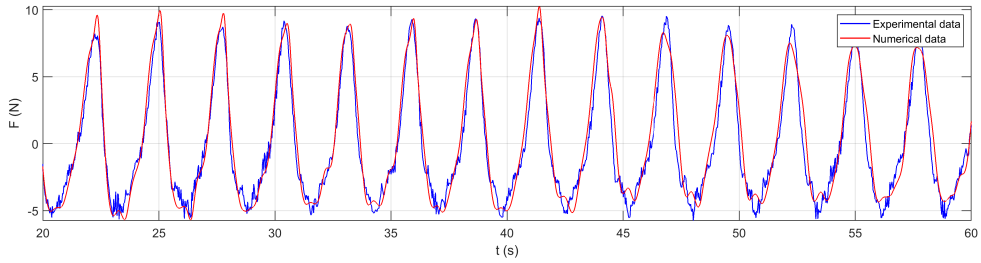

Figure 5.8: Total force time series: comparison between experimental and numerical data for test "R15"

The agreement between the two different time series is found to be very good, the model represents very well the trend of the force over the pile. Both the crest and though phases are very well reproduced.
As already seen in Section 4.1.2, the analytical approach of (Morison et al., 1950), even if widely used for the design of a marine piled structure (Det Norske Veritas, 2010), it is an empirical method which works under specific conditions and limitations depending on the characteristics of the wave (linear with a small amplitude with respect to the water depth) and of the structure (small compared to the wave length). Moreover, the results are highly influenced by drag and inertia parameters which have to be evaluated from experimental measurements (Sarpkaya, 1976; Chakrabarti, 1987). Various experimental studies with different wave and field conditions (Chen et al., 2014; Maza et al., 2015) demonstrate the importance of *CFD* numerical modelling, being an important tool to avoid high underestimation of the forces induced by nonlinear waves.

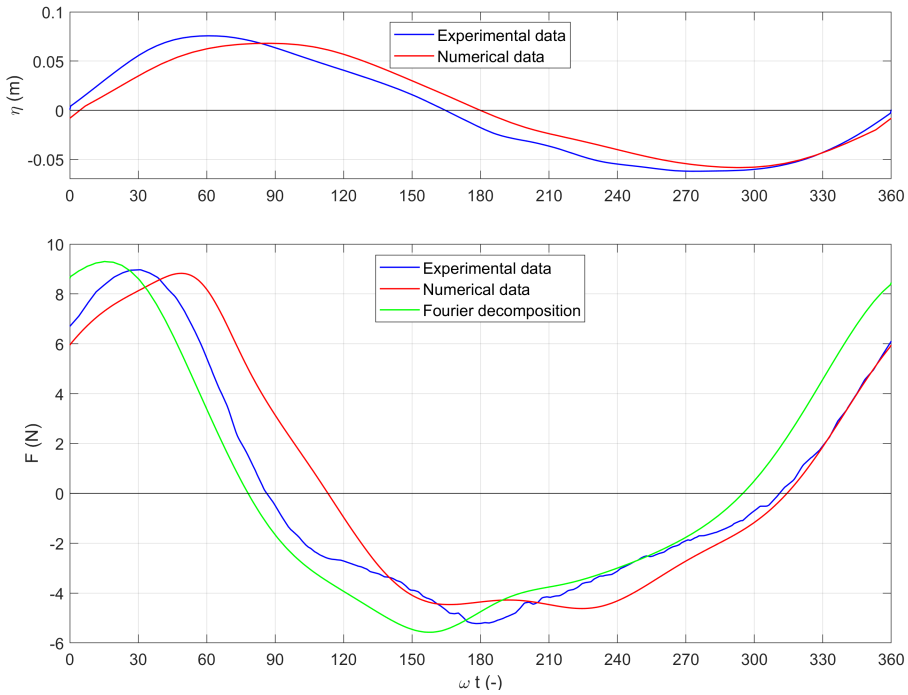

Figure 5.9: Phase averaged water level surface at $WG5$ in correspondence of the pile (upper panel) and force (lower panel): experimental data (blue), numerical data (red) and by *Fourier* decomposition approach (green) for wave test $R15$.

In Figure 5.9, the phase averaged force of the numerical model is hence compared with the corresponding results for experimental data obtained by direct measurement (blue line) and by the *Fourier* decomposition approach (green line) already shown in Figure 4.12, with the hydrodynamic coefficient taken from the literature as C_D=0.9 and C_M=2.0. Here, the water elevation for the *Fourier* decomposition method is not reported because it corresponds to the experimental one by definition (see Equation 5.6). The numerical model with the new boundary condition for the wave generation of a measured signal provides very good results. The phase averaged water elevation in correspondence of the pile (upper panel) is reproduced very well and, moreover, the total force over the pile shows a very good agreement with experimental data. Both the shape and the maximum/minimum values are very well reproduced. However, it must be noted that the more simple approach of the application of a revised *Morison* formula (Equation 2.6) with the velocity field computed by applying the linear wave theory to the spectral components of the water elevation signal, also gives very good results, as already highlighted. This method can be considered valid for a first estimation of the total force over the pile given a specific time series of $\eta(t)$.
It can be concluded that the model has been fully validated by means of different types of experimental data. Both kinematic and dynamic quantities have been used in order to obtain a very good comparison.

5.3 Comparison with experimental data

In the previous section, the validation procedure was widely performed considering the comparison with all the available measured data (water level, pressure, velocity and force) for the wave test "R15". Here, different wave conditions from Table 3.1 were analysed. In particular, three wave tests for each wave period are chosen (namely tests "R2","R5","R6","R7","R8","R9","R10", "R17", "R21", "R22", "R23", "R24", "R25" and "R27" . Among all the available wave periods (T=1.83s-2.00s-2.19s-2.35s-2.74s), three different wave heights (H from 16 to 23cm) and, thus, different values of KC from 4.7 to 10.0. As for the validation test "R15", the duration of each simulation was 60s and it took about 60h in 8 processors on a 3.6GHz machine to complete. In this section, only the results of water level in correspondence of the pile ($WG5$) and the total force acting over it are reported, as shown in Figures 5.10 to 5.23, because they are the most representative hydrodynamic quantities, among the measured ones. Here, the time series of the last 35s of simulations are reported in order to focus on the part of the test over the transition zone. Most of the results obtained with the simulations of the wave conditions selected from Table 3.1 gave a very good agreement with experimental data. The free surface elevation is very well reproduced both for longer ("R15" and "R17") and for shorter ("R6" and "R7") waves. Some small differences are noticed, especially for the crest phases, but the adaptation between the two curves can be considered very good. The goodness of the numerical model with respect to the experimental data is confirmed by the evaluation of the determination coefficient r^2, here computed as:

$$r^2 = 1 - \frac{\sum_i (y_i - f_i)^2}{\sum_i (y_i - \bar{y})^2} \tag{5.9}$$

where y_i represents the experimental value of the considered quantity (water level or force) at each time step i; f_i is the numerical value in the same moment and $\bar{y}$ is the mean value of y_i. Longer waves, with lower values of H/L are perfectly reproduced by the numerical model both in terms of water surface elevation and force over the pile. Among the different simulations, those that obtained the lowest values of r^2 are the tests with the higher ratio H/L such as waves "R22" and "R23" (Figures 5.19 and 5.20). Here, some spikes in the force measurements are recorded and the trough phase is not well represented. This effect can be probably due to the aspect ratio of the mesh. The steepness of the wave can play a primary role on the goodness of a numerical model. If the wave becomes highly peaked (due to the large ratio H/L) as in those tests, the aspect ratio should be decreased. Different authors (Jacobsen et al., 2012; Devolder et al., 2018) noted how numerical results obtained with an aspect ratio equal to 1 are significantly better compared to an aspect ratio equal to 2, especially for breaking or quasi-breaking waves. Here, in the zone far from the cylinder the aspect ratio was 2:1 which is a good value for not-breaking waves (as for the wave used for the validation of the model in Section 5.2) but it could be not enough for some cases for which the mesh should be adapted. The use of this numerical model for design purposes, hence requires an additional refinement of the mesh for such tests to improve the results increasing the r^2 value. However, the comparison with experimental data and the usefulness of the numerical model are still very good. For the tests characterized by a lower steepness (namely $H/L \lesssim 0.045$), very high values of the determination coefficient are reached ranging from the smallest obtained for wave "R10" (r^2=0.77 for water surface and r^2=0.63 for force) to the largest one for wave "R8" (r^2=0.94 for water surface and r^2=0.96 for force). The use of the determination

coefficient to perform the comparison between experimental and numerical data is not typically done in literature because it could give "small" values even when data comparison seems to be good (e.g. when a small phase drift between the two signal occurs and because of the zero-crossing phases). However, in this case, the goodness of fitting is confirmed by the large values of r^2 that have been obtained in most of the cases.

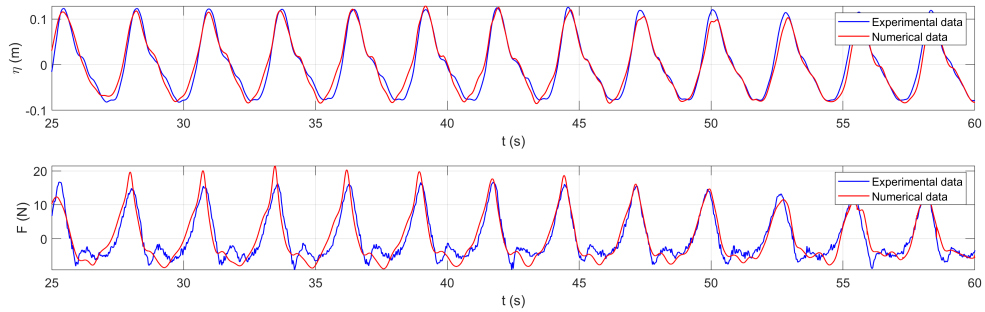

Figure 5.10: Comparison between experimental and numerical data for test "R2": water elevation (upper panel; r^2=0.96) and total force (lower panel; r^2=0.87) time series

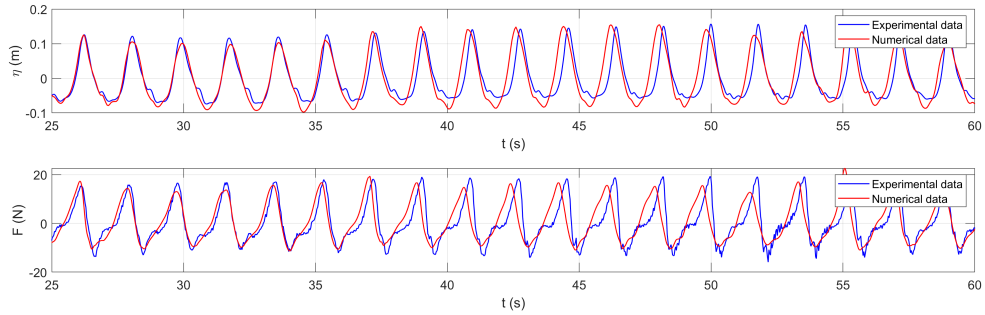

Figure 5.11: Comparison between experimental and numerical data for test "R5": water elevation (upper panel; r^2=0.67) and total force (lower panel; r^2=0.56) time series

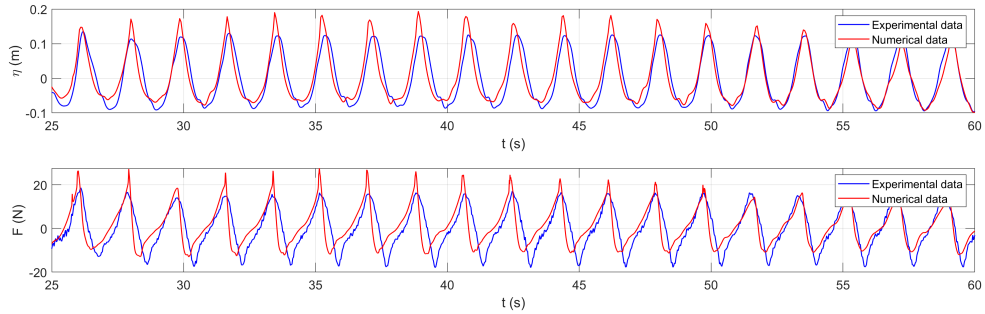

Figure 5.12: Comparison between experimental and numerical data for test "R6": water elevation (upper panel; r^2=0.91) and total force (lower panel; r^2=0.77) time series

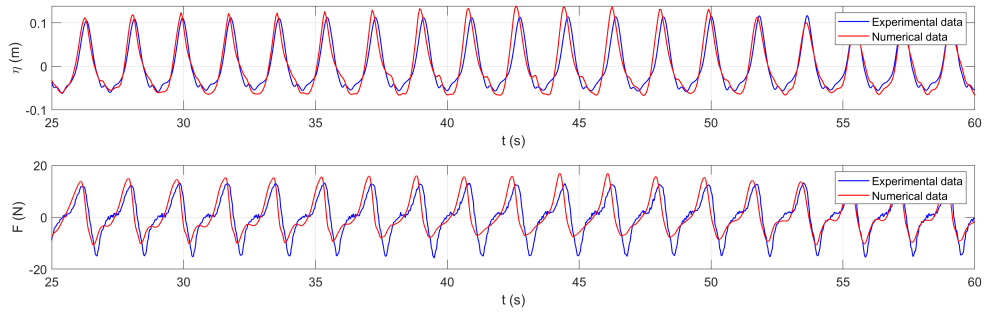

Figure 5.13: Comparison between experimental and numerical data for test "R7": water elevation (upper panel; r^2=0.86) and total force (lower panel; r^2=0.70) time series

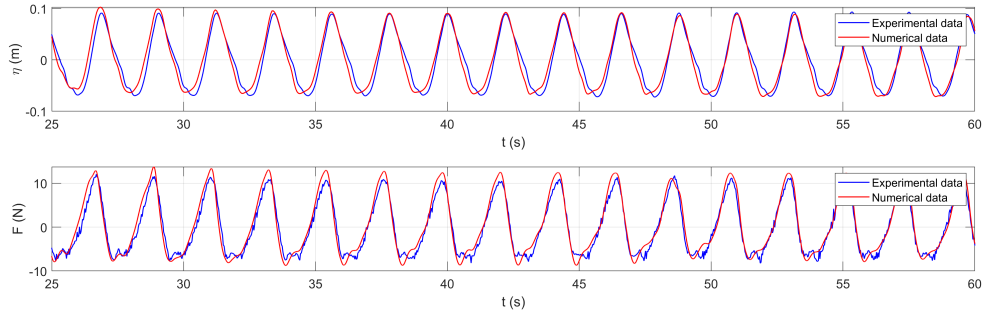

Figure 5.14: Comparison between experimental and numerical data for test "R8": water elevation (upper panel; r^2=0.94) and total force (lower panel; r^2=0.96) time series

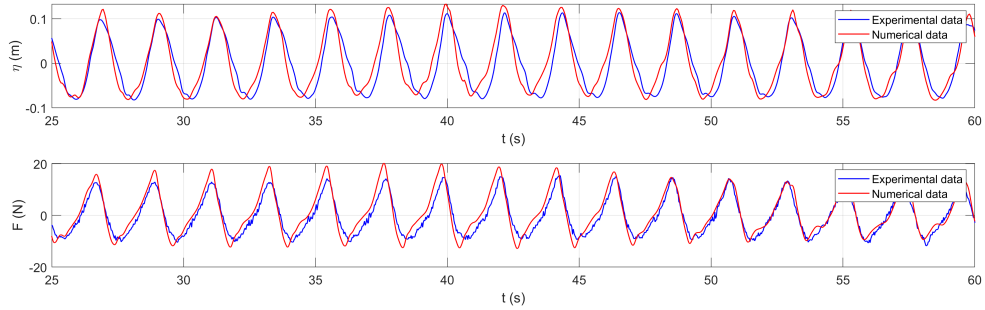

Figure 5.15: Comparison between experimental and numerical data for test "R9": water elevation (upper panel; r^2=0.89) and total force (lower panel; r^2=0.92) time series

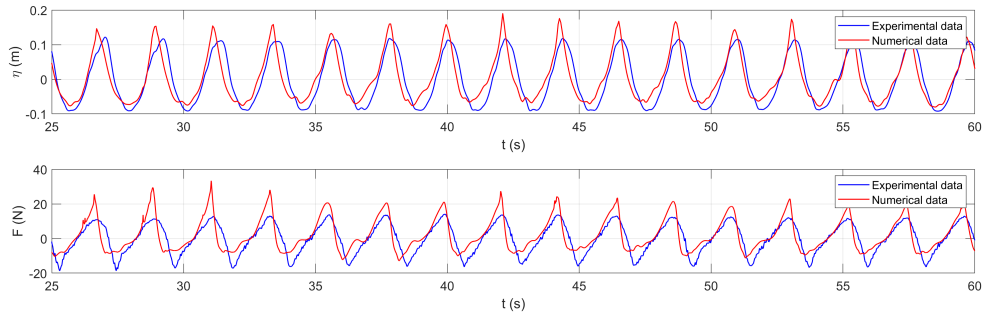

Figure 5.16: Comparison between experimental and numerical data for test "R10": water elevation (upper panel; r^2=0.77) and total force (lower panel; r^2=0.63) time series

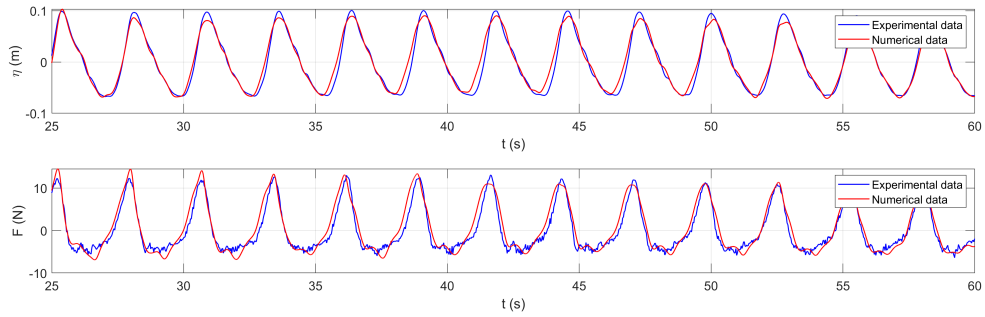

Figure 5.17: Comparison between experimental and numerical data for test "R17": water elevation (upper panel; r^2=0.97) and total force (lower panel; r^2=0.92) time series

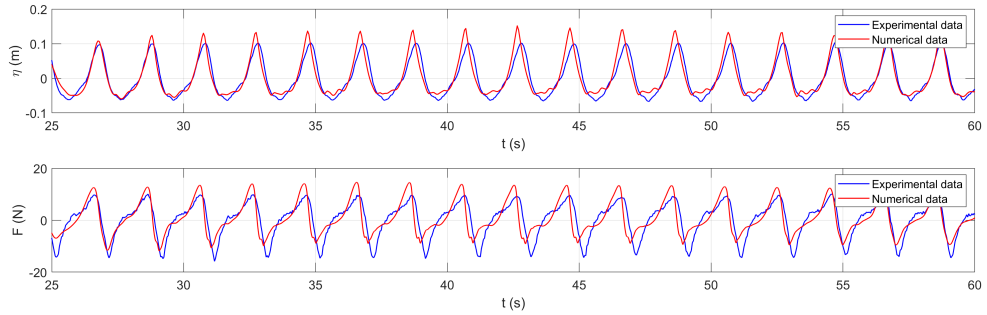

Figure 5.18: Comparison between experimental and numerical data for test "R21": water elevation (upper panel; r^2=0.91) and total force (lower panel; r^2=0.78) time series

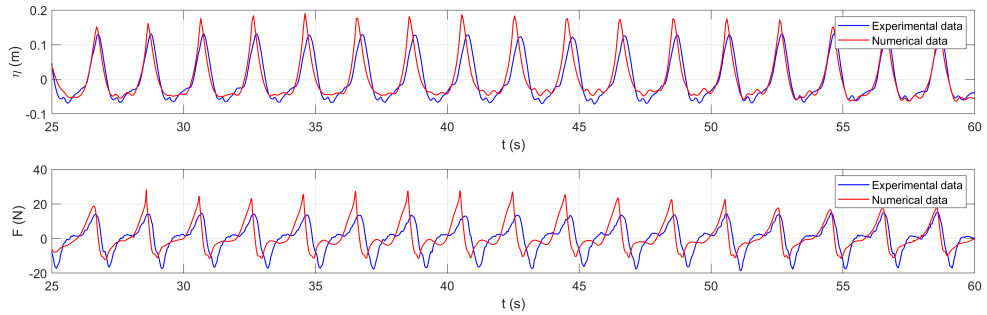

Figure 5.19: Comparison between experimental and numerical data for test "R22": water elevation (upper panel; r^2=0.85) and total force (lower panel; r^2=0.47) time series

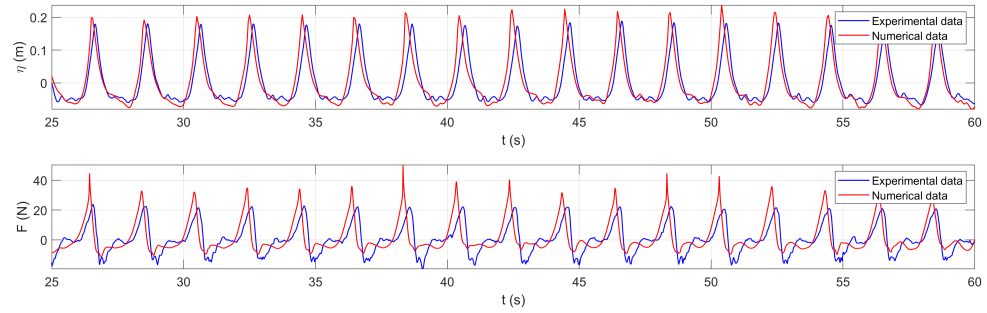

Figure 5.20: Comparison between experimental and numerical data for test "R23": water elevation (upper panel; r^2=0.67) and total force (lower panel; r^2=0.30) time series

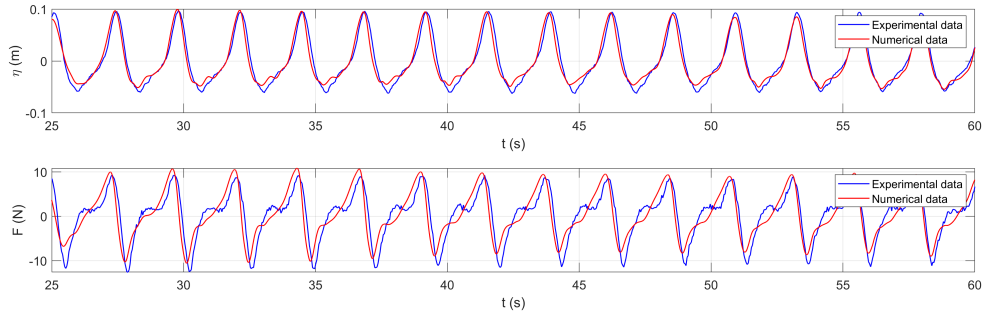

Figure 5.21: Comparison between experimental and numerical data for test "R24": water elevation (upper panel; r^2=0.96) and total force (lower panel; r^2=0.81) time series

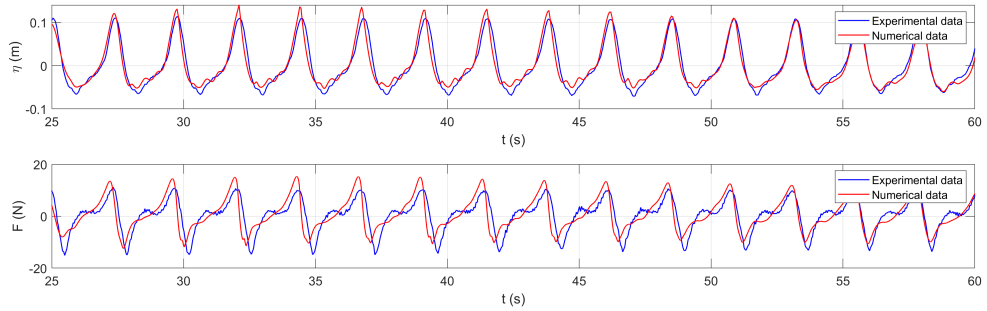

Figure 5.22: Comparison between experimental and numerical data for test "R25": water elevation (upper panel; r^2=0.95) and total force (lower panel; r^2=0.79) time series

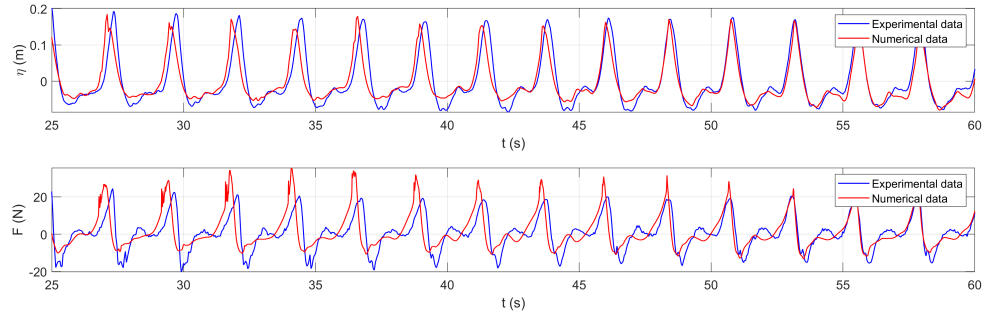

Figure 5.23: Comparison between experimental and numerical data for test "R27": water elevation (upper panel; r^2=0.90) and total force (lower panel; r^2=0.64) time series

The numerical model made with OpenFOAM® allows to obtain a very good evaluation of the total force over the pile, taking into account the nonlinearities of the regular waves that have been decomposed into their spectral components by performing a *Fourier* analysis. The water level surface on the lateral side of the pile and the

wave force over it are very well reproduced and, thus, the model is valid for further analysis.

5.4 Numerical results

The number of validated numerical data gave the possibility to perform analysis which are not so easy to do experimentally as, for example, the measurement of run-up along the surface of the cylinder or the evaluation of vortex generation, development and growth.

5.4.1 Run-up

A good estimation of wave run-up over a cylinder is a primary task in the design of a platform or a wind turbine foundation. The wrong evaluation of the run-up could lead to the wrong positioning of the entrance platform that could not be accessible under severe wave conditions. On the other side, building the platforms on a higher level would bring other problems, such as safety problems, due to the high distance from the boat and thus additional intermediate platforms must be designed. Lara et al. (2013) showed that OpenFOAM® is a very good tool for the evaluation of wave run-up over piled structures.
In the present section, the evaluation of run-up for each wave condition has been made by means of the phase averaging technique presented in Section 4.1.1 once the data can be considered in the steady part of the wave train. The incident wave height is obtained by the control line placed in correspondence of the pile ($WG5$ in Figure 5.1) while the run-up level along the pile is computed by the analysis of the values α_1 on its surface. An example of the result for two wave conditions with different time periods ($R7$ with T=1.83s and $R8$ with T=2.19s) are shown in Figure 5.24

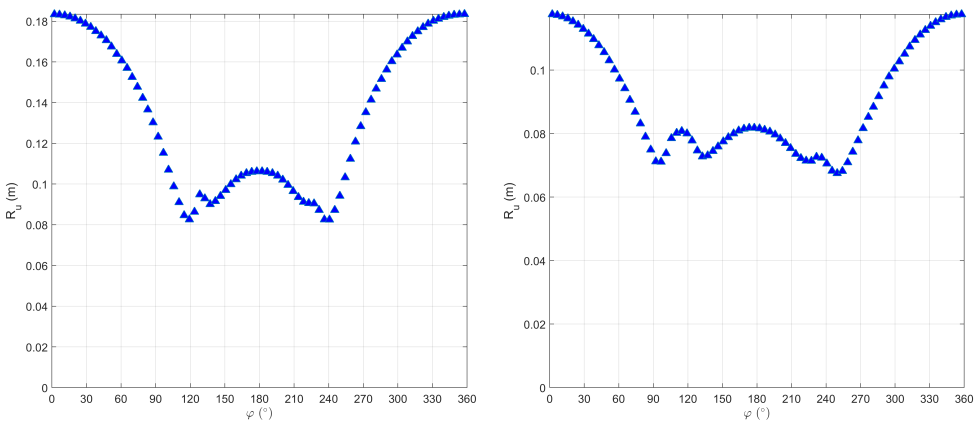

(a) (b)

Figure 5.24: Phase averaged run-up along the surface of pile for wave $R7$ (a) and $R8$ (b) obtained with the numerical model.

Here, on the abscissa the angular coordinate φ described in Figure 3.9 is reported, on the ordinate the phase averaged value of run-up (R_u) along the surface is reported.

In each test of Figure 5.24, two peak values are obtained, one at the stagnation point (φ=0°) and the other one at the back of the cylinder (φ=180°). Points where the run-up is minimum are on the side part of the cylinder, where $\varphi \approx$120°-240°. This specific pattern is also confirmed by previous experimental and numerical works (Mohseni et al., 2018). The incident wave, reaches the stagnation point and is divided into two waves (edge waves) that move along the surface of the cylinder at both sides. When such waves reach the back of the pile ($\varphi \approx$180°), a notable amount of water merges, thus leading an asymmetric pattern. This phenomenon is highly nonlinear and it is one of the cause of wave scattering. The visual results obtained for the numerical simulation of test $R8$ are reported in Figures 5.25 and 5.26. Here, the positive elevation phases of the wave from the up-crossing to the down-crossing are displayed. In particular, the upper panel in each figure represents the water level at the control point placed in correspondence of the wave gauge on the side of the pile ($WG5$), the middle panels show the planar view of the free surface while the lower panels show the three-dimensional interaction between the wave and the pile. Note that in those figures the free surface is contoured with the ratio between the η value of each point of the free surface ($\eta(x, y) = z(x, y) - h$) with the crest height of the wave (η_{max}). The lower limit of the colormap has been set to $\eta/\eta_{max} = -0.40$ to highlight the differences of the phases with positive elevation. Moreover, the values around the zero are displayed as a white coloured band in order to highlight the position of the up-crossing.

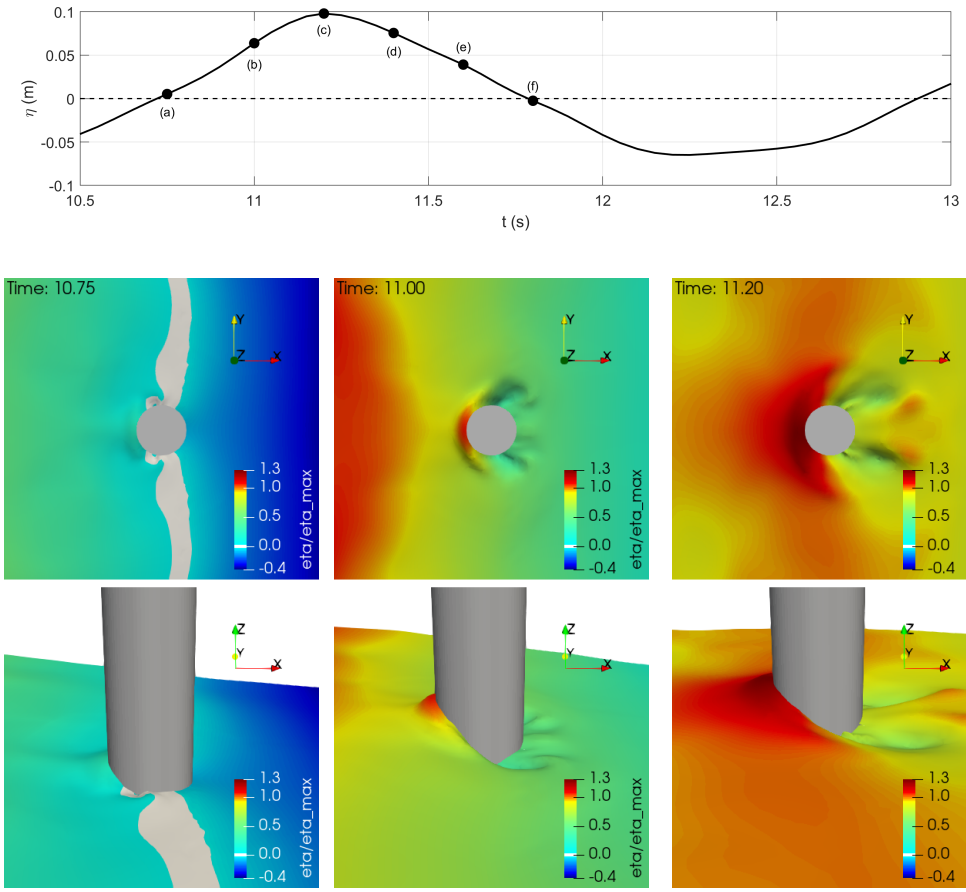

(a) (b) (c)

Figure 5.25: Free surface elevation contour around the cylinder, wave $R8$ (T=2.19s, H=0.16m) at $t = 10.75s$ (up-crossing - panels a), $t = 11.00s$ (rising phase - panels b), $t = 11.20s$ (crest phase - panels c). Colormap η/η_{max}.

When the incident wave is no-breaking, the wave impact is not so high but, due to the interaction between the high velocities and the cylinder, the run-up is very large (Swan and Sheikh, 2015). The quantity of water in front of the pile starts to accumulate at the up-crossing (Figure 5.25a), grows up (Figure 5.25b) and reach its maximum volume in correspondence of the crest (Figure 5.25c). Moreover, during these phases, two edge waves are generated and start propagating along the surface of the cylinder in downstream direction (lower panels of Figure 5.25). After the crest phase, the water level in front of the pile runs down and washes back, mainly at upstream direction (Figures 5.26d-e) until the flow is completely reversed at the up-crossing (Figure 5.26f). In Figure 5.26e the edge waves reach the position opposite to the stagnation point (φ=180°), they collide one into the other and the amount of volume of water that they carried out originates, on the back of the pile, the second run-up peak showed in Figure 5.24 which has a lower value compared to the first one.

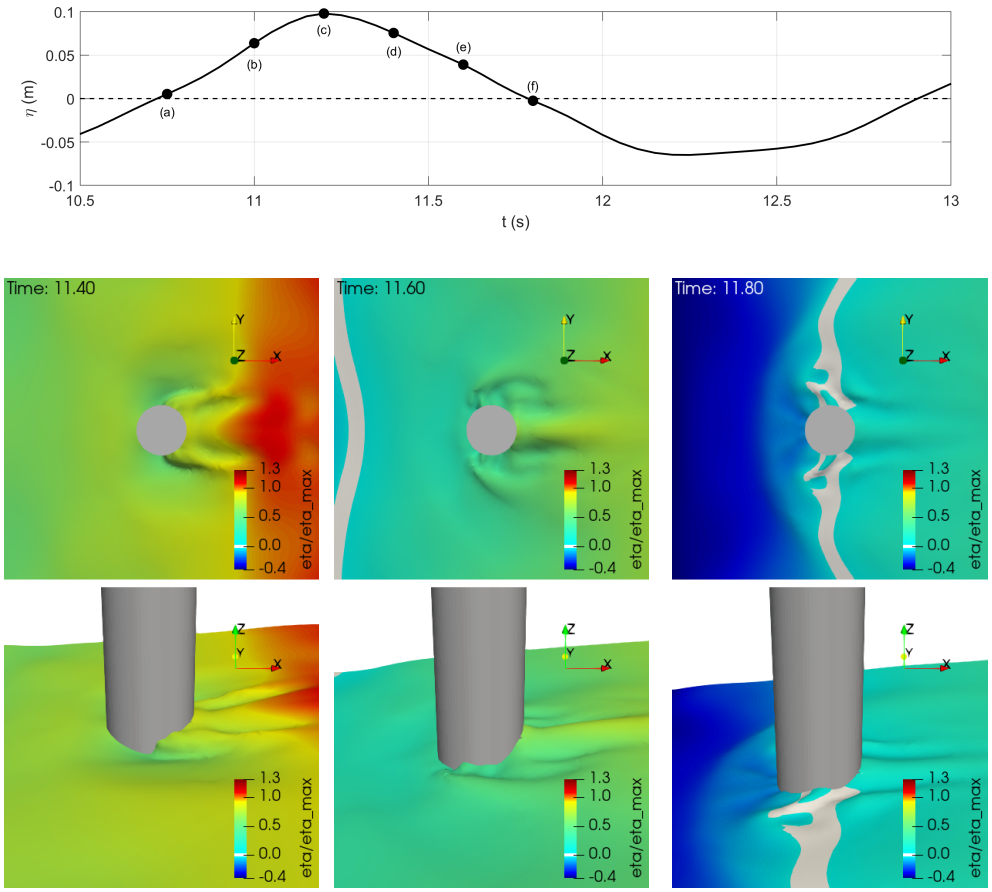

(d) (e) (f)

Figure 5.26: Free surface elevation contour around the cylinder, wave $R8$ (T=2.19s, H=0.16m) at $t = 11.40s$ (descending phase - panels d), $t = 11.60s$ (descending phase - panels e), $t = 11.80s$ (down-crossing - panels f). Colormap η/η_{max}.

This phenomenon involves different complicated features such as breaking, air entrainment, and turbulence, so the available prediction methods result inadequate and some effective tool is needed as a support of the design process. For steep waves, the motion is highly nonlinear, therefore the linear theory is not appropriate for predicting wave run-up accurately and it could lead to a significant underestimation of the crest elevation (Niedzwecki and Huston, 1992; Kriebel, 1992). Therefore, second-order and higher-order effects must be taken into account. Physical experimentation is one of the most common approaches for studying wave-structure interaction. The experiments of Kriebel (1990, 1992) for regular wave run-up on a circular cylinder in water of finite depth have subsequently been compared with a number of wave run-up calculation procedures.
In the literature, several formulations have been proposed to estimate the maximum run-up over the surface of a vertical cylinder. Hallermeier (1976) suggests an estimation of run-up depending on the maximum elevation of the crest (η_{max}) which is increased thanks to the contribution of the velocity stagnation head. The particles are forced to move upward because of the presence of the pile, thus, the kinetic energy

of the particles is transformed into potential energy (Equation 5.10).

$$R_u = \eta_{max} + \frac{U^2}{2g} \tag{5.10}$$

where u is the water particle velocity at the still water level. The experimental small-scales study of Niedzwecki and Duggal (1992) used the linear theory to calculate the kinematics and found out that Equation 5.10 under predict the maximum run-up value. The formulation of Hallermeier (1976) is changed to:

$$R_u = \frac{H}{2} + 6.83\frac{U^2}{2g} \tag{5.11}$$

in which H is the undisturbed incident wave height. In another paper, Niedzwecki and Huston (1992) introduced a second coefficient to the wave height to obtain a better fit of the data:

$$R_u = 0.56H + 6.52\frac{U^2}{2g} \tag{5.12}$$

It must be highlighted that in these experimental campaigns the linear theory has been used to evaluate the velocity of the particle in correspondence of the still water level. As already seen in Figure 4.2, using the linear theory to evaluate the kinematics of nonlinear waves could lead to a wrong estimation of the values. In more recent studies (Kazeminezhad and Etemad-Shahidi, 2015; Bonakdar et al., 2016), small scale tests were performed to obtain other run-up formulas based on dimensionless parameters such as H/h, H/L and D/L.
The results of the application of Equations 5.10-5.12 to the wave tests simulated numerically are reported in Figure 5.27.

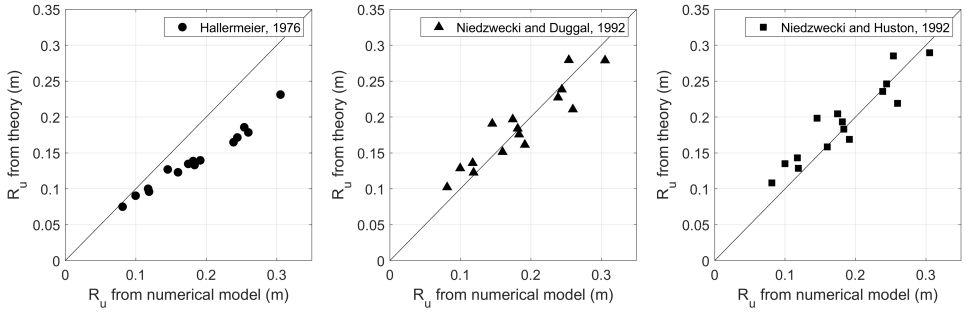

Figure 5.27: Comparison between run-up obtained from the numerical model and theories: Hallermeier (1976) - circles (r^2=0.36); Niedzwecki and Duggal (1992) - triangles (r^2=0.85); Niedzwecki and Huston (1992) - squares (r^2=0.84).

As already noted by different authors (Martin et al., 2001; De Vos et al., 2007), most theories give a bad estimation of the run-up values, in particular the velocity stagnation head approach of Hallermeier (1976) gives an underestimation while the semi-empirical method of Niedzwecki and Huston (1992) overestimates the run-up in nearly all cases. The results of our analysis (Figure 5.28) mostly confirm the limits of this approach. In particular, Equation 5.10 (Hallermeier, 1976) lead to values of run-up which are significantly lower than the measured up to the limit case of wave $R6$ where the value predicted from the theory with η and u from the numerical

model is about 30% lower than the measured one (r^2=0.36). The semi-empirical approaches gives almost the same results (Equation 5.11 - r^2=0.85; Equation 5.12 - r^2=0.84). The coefficient of determination is higher with respect to the previous analysed formula and, moreover, in this situation a slight overestimation of the run-up values is obtained, which is good for design purposes. However, it must be noted that in the studies of Niedzwecki and Huston (1992); Niedzwecki and Duggal (1992), no measurements of wave velocity are carried out and the results are highly dependent on the wave theory which is chosen for its computation. The main advantage of numerical modelling is the possibility to extract from the numerical domain every kind of informations (depending only on the computational costs in terms of time or storage memory). A well calibrated model, as in this case, allows to extract data such as velocity measurements, and consider them trustworthy. According to this, in Equations 5.10 to 5.12 the coefficient of the kinetic component (here defined m) is fitted with numerical data in order to find the best correlation (Figure 5.28).

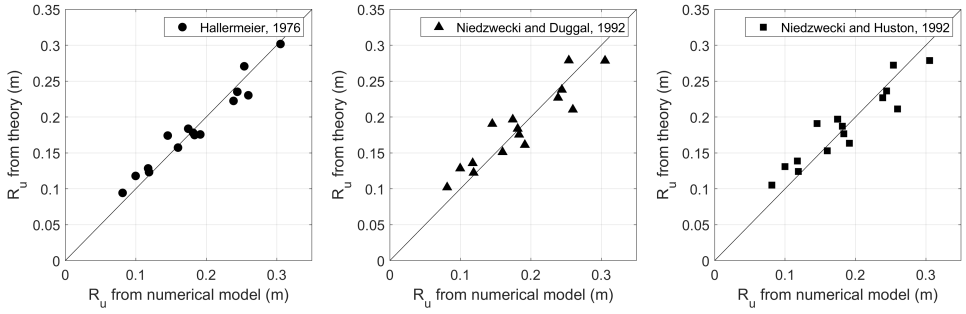

Figure 5.28: Comparison between run-up obtained from the numerical model and theories with fitted velocity coefficient m: Hallermeier (1976) - circles (m=4.47 and r^2=0.94); Niedzwecki and Duggal (1992) - triangles (m=6.81 and r^2=0.85); Niedzwecki and Huston (1992) - squares (m=5.98 and r^2=0.85).

All the approaches with modified coefficients give a very good agreement with experimental data (r^2 always larger than 0.85). The best fit approach on Equations 5.11 and 5.12 did not change significantly the coefficients. The coefficient m in Niedzwecki and Duggal (1992) changed slightly from 6.83 to 6.81 and in Niedzwecki and Huston (1992) from 6.52 to 5.98 and, thus, also the regression coefficient remained almost the same. The results are, hence, well represented by those formulas and their validity is confirmed. However, the modified approach of Hallermeier (1976) with $m = 4.47$ leads to a better adaptation to the numerical data. The poor agreement (r^2=0.36) obtained with Equation 5.10 with $m = 1$ increased considerably up to the large regression coefficient r^2=0.94. Therefore, the new equation for run-up calculation based on validated numerical data becomes:

$$R_u = \eta_{max} + 4.47\frac{u^2}{2g} \tag{5.13}$$

Among the three approaches, Equation 5.13 is the one that better represents the data. It is based on the Hallermeier (1976) approach that, differently from the others here reported, considers the value of η_{max} and not the total wave height H as a first term and, hence, it implicitly takes into account that the shape of the wave could be not linear and symmetric as it happens for the *Airy* theory.

5.4.2 Vortex generation

Eulerian coherent structure criteria for vortex identification are typically formulated in terms of the invariants of the velocity gradient tensor $\boldsymbol{\nabla U}$. The *Q-criterion*, developed by Hunt et al. (1988), locates regions where rotation dominates strain in the flow. Letting $\boldsymbol{S}$ and $\boldsymbol{\Omega}$ denote the symmetric and antisymmetric parts of $\boldsymbol{\nabla U}$, Q is defined as the second invariant of $\boldsymbol{\nabla U}$, that, for incompressible flow, corresponds to:

$$Q = \frac{1}{2}(||\boldsymbol{\Omega}||^2 - ||\boldsymbol{S}||^2) \tag{5.14}$$

where $||\cdot||$ is the Euclidean matrix norm. A coherent vortex is defined as a region where $Q > 0$. Q represents the local balance between shear strain rate ($(\boldsymbol{S})$ and vorticity tensor ($\boldsymbol{\Omega}$) intensity, identifying vortices as elliptic areas where the vorticity is larger than the rate of strain (Kolar, 2007). The $Q > 0$ criterion states that a vortex can be defined as a connected fluid region where the second invariant of the velocity gradient tensor is positive.

It is well known that to completely achieve the exact description of vortical structures, the problem must be solved in all of its length and time scales by means of *Direct Numerical Simulations*. However, the computational costs are prohibitive for a simulation at high Reynolds numbers and, thus, in order to simplify the numerical approaches, one is naturally led to the *Large Eddy Simulations*, which represents less computational effort at the cost of introducing some modelling in the sub-grid scales. Nevertheless, the costs for a full and correct *LES* for high Reynolds numbers is still comparable to *DNS*. However, several authors (Ong et al., 2009; Rosetti et al., 2012), due to the limited computational costs (time of simulation and storage space) made analysis on vortex shedding with *RANS* equations with different turbulence models ($\kappa - \epsilon$ and $\kappa - \omega SST$). It appears that this approach is able to produce the vortex-shedding motion and to qualitatively individuate the vortices.

A similar analysis with a *RANS* model was performed by Baykal et al. (2017). Here the formation of horseshoe vortex and lee-wake vortex is analysed for both steady current or oscillatory flow conditions. The back-filling process is also taken into account with that morphodynamic model. Differently from that work, in this thesis the analysis is carried out in rigid bed conditions with real measured wave as an input. Baykal et al. (2017) highlighted how, using a *RANS* approach, the coherent structures can be significantly damped or smoothed (because of the large eddy viscosity used); however, differently from that study, here the new stabilized version of the $\kappa - \omega SST$ closure model proposed by Larsen and Fuhrman (2018) has been used in order to avoid an over-prediction of the turbulence levels.

To better visualize the vortical structure, the results of wave condition $R2$ of Table 3.1 are analysed. In particular, in Figure 5.29, four time steps are shown corresponding to the characteristics phases of a wave cycle: panel "a" corresponds to the reversal of the flow close to the up-crossing, panel "b" represents the crest phase, panel "c" shows the other reversal of the flow (before the down-crossing) and panel "d" refers to the trough phase. For each significant phase, the figure shows: the free surface around the pile with the associated iso-contour of Q under it for the three-dimensional vortex representation; the vorticity contour computed according to Equation 4.14 and the *Q-criterion* contour computed according to Equation 5.14 at a horizontal plane close to the bottom of the flume ($z_b = 1cm$). The instants in which the flow is reversed are referred to the bottom of the flume (panels "a"-"c") instead of at the free surface because they are more representative for the vortex generation process at the bottom.

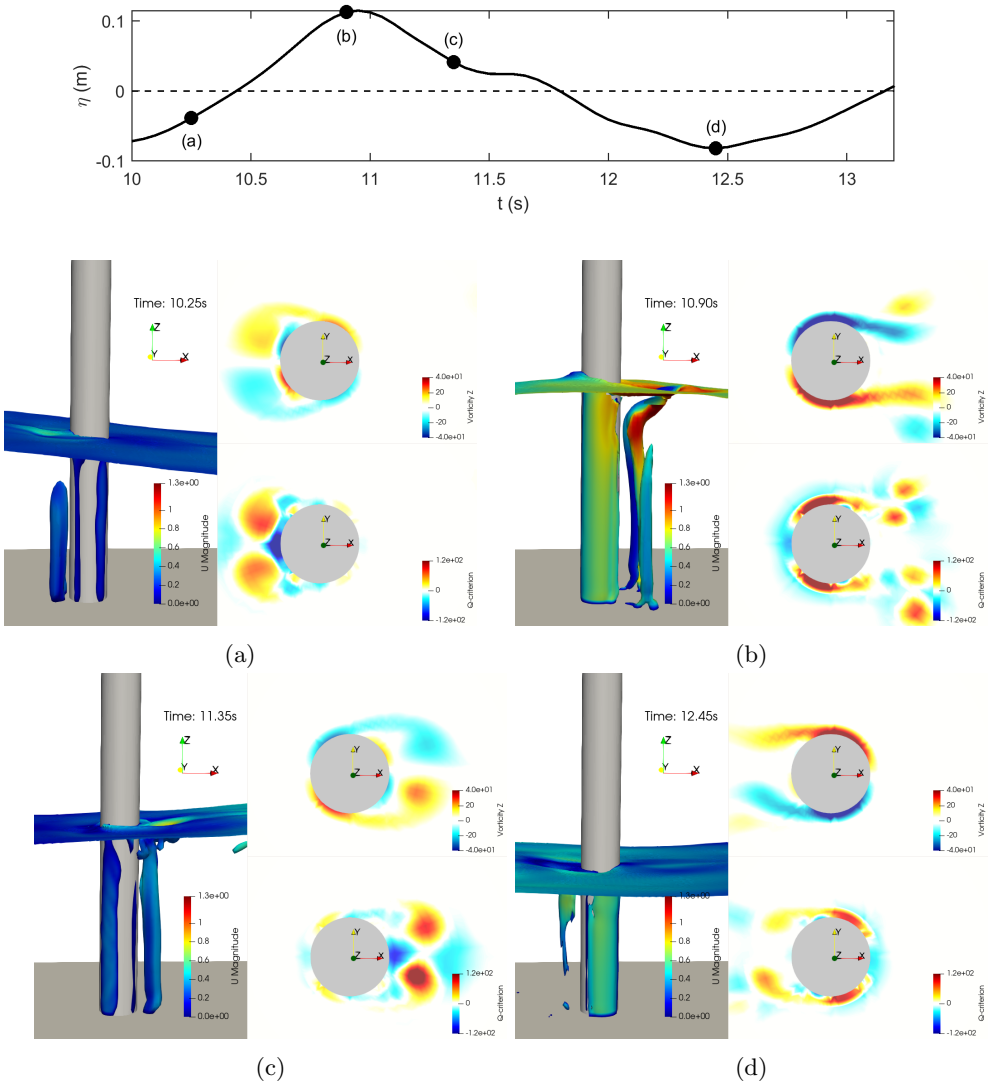

Figure 5.29: Vortex pattern identification of wave $R2$ around the cylinder at different times: (a) at the reversal of the flow close to the up-crossing, (b) at the crest phase, (c) at the reversal of the flow close to the down-crossing, (d) at the trough phase. In each panel it is plotted the free surface and the iso-contour of the *Q-criterion* ($Q = 80$) coloured by velocity magnitude (left), the vorticity contour (top-right) and the $Q - criterion$ contour (bottom-right) at the plane z_b=1cm.

Considering all the limitation of the application of a *RANS* model for the vortex pattern identification, the results obtained in Figure 5.29 are very interesting. When the horizontal velocity is approximately zero, (panels "a" and "c") the vortex visualization on the front of the pile (due to the reversed flow) is very clear; two symmetrical structures are generated and then, when the velocity becomes positive (x direction), they are carried on with the flow on the lateral side of the pile. At the same time, a large vorticity is generated in front of the pile (panel "b") possibly due to the presence of horseshoe vortex as highlighted also by Baykal et al. (2017) in which the

presence of such vortices was more evident due to the higher value of KC (KC=20). From the *Q-criterion* contour of Figure 5.29b, it is evident how, from the rotation of the boundary layer around the cylinder, another pair of symmetrical vortices is generated. At the same time, two different pair of vortices are present (red zones), the vortices generated from the previous half cycle carried on by the reversed flow (the two external vortical structures in panel "b") and the so named lee-wake vortices generated from the rotation of the flow around the pile (internal). The "old" vortices lose intensity and they are completely transported by the flow and hence dissipated. The "new" ones, as happened in panel "a", remain in the area of influence of the pile until the reversal of the flow (panel "c") where it is possible to note that during this phase the intensity of the vortices (e.g. the intensity of Q) is higher because they are originated from the positive water elevation phases, in which the velocities are higher. This is also confirmed by the comparison between the trough phase (panel "d") with the crest phase (panel "b"). During the crest, the presence of vortical structures is more evident both in front and behind the cylinder with respect to the phase in which the velocity in the negative direction is maximum.
It must be noted that this specific analysed time interval is in the initial part of the simulation, one of the first waves after the numerical ramp time of 5s. Here, even if the symmetry with respect to the *x-axis* is evident, it seems that this hydrodynamic condition represents an upper limit of the symmetrical flow. The vortical structures are similar on both sides of the cylinder but their intensity is very different (see the ω and Q contour) especially during the phase in which the lee wake vortices are more visible (panel "c"). Higher values are obtained on the side of the pile in which $y < 0$. This small difference, wave after wave, increases up to a point in which the symmetry is broken and an alternate detachment of vortices occurs. This phenomenon was expected for this specific wave condition (KC=10.0). As already highlighted by Sumer et al. (1997) and reported in Section 2.1, for $6 < KC < 17$ the symmetry breaks up, vortex shedding occurs with one vortex shed in each half period (see Figure 2.2c). The model reproduces adequately this phenomenon as it can be seen in Figure 5.30 where the results in terms of Q at close time steps are displayed in order to better understand the process of generation and growth of the vortices and their path. As in the previous plot, the red zones ($Q > 0$) represent the areas in which the coherent vortex is identified and, because the main topics of this thesis is the study of the interaction between fluid phase and structure in the nearbed, the plots are extracted close to the bottom of the flume (z_b=1cm).

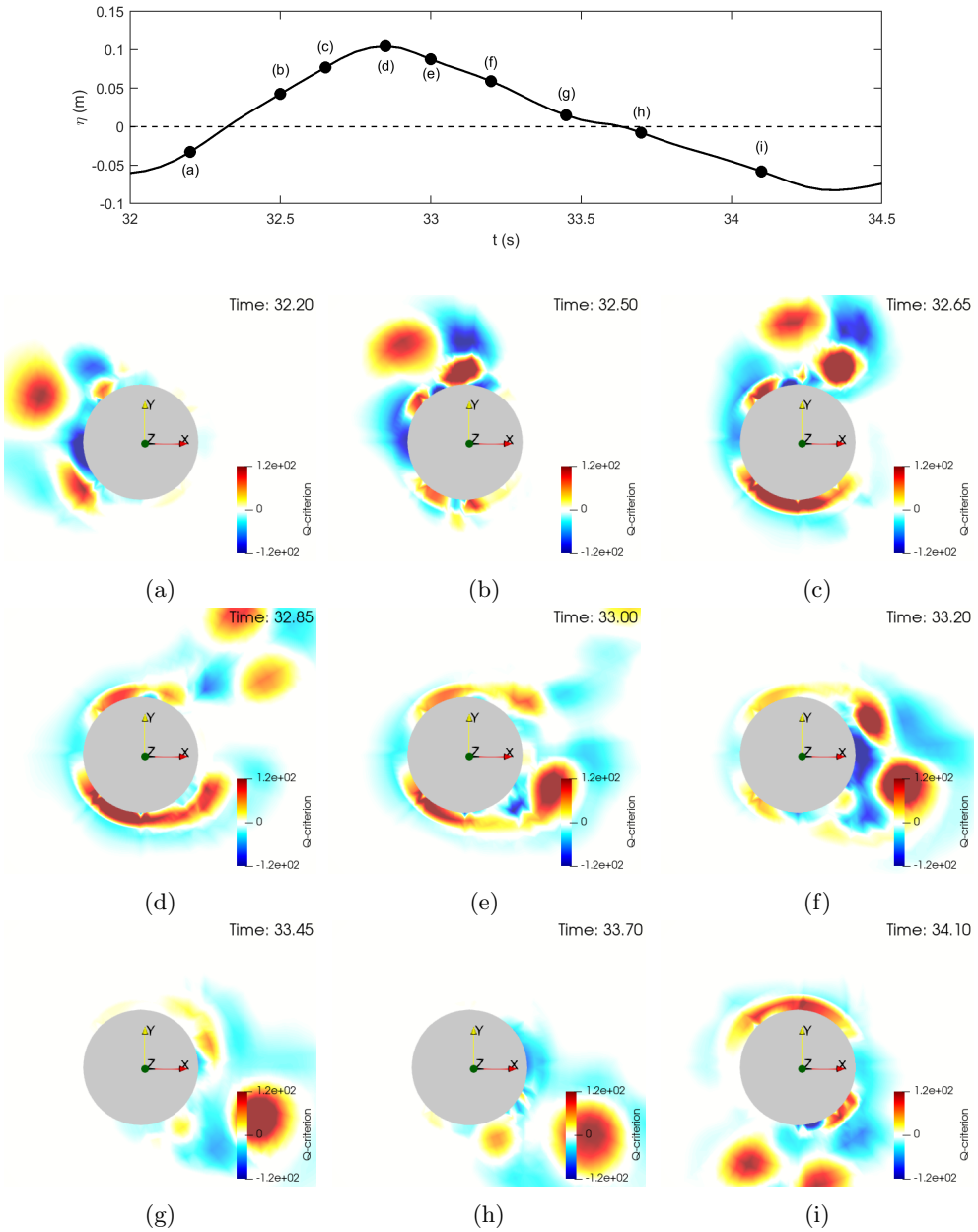

Figure 5.30: Vortex pattern identification of wave $R2$ around the cylinder at different times after the symmetry breaks up: $Q - criterion$ contour at the plane z_b=1cm.

The analysis of Figure 5.30 confirms the vortex generation theory presented in Sumer et al. (1997). After the first phase in which the stream around the pile was symmetric (Figure 5.29), the symmetry breaks up and the vortices start to shed alternatively. Moreover, having representations of closer time steps, it is more easy to visualize and understand the double pair vortices behaviour described above. The vortex in front of the pile in panel "a", which is the wake vortex of the backflow, after the up-crossing is carried by the flow along the x direction. Moreover, due to the

generation of another vortex close to it (that will be the lee-wake vortex), it is also pushed laterally up to completely get away from the area of influence of the cylinder (b-c-d). In this case, but not for all the wave, also the new vortex completely detaches from the pile during the crest phase being removed by the flow (in Figure 5.30d it can be seen the two vortices moving away). At this point, the horizontal velocity is still positive and the vortex generation process lead to the creation of two more wake vortices on both sides (panels "e"-"f"). Those vortices are completely asymmetric both for dimension and intensity in agreement with Figure 2.2. After the reversal of the flow (panel "g") the smaller vortex is destroyed and the bigger one is carried backward from the reversed flow. In this case it moves upstream from the same side where it came from ($y < 0$) but in some case it has been observed (both in the numerical model and by PTV experimental analysis) that a vortical structure originated on one side, after being detached, comes back on the other side, rolling completely around the cylinder.
As already reported in Section 4.3, the same wave condition has been analysed experimentally with the PTV technique and the comparison between the most relevant phases is shown in Figure 5.31. Here, the phase averaged experimental results are compared with the numerical ones obtained for a specific wave, within the whole time series, that shows a good correspondence with the first one (upper panel). In particular, two wave phases are analysed (crest phase: panels "a"; reversal of the flow: panels "b"). The numerical results show the contour of the *Q-criterion* (central panels) as already done in Figure 5.30. According to Figure 4.39, the experimental data are plotted in terms of contour of the OW parameter (lower panels) for the same wave phases.

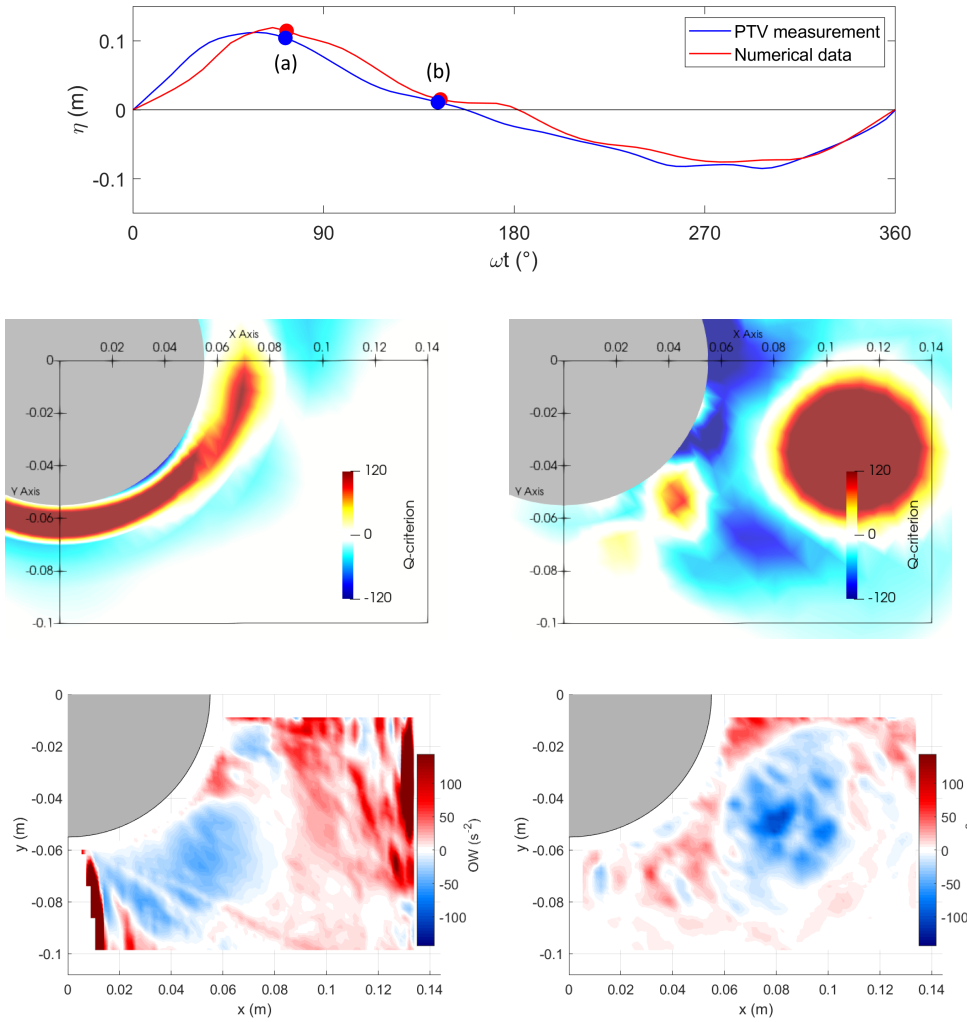

(a) (b)

Figure 5.31: Vortex pattern identification for wave $R2$. Numerical data (central panels): contour of the *Q-criterion* at z_b=1cm. Experimental data (lower panels): contour of the OW at z_b=4.6cm. Results obtained for the crest phase (panels a) and at the reversal of the flow (panels b)

The results are in substantial agreement even they are not exactly representing the same phenomenon. The results in the PTV section are phase averaged, hence they are obtained considered the whole time series. On the contrary, the central panels of Figure 5.30 represent a specific time step. Moreover, in the numerical model a horizontal plane at z_b=1cm is analysed in order to have informations on the vortical structures at the bottom of the flume. In the experimental set-up it was not possible to investigate that plane due to the problem of allocating the camera below the flume and because of its focal length (the lower measured plane is situated at z_b=4.6cm). The aim of this analysis is not only the comparison between experimental and numerical data but also to improve the knowledge of the phenomenon and, therefore,

the horizontal plane in such position has been chosen as the most significant.
However, taking into account this difference, the comparison can be done between the two data sets. Under the crest phase (Figure 5.31a) the same vortical structure can be recognized as the red coloured vortex in the numerical model that corresponds to the blue vortex on PTV campaign. Both the representations show that the detachment point is located at about $\varphi = 135°$ and the shape of the vortex, considering that the experimental results show an evident disturbance zone at $\varphi \approx 90°$, is very similar. However, the thickness of these vorticity dominated zones appears to be higher in experimental results. After the passage of the crest, the phase in which the vortex is more visible corresponds to the reversal of the flow (Figure 5.31b). The correspondence is very good, the vortex is completely detached from the cylinder and it is located at about $\varphi = 150°$. The size of the vortex appears to be very similar ($\approx 0.6D$) and, moreover, even the distance from the pile at which it occurs is well represented. In the experimental analysis it is located slightly closer to the structure with respect to the numerical model possibly due to the differences between the two methods of elaborations.
In Figure 5.32 the comparison between the experimental and numerical dynamic pressure distribution around the pile at the plane z_b=0.08m is reported for the analysed wave $R2$. Here, the small difference between the two datasets is due to the small difference in terms of water elevation at the same wave phase (see Figure 5.32c in which the water elevation is almost the same and, thus, even the magnitude of the pressure corresponds).

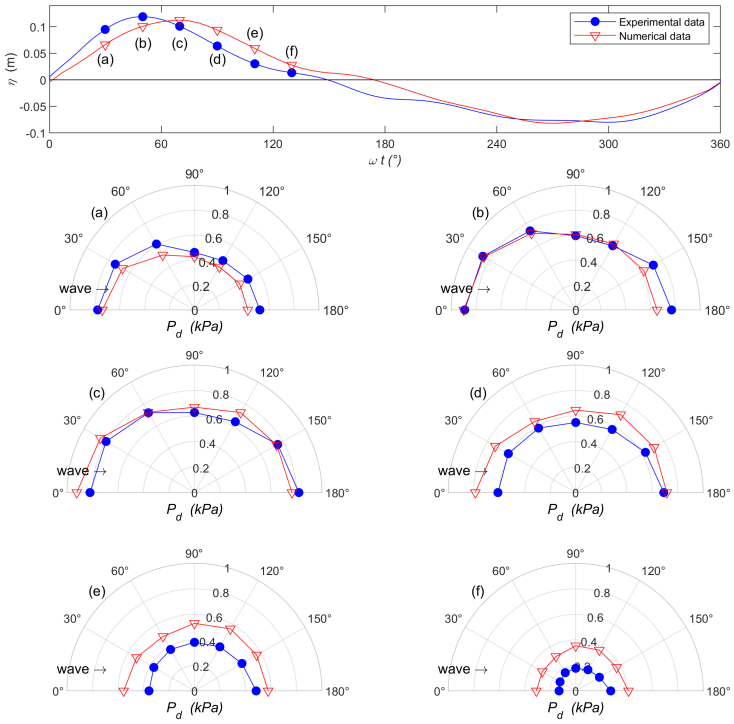

Figure 5.32: Phase averaged water elevation of wave $R2$ and plan view (xy-plane at z_b=0.08m) of the dynamic pressure P_d, for different wave phases: $\omega t = 30°$ (a); $\omega t = 50°$ (b); $\omega t = 70°$ (c); $\omega t = 90°$ (d); $\omega t = 110°$ (e); $\omega t = 130°$ (f). Experimental (blue lines with circles) and numerical data (red lines with triangles).

The results of the experimental data (blue lines) are similar to those obtained for wave $R15$ previously discussed in Section 4.1.3. During the analysed positive elevation phases, the pressure is always higher in front of the pile, hence originating a positive force. A favourable pressure gradient (negative value) is observed around the pile during the rising phases (panel "a"). The pressure gradient switch to positive and increases in intensity at the back of the pile during the crest phase (panels "b"-"c"). In particular, in panel "c" the maximum positive gradient, when vortex shedding is supposed to occur, is found in the zone $\varphi = 120° - 150°$. This is in agreement with the corresponding contour map of *Okubo-Weiss* or vorticity (Figure 4.39b) in which the vortex seems to detach exactly in that zone. When the intensity of the flow decreases (panels "d"-"e"-"f"), the magnitude of the dynamic pressure is lower. In this phase, the vortical structure is completely detached from the pile (Figure 4.39d) and hence, no effects are expected on the pressure distribution along the x-axis that became symmetric (the total force approaches to zero at the down-crossing).
Similar considerations can be done for the numerical results. As in the experimental case, a negative pressure gradient is obtained in the range $\varphi = 0° - 90°$ during phases $\omega t = 30° - 50°$. On the contrary, here the maximum positive gradient is less evident but it occurs again during the maximum elevation phase (panel "c") but, differently from the previous situation, in a different position ($\varphi = 90° - 120°$). However, this is coherent with the corresponding results concerning the vortex visualization at the crest phase by means of the *Q-criterion* (Figure 5.31a). Here, the vortical struc-

ture appears to exactly detach in the zone individuated by the pressure distribution analysis at the corresponding wave phase.

5.5 Discussion on the numerical results

A numerical model with the open source tool OpenFOAM® has been realised. As for the experimental data, the numerical results can contribute to the comprehension of a complex 3D physical phenomenon induced by the wave-structure interaction. In particular, the numerical data allows to analyse in a more complete way such interaction, being the flow highly three-dimensional. Indeed, the 3D physical phenomenon of the run-up around the cylinder or the vortical structures generation, development and detachment can be fully studied.
As a novelty aspect, in agreement with the good results obtained for the force estimation in the experimental model, a new boundary condition for the wave generation is added to the numerical code. It consists in the generation of a measured water elevation signal and the corresponding velocity profile is computed by means of the same *Fourier* decomposition approach used in Sections 4.1.1 and 4.1.2. With this boundary condition, a nonlinear wave time series corresponding to a specific wave condition ($R15$) is generated and the excellent comparison with all the available experimental data (water elevation, pressure, velocity and force) confirmed the goodness of such approach. The model is hence validated with the water elevation and force time series of other experimental tests and the results are very good as also confirmed by the high values obtained for r^2. Once the model is validated, further analysis are performed.
The interaction of the water surface with the pile is studied and the phase averaged run-up along the circumference of the pile is computed. From this results, in addition to some images that help the visual representation of the phenomenon, the interaction of the wave with the cylinder is analysed. In particular, in the stagnation point an amount of water is observed under the crest phase. After this phase, two edge waves are generated on the lateral side of the pile and they merge each other on the back of the pile originating a second peak on the run-up distribution at $\varphi = 180°$. The analysis is completed with the study of the maximum values in comparison with some formulas available in the literature. In particular, an adaptation of the equation proposed by Hallermeier (1976) gave very good results on the run-up estimation ($r^2 = 0.94$). It is noted how, among the reported formulas, the one that gives the best result is the only one that does not depend on the total wave height but on the crest height (taking into account implicitly the nonlinearity of the wave). An accurate estimate of the run-up on the structure is fundamental in the design of the position of the access facility to the structure that must be placed at a higher level.
The generation of coherent structures is analysed in terms of vorticity and by means of the *Q-criterion* for the most intense wave condition ($R2$). As it also happened in experimental tests, after a certain number of waves the symmetry of the flow breaks up as also highlighted by Sumer et al. (1997) for this specific wave conditions ($KC > 10$). Moreover, it is also observed that if the vortex does not have enough intensity to completely move away from the area of influence of the pile, when the flow reversal occurs, it changes its direction and it finally detaches on the other side of the pile, in addition to the new generated vortex, until it is completely dissipated. The detailed analysis of the vortical structures (performed for the wave phases corresponding to the positive water surface displacement) allowed to obtain useful information linked to the scour

pattern. The results are also in agreement with those of the PTV campaign of Section 4.3; both the phase, size and position of vortices are well represented. The effect of the vortex generation is also observed in the analysis of the pressure gradients around the pile that, as for the experimental results, show positive (adverse) values in the zone $\varphi = 120° - 150°$ when vortex shedding occurs.
The main results of the numerical model allowed to improve the understanding of the complex relation between pressure gradients, vortical structures generation and associated scour patterns. Moreover, the adaptation of an existing relation for the evaluation of the maximum run-up is obtained with a significant number of numerical data but it needs to be validated by experimental data in order to be considered suitable for design purposes.

Chapter 6

Conclusions

The aim of this thesis is to improve the knowledge on the dynamical and morphological processes induced by nonlinear regular and random waves on vertical cylinders. In particular, the correct design of such structures depends on some aspects that still present a certain degree of uncertainties. This thesis provided a critical analysis and upgrade of the methods generally used in the design of a piled marine structure. Moreover, the present thesis allowed to extend the knowledge on the physical phenomenon of the vortical structure generation and development related to the scour process.

The first aspect studied in this work is the accurate evaluation of the force acting on the pile due to wave action only. From the analysis of the pressure over the surface of the pile, an asymmetric pressure distribution between the front and the wake region of the pile is observed, thus producing a total force on it. The maximum force occurs during the rising of the positive water surface elevation ($\omega t > 0°$) and before the wave crest phase ($\omega t \approx 60°$). Such result suggests that both the drag and inertial components of the total force are important. Usually the *Morison* approach is applied for the evaluation of the total force under non-breaking waves (Det Norske Veritas, 2010). However, in this study we pointed out that this approach highly depends on the choice of the wave theory for the calculation of the orbital velocity that can lead to a large underestimation of the peak values in the case of real waves which are characterized by nonlinear behaviour. In order to consider the effects of the nonlinearity of the waves, here, a *Fourier* decomposition approach has been used to compute the velocity profiles of regular waves. This approach consists in the realization of the spectral decomposition of the free surface elevation signal into components with different amplitudes and phases. Therefore, the velocity profile is reconstructed applying the *Airy* theory and summing each component effect. Finally, the total force is computed as a sum of a drag component and an inertia component with the hydrodynamic coefficients obtained from the literature. The comparison between the computed and experimental phase-averaged forces is very good. The shape of the force phase evolution is very well reproduced as long as the peak values. Both the phase and the maximum values are well estimated and only in few cases a small overestimation ($\approx 20\%$) is observed. The recommended practice (Det Norske Veritas, 2010) about wave induced loads on slender members suggests to use more exact theory for the total force evaluation. The results obtained with this approach give a conservative and accurate evaluation of the total force from the water elevation signal. On the contrary, when the linear theory is applied for the computation of the kinematics related

to the force (*Morison* equation), the phase in which the maximum force occurs is not well reproduced and mostly the maximum force values are underestimated almost for all the wave conditions. Therefore, the use of the *Fourier* decomposition approach for the force computation can be considered a very good solution for design purposes. Another important objective of this thesis was the evaluation of the scour, due to regular and random waves, that is one of the most important cause of failure of structures in the marine environment. The experimental data of this thesis confirmed the results of the empirical relation of Equation 4.2 even if in this study we highlighted that it is not easy to evaluate exactly the maximum scour value due to the presence of ripples and to the backfilling process in the live bed condition. Although several formulas have been provided in the last years (Zanke et al., 2011; Dey et al., 2011; Farooq and Ghumman, 2019), the equation of Sumer et al. (1992) is proved to be that one that better represents the scour under regular waves. However, a small correction of such formula is reported adding our data set to the existing one. Indeed, in our observations the scour process starts for values of $KC \approx 4$ slightly lower than those reported in literature ($KC \approx 6$) possibly due to the fact that the analysed waves presented a large nonlinearity. This finding influences the design of a scour protection system because the structure have to be protected also for weaker wave conditions. In addition, in order to take into account the nonlinearity of the waves, a relation for the scour prediction depending on the *Ur* parameter is here presented. However, further experiments are needed to be validated. For random waves, the equation of Sumer et al. (1992) did not give good results. The evaluation of the scour process has been made by making use of the method proposed by Ong et al. (2013) that depends on the cumulative distribution of the crest heights. The results are very good but, due to the high complexity of the method, a simplified approach has been here proposed. The *Keulegan-Carpenter* number is calculated according to Equation 4.12 in spite of Equation 3.6. The results obtained with this modified approach are almost equivalent to the original one but its applications can be considered easier and more suitable for design purposes. However, the present approach need further verifications due to the limited number of random wave tests.

The analysis of the pressure gradients, in addition to the results of the PTV experiments, allowed to better explain the generation, growth and detachment of vortices under regular waves. The wave phases and positions in which the maximum values of the pressure gradients occur, correspond to those in which the detachment of vortices is observed. The individuation of vortical structures has been done with the computation of the vorticity and *Okubo-Weiss* fields. The results of Figures 4.39 to 4.45 are able to explain the complex scour patterns obtained with the mobile bed model. The vortices characterised by a high intensity are able to catch the sediments, put them in suspension and, once they lose energy, to release them in different positions with respect to their original ones, thus leading to a deposit zone, usually located at $\varphi = 135°$. Within the range of the analysed values of KC under only wave action, the lee-wake vortex is confirmed to be the main responsible of the scour.

The numerical simulations performed with the open source tool OpenFOAM® allowed to contribute to the comprehension of the complex hydrodynamics induced by the wave-structure interaction in rigid bed conditions. In particular, the numerical data allows to analyse in a more complete way such interaction, being the flow highly three-dimensional. A new wave generation boundary condition has been added to the numerical model in order to perfectly generate an experimental water elevation signal in the fluid domain. The same *Fourier* decomposition method used in experimental tests has been applied for the computation of the input velocities at the boundary of

the numerical model. A nonlinear wave time series can be generated and the comparison with the available experimental data is excellent. The estimation of the maximum value of run-up is fundamental for the design of the position of the access facility of the piled structure (e.g. monopile wind turbine). The analysis of the maximum values lead to an adaptation of the equation proposed by Hallermeier (1976) that gave very good results on the run-up estimation depending on the crest height.
The study of the three dimensional vortical structures generation process for an intense wave condition has been done by means of the analysis of the vorticity field and of the *Q-criterion*. As also observed by other authors (Sumer et al., 1997), the symmetry of the flow around the pile is broken after a certain number of waves when $KC \geq 10$. The numerical results showed that, in some instances, a vortex generated during the first half of the period can remain in the area of influence of the pile. After the reversal of the flow, it changes the direction according to the stream until it is finally removed on the opposite side of the pile with respect to where it was generated. The detailed analysis of the positive elevation phases is in agreement with the results of the PTV campaign of Section 4.3, in which both the phase, size and position of vortices are well represented.
In conclusion, the results obtained from the experimental campaign allowed to extend the comprehension of the scour process and to give useful information for the design (force and maximum scour estimation) of a cylindrical structure under regular and random nonlinear waves. Those results, in conjunction with those from the numerical model, improved the understanding of the complex relation between pressure gradients, the vortex generation/development and the associated scour patterns. Moreover, a simple relation for the evaluation of the maximum run-up is proposed.
The main objectives of the present thesis have been achieved. However, future works are needed to validate some of the results obtained with this work that have a still limited dataset (e.g. the proposed method for random waves, the relation between S/D and Ur for regular waves and the formula for the estimation of the run-up). Moreover, piled structures in coastal environments are also built by means of a group of piles in different arrangements. The validated numerical model can be used to evaluate the effect of the pile array configurations on the wave loading over them. In particular, the effect of a group of waves focused in different positions will be studied. In addition, deeper analysis can be performed for the determination of the hydrodynamic coefficients to be used in the evaluation of the drag and inertia force components because of their high relevance on the determination of the total force. Finally, the efficiency of innovative protection systems, such as *Geotextile Sand Containers*, is going to be studied under breaking or non-breaking waves.

References

Ayoubloo, M. K., Etemad-Shahidi, A., and Mahjoobi, J. (2010). Evaluation of regular wave scour around a circular pile using data mining approaches. *Applied Ocean Research*, 32(1):34–39.

Baker, C. J. (1979). The laminar horseshoe vortex. *J. Fluid Mech.*, 95(2):347–367.

Barthel, V., Mansard, E. P. D., Sand, S. E., and Vis, F. C. (1983). Group bounded long waves in physical models. *Ocean Engineering*, 10(4):261–294.

Baykal, C., Sumer, B. M., Fuhrman, D. R., Jacobsen, N. G., and Fredsøe, J. (2017). Numerical simulation of scour and backfilling processes around a circular pile in waves. *Coastal Engineering*, 122:87–107.

Berberovic, E., van Hinsberg, N. P., Jakirlic, S., Roisman, I. V., and Tropea, C. (2009). Drop impact onto a liquid layer of finite thickness: dynamics of the cavity evolution. *Physical Review*, E 79.

Bijiker, E. W. and de Bruyn, C. A. (1988). Erosion around a pile due to current and breaking waves. *Proc. 21st Coast. Eng. Conference*, 21:1368–1381.

Boccotti, P., Arena, F., Fiamma, V., and Barbaro, G. (2012). Field experiment on random wave forces acting on vertical cylinders. *Probabilistic Engineering Mechanics*, 28:39–51.

Bonakdar, L., Oumeraci, H., and Eteman-Shahidi, A. (2016). Run-up on vertical piles due to regular waves: small-scale model tests and prediction formulae. *Coastal Engineering*, 118:1–11.

Breusers, H. N. C., Nicollet, G., and Shen, H. W. (1977). Local scour around cylindrical piers. *Journal of hydraulic Research*, 15(3):211–252.

Cao, H. J. and Wan, D. C. (2017). Benchmark computations of wave run-up on a single cylinder and four cylinders by naoe-foam-sjtu solver. *Applied Ocean Research*, 65:327–337.

Carreiras, J., Larroudé, P., Seabra-Santos, F., and Mory, M. (2000). Wave scour around piles. *Proc. 27th Coast. Eng. Conference*, 276:1860–1870.

Cartwright, D. E. and Longuet-Higgins, M. S. (1956). The statistical distribution of the maxima of random function. *Proc. R. Soc. London, Ser. A.*, pages 212–232.

Celebi, M. S., Kim, M. H., and Beck, R. F. (1998). Fully nonlinear 3-d numerical wave tank simulation. *Journal of Ship Research*, 42:33–45.

Chakrabarti, S. K. (1980). Inline forces on fixed vertical cylinder in waves. *Journal of Waterway, Port, Coastal and Ocean Division, ASCE*, 106:145–155.

Chakrabarti, S. K. (1987). *Hydrodynamics of Offshore Structures*. Computational Mechanics Publications.

Chen, L. F., Zang, J., Hillis, A. J., Morgan, G. C. J., and Plummer, A. R. (2014). Numerical investigation of wave-structure interaction using openfoam. *Ocean Engineering*, 88:91–109.

Coastal Engineering Research Center (1984). *Shore Protection Manual*, volume II. US Army Corps of Engineers, DEPARTMENT OF THE ARMY, Waterways Experiment Station, PO Box 631, Vicksburg, Mississippi 39180.

Corvaro, S., Mancinelli, A., Brocchini, M., Seta, E., and Lorenzoni, C. (2010). On the wave damping due to permeable seabed. *Coast. Eng.*, 57:1029–1041.

Corvaro, S., Marini, F., Mancinelli, A., and Lorenzoni, C. (2018a). Scour protection around a single slender pile exposed to waves. In *Proceedings of the Coastal Engineering Conference*, volume 36.

Corvaro, S., Marini, F., Mancinelli, A., Lorenzoni, C., and Brocchini, M. (2018b). Hydro- and morpho- dynamics induced by a vertical slender pile under regular and random waves. *Journal of Waterwawy, Port, Coastal, and Ocean Engineering*, 144(6).

Corvaro, S., Seta, E., Mancinelli, A., and Brocchini, M. (2014). Flow dynamics on a porous medium. *Coast. Eng.*, 91:280–298.

Dargahi, B. (1989). Turbulent flow field around a circular cylinder. *Exps. Fluids*, 8 (1-2):1–12.

De Vos, L., Frigaard, P., and De Rouck, J. (2007). Wave run-up on cylindrical and cone shaped foundations for offshore wind turbines. *Coastal Engineering*, 54:17–29.

Dean, R. G. (1976). Methodology for evaluating suitability of wave and wave force data for determining drag and inertia coefficient. In *Proceedings of the 1st International Conference on Behaviour of Off-shore Structures*, pages 40–64, BOSS'76; Norwegian Institute of Technology, Trondheim, Norway.

Det Norske Veritas (2010). *Environmental Conditions and Environmental Loads*, volume DNV-RP-C205.

Devolder, B., Troch, P., and Rauwoens, P. (2018). Performance of a buoyancy-modified k-ω and k-ω sst turbulence model for simulating wave breaking under regular waves using openfoam. *Coastal Engineering*, 138:49–65.

Dey, S., Helkjær, A., Sumer, B. M., and Fredsøe, J. (2011). Scour at vertical piles in sand-clay mixtures under waves. *Journal of Waterway, Port, Coastal, and Ocean Engineering*, 137:324–331.

Dey, S., Sumer, B. M., and Fredsøe, J. (2006). Control of scour at vertical circular piles under waves and current. *Journal of Hydraulic Engineering*, 132:270–279.

Energia Clima 2030 (2019). Proposta di piano integrato per l'energia e il clima. Technical report, Ministero dello Sviluppo Economico, Italia.

Ettema, R. (1980). *Scour at bridge piers*. Ph.d. thesis, Auckland University, Auckland, New Zealand.

Ettema, R., Kirkil, G., and Muste, M. (2006). Similitude of large-scale turbulence in experiments on local scour at cylinders. *Journal of Hydraulic Engineering*, 132(1):33–40.

Ettema, R., Melville, B. W., and Barkdoll, B. (1998). Scale effects in pier-scour experiments. *Journal of Hydraulic Engineering*, 124 (6):639–642.

Farooq, R. and Ghumman, A. R. (2019). Impact assessment of pier shape and modifications on scouring around bridge pier. *Water*, 11:1761.

Finnegan, W. and Goggins, J. (2015). Linear irregular wave generation in a numerical wave tank. *Applied Ocean Research*, 52:188–200.

Folk, R. L. and Ward, W. C. (1957). Brazos river bar: a study in the significance of grain size parameters. *Journal of Sedimentary Petrology*, 27:3–26.

Forristall, G. Z. (2000). Wave crest distributions: Observation and second-order theory. *J. Phys. Oceanogr.*, 30:1931–1943.

Foti, E. and Blondeaux, P. (1995). Sea ripple formation: the heterogenous sediment case. *Coast. Eng.*, 25 (3-4):237–253.

Hadad, T. & Gurka, R. (2013). Effects of particle size, concentration and surface coating on turbulent flow properties obtained using piv/ptv. *Experimental Thermal and Fluid Science*, 45:203–212.

Hallermeier, R. J. (1976). Nonlinear flow of wave crests past a thin pile. *Journal of the Waterways, Harbors and Coastal Engineering Division*, 102(4):365–377.

Henriquez, M., Reniers, A. J. H. M., Ruessink, B. G., and Stivea, M. J. F. (2014). Piv measurements of the bottom boundary layer under nonlinear surface waves. *Coastal Engineering*, 94:33–46.

Higuera, P., Lara, J. L., and Losada, I. J. (2013a). Realistic wave generation and active wave absorption for navier-stokes models: Application to openfoam. *Coastal Engineering*, 71:102–118.

Higuera, P., Lara, J. L., and Losada, I. J. (2013b). Simulating coastal engineering processes with openfoam. *Coastal Engineering*, 71:119–134.

Higuera, P., Losada, I. J., and Lara, J. L. (2015). Three-dimensional numerical wave generation with moving boundaries. *Coastal Engineering*, 101:35–47.

Hunt, J. C. R., Wray, A. A., and Moin, P. (1988). Eddies, stream, and convergence zones inturbulent flows. Technical Report CTR-S88, Center for Turbulence Research Report.

Isaacson, M. (1979). *Wave-induced forces in the diffraction regime*. Mechanics of Wave-Induced Forces on Cylinders. T. L. Shaw.

Jacobsen, N. G., Fuhrman, D. R., and Fredsøe, J. (2012). A wave generation toolbox for the open-source cfd library: Openfoam®. *International Journal for Numerical Methods in Fluids*, 70:1073–1088.

Journée, J. M. J. and Massie, W. W. (2001). *Offshore Hydromechanics*. Number 12. Delft University of Technology.

Kazeminezhad, M. H. and Etemad-Shahidi, A. (2015). A new method for the prediction of wave runup on vertical piles. *Coastal Engineering*.

Kida, S. and Miura, H. (1998). Identification and analysis of vortical structures. *European Journal of Mechanics - B/Fluids*, pages 471–488.

Klopman, G. (1996). Extreme wave heights in shallow water. *Delft Hydraulics*, Report H2486.

Kobayashi, T., Saga, T., and Sekimoto, K. (1989). *Velocity measurement of three-dimensional flow around rotating parallel disks by digital image processing*, volume 85. United States: SPIE Society of Photo-Optical Instrumentation Engineers.

Kolar, V. (2007). Vortex identification: new requirements and limitations. *International Journal of Heat and Fluid Flow*, 28(4):638–652.

Kriebel, D. (1990). Nonlinear wave diffraction by the vertical circular cylinder. part 1: diffraction theory. *Ocean Engineering*, 17:345–377.

Kriebel, D. (1992). Non-linear wave interaction with a vertical circular cylinder. part ii: wave run-up. *Ocean Engineering*, 19(1):75–79.

Lara, J. L., Higuera, P., Guanche, R., and Losada, I. J. (2013). Wave interaction with piled structures. application with ih-foam. In *Proceedings of the ASME 2013 32nd International Conference on Ocean, Offshore and Arctic Engineering (OMAE)*, Nantes, France.

Larsen, B. E. and Fuhrman, D. R. (2018). On the over-production of turbulence beneath surface waves in reynolds-averaged navier-stokes models. *Journal of Fluid Mechanics*, 853:419–460.

Le Méhauté, B. (1976). *An introduction to hydrodynamics and water waves*. Springer Study Edition.

Lewis, G. S., Cantwell, B. J., and Lecuona, A. (1987). The use of particle tracking to obtain planar velocity measurements in an unsteady laminar diffusion flame. In *Western States Section of the Combustion Institute spring meeting*, Provo, UT, USA.

Lin, C. and Huang, J. (2004). Decomposition of incident and reflected higher harmonic waves using four wave gauges. *Coastal Engineering*, 55:395–406.

Lin, Z., Pokrajac, D., Guo, Y., Jeng, D.-G., Tang, T., Rey, N., Zheng, J., and Zhang, J. (2017). Investigation of nonlinear wave-induced seabed response around monopile foundation. *Coastal Engineering*, 121:197–211.

Lucas, B. D. and Kanade, T. (1981). An iterative image registration technique with an application to stereo vision (jcai). In *Proceedings of the 7th International Joint Conference on Artificial Intelligence (IJCAI '81)*, pages 121–130.

Manes, C. and Brocchini, M. (2015). Local scour around structures and the phenomenology of turbulence. *J. Fluid Mech.*, 779:309–324.

Martin, A. J., Easson, W. J., and Bruce, T. (2001). Run-up on columns in steep, deep water regular waves. *Journal of Waterway, Port, Coastal and Ocean Engineering*, 127(1):26–32.

Masselink, G. and Short, A. D. (1993). The effect of tide range on beach morphodynamics and morphology: A conceptual beach model. *Journal of Coastal Research*, 9:785–800.

Matutano, C., Negro, V., López-Gutiérrez, J. S., and Esteban, M. D. (2013). Scour prediction and scour protections in offshore wind farms. *Renew Energy*, 57(3):358–365.

Mayer, S. and Madsen, P. A. (2000). Simulations of breaking waves in the surf zone using a navier-stokes solver. In *25th Conference of Coastal Engineering*, pages 928–941.

Maza, M., Lara, J. L., and Losada, I. J. (2015). Tsunami wave interaction with mangrove forests: A 3-d numerical approach. *Coastal Engineering*, 98:33–54.

Melville, B. W. (1984). Live-bed scour at bridge piers. *Journal of Hydraulic Engineering, A.S.C.E.*, 110(9):1234–1247.

Melville, B. W. and Coleman, S. E. (2000). *Bridge Scour*. Water Resources Publications, LLC.

Menter, F. (1994). Two-equation eddy viscosity turbulence models for eingineering applications. *AIAA Journal*, 32(8):1598–1605.

Miozzi, M. (2004). Particle image velocimetry using feature tracking and delaunay tessellation. In *Proceeding of the XII International Symposium on application of laser technique to fluid mechanics*, Lisbon.

Miozzi, M., Corvaro, S., Pereira, F. A., and Brocchini, M. (2019). Wave-induced morphodynamics and sediment transport around a slender vertical cylinder. *Advances in Water Resources*, 129:263–280.

Miozzi, M., Postacchini, M., Corvaro, S., and Brocchini, M. (2015). Whole-wavelength description of a wave boundary layer over permeable wall. *Exps. Fluids*, 56:127.

Mohseni, M., Esperanca, P. T., and Sphaier, S. H. (2018). Numerical study of wave run-up on a fixed and vertical surface-piercing cylinder subjected to regular, non-breaking waves using openfoam. *Applied Ocean Research*, 79:228–252.

Moin, P. and Kim, J. (1985). The structure of the vorticity field in turbulent channel flow. part 1. analysis of instantaneous fields and statistical correlations. *Journal of Fluid Mechanics*, 155:441–464.

Morison, J. R., O'Brien, M. P., Johnson, N. P., and Schaaf, S. A. (1950). The force exerted by surface waves on piles. *Petroleum Transactions*, 189:149–157.

Myrhaug, D. and Ong, M. C. (2013). Effects of sand-clay mixtures on scour around vertical piles due to long-crested and short-crested nonlinear random waves. *Journal of Offshore Mechanics and Arctic Engineering*, 135(3):034502.

Niedzwecki, J. M. and Duggal, S. D. (1992). Wave run-up and forces on cylinders in regular and random waves. *Journal of Waterway, Port, Coastal, and Ocean Engineering*, 118(6):615–634.

Niedzwecki, J. M. and Huston, J. R. (1992). Wave interaction with tension leg platforms. *Ocean Engineering*, 19(1):21–37.

Nielsen, A. W., Sumer, B. M., Ebbe, S., and Fredsøe, J. (2012). Experimental study on the scour around a monopile in breaking waves. *J. Waterw, Port, C - ASCE*, 138 (6):501–506.

Okubo, A. (1970). Horizontal dispersion of floatable particles in the vicinity of velocity singularities such as convergences. *Deep Sea Research and Oceanographic Abstracts*, 17(3):445–454.

Olsen, N. R. B. and Kjellesvig, H. M. (1998). Three-dimensional numerical flow modeling for estimation of maximum local scour depth. *Journal of Hydraulics Engineering*, 36:579–590.

Ong, M. C., Myrhaug, D., and Hesten, P. (2013). Scour around vertical piles due to long-crested and short-crested nonlinear random waves plus a current. *Coast. Eng.*, 73:106–114.

Ong, M. C., Utnes, T., Holmedal, L. E., Myrhaug, D., and Pettersen, B. (2009). Numerical simulation of flow around a smooth circular cylinder at very high reynolds numbers. *Marine Structures*, 22:142–153.

Rosetti, G., Vaz, G., and Fujarra, A. L. C. (2012). Urans calculations for smooth circular cylinder flow in a wide range of reynolds numbers: Solution verification and validation. *Journal of Fluids Engineering*, 134(12):549.

Roulund, A., Sumer, B. M., and Fredsøe, J. (2005). Numerical and experimental investigation of flow and scour around a circular pile. *Journal of Fluid Mechanics*, 534:351–401.

Sarpkaya, T. (1976). In-line and transverse forces on cylinders in oscillating flow at high reynolds' numbers. In *Proceedings of the Eighth Offshore Technology Conference*, pages 95–108, Houston, Texas, OTC 2533.

Sharma, J. N. and Dean, R. G. (1981). Second-order directional seas and associated wave forces. *Soc. Petrol. Eng. J.*, 21:129–140.

Soulsby, R. (1997). *Dynamics of Marine Sands*. Thomas Telford London, UK.

Sumer, B. M., Christiansen, N., and Fredsøe, J. (1997). The horseshoe vortex and and vortex shedding around a vertical wall-mounted cylinder exposed to waves. *J. Fluid Mech.*, 332:41–70.

Sumer, B. M. and Fredsøe, J. (2002). *The mechanics of scour in the marine environment*. Advanced Series on Ocean Engineering. Vol. 17.

Sumer, B. M., Fredsøe, J., and Christiansen, N. (1992). Scour around a vertical pile in waves. *J. Waterw, Port, C - ASCE*, 118 (1):15–31.

Sun, L., Zang, J., Chen, L., Taylor, R. E., and Taylor, P. H. (2016). Regular waves onto a truncated circular column: a comparison of experiments a and simulations. *Applied Ocean Research*, 59:650–662.

Swan, C. and Sheikh, R. (2015). The interaction between steep waves and a surface piercing column. *Philosophical Transactions of the Royal Society A*, 373(2033).

Tavouktsoglou, N. S., Harris, J. M., Simons, R. R., and Whitehouse, R. J. S. (2017). Equilibrium scour-depth prediction around cylindrical structures. *J. Waterw, Port, C - ASCE*, 143 (5).

Ting, F. C. K. (2013). Laboratory measurements of large-scale near-bed turbulent flow structures under plunging regular waves. *Coastal Engineering*, 77:120–139.

Umeda, S. (2011). Scour regime and scour depth around a pile in waves. *J. Coastal Res.*, Special Issue 64:845–849.

Van Weele, B. J. and Herbich, J. B. (1972). Wave reflection and trasmission for pile arrays. *Proc. 13th Coast. Eng. Conference*, 13:1935–1953.

Vongvisessomjai, S. & Silvester, R. (1976). Wave forces on submerged objects. In *Coastal Engineering Proceedings*, volume 15, pages 2387–2412.

Weiss, J. (1991). The dynamics of enstrophy transfer in two-dimensional hydrodynamics. *Physica D: Nonlinear Phenomena*, 48(2-3):273–294.

Whitehouse, R. (1998). *Scour at marine structures: a manual for practical applications*. Thomas Telford.

Williamson, C. H. K. (1985). Sinusoidal flow relative to circular cylinders. *J. Fluid Mech.*, 155:141 – 174.

WindEurope (2019). Offshore wind in europe. key trends and statistics 2018. Technical report, Colin Walsh.

Zanke, U. C. E., Hsu, T.-W., Roland, A., Link, O., and Diab, R. (2011). Equilibrium scour depths around piles in noncohesive sediments under currents and waves. *Coastal Engineering*, 58:986–991.